

DISS. ETH NO. 27909

# **Attosecond Coincidence Spectroscopy of Molecules and Clusters**

A thesis submitted to attain the degree of

DOCTOR OF SCIENCES of ETH ZURICH

(Dr. sc. ETH Zurich)

presented by

**Saijoscha Heck**

M.Sc. Physics, Ruprecht-Karls-Universität Heidelberg

born on 07.03.1993

citizen of  
Germany

accepted on the recommendation of

Prof. Dr. Hans Jakob Wörner, examiner

Prof. Dr. Gunnar Jeschke, co-examiner

2021

---

# Contents

<b>Abstract</b>	<b>v</b>
<b>Zusammenfassung</b>	<b>vii</b>
<b>1 Introduction</b>	<b>1</b>
<b>2 Attosecond Photoionization Spectroscopy</b>	<b>5</b>
2.1 The Photoionization Process . . . . .	7
2.1.1 Scattering Theory . . . . .	8
2.1.2 Resonance Phenomena . . . . .	11
2.1.3 Photoionization Time Delays . . . . .	12
2.2 Attosecond Pulse Generation . . . . .	14
2.2.1 High-Harmonic Generation . . . . .	14
2.3 The RABBIT Technique . . . . .	18

---

<b>3</b>	<b>Experimental Methods</b>	<b>23</b>
3.1	Laser system . . . . .	25
3.2	Attosecond Beamline . . . . .	25
3.2.1	Active Interferometer Stabilization . . . . .	29
3.3	Detection Chamber . . . . .	32
3.3.1	Electron and Ion Spectrometer . . . . .	33
3.3.2	Jet Chamber . . . . .	35
3.3.3	Data Processing . . . . .	37
3.4	Data Analysis . . . . .	40
3.4.1	Calibration . . . . .	41
3.4.2	RABBIT . . . . .	44
<b>4</b>	<b>Molecular-Frame-Resolved Photoionization Time Delays</b>	<b>49</b>
4.1	Attosecond Interferometry of Shape Resonances in the Recoil Frame of $\text{CF}_4$ . . . . .	53
4.2	Conclusion and Outlook . . . . .	74
<b>5</b>	<b>Attosecond Spectroscopy of Clusters</b>	<b>75</b>
5.1	Attosecond Spectroscopy of Size-Resolved Water Clus- ters . . . . .	77
5.2	Argon Clusters . . . . .	93
5.3	Conclusion and Outlook . . . . .	99



---

<b>6</b>	<b>Attosecond Spectroscopy of Rare Gas Dimers</b>	<b>101</b>
6.1	Two-Center Interference in Dimers . . . . .	105
6.2	Molecular-Frame-Resolved Delays of Neon Dimer . .	113
6.3	Conclusion and Outlook . . . . .	117
<b>7</b>	<b>Conclusion</b>	<b>119</b>
	<b>Appendix A</b>	<b>123</b>
	<b>Appendix B</b>	<b>139</b>
	<b>Appendix C</b>	<b>169</b>
	<b>Author Contributions</b>	<b>172</b>
	<b>References</b>	<b>175</b>
	<b>List of Publications</b>	<b>194</b>
	<b>Curriculum Vitae</b>	<b>196</b>
	<b>Acknowledgement</b>	<b>200</b>



# Abstract

Electron dynamics in atomic and molecular systems happen on an attosecond ( $10^{-18}$  s) timescale. The photoionization dynamics can be measured with an interferometric approach using attosecond XUV pump and femtosecond IR probe pulses, known as Reconstruction of Attosecond Beating By Interference of two-photon Transitions (RABBIT). RABBIT is a well-established technique in which the kinetic energy of the photoelectron is measured as a function of the XUV-IR time delay. In this thesis, an extension of this method, which combines RABBIT with an electron-ion coincidence 3D momentum imaging technique, is utilized to measure photoionization delays of molecules and clusters. The results consist of fundamental discoveries that offer novel perspectives on our understanding of attosecond dynamics in molecules.

First, a direct measurement of recoil-frame angle resolved photoionization delays in the vicinity of several shape resonances of  $\text{CF}_4$  is presented in combination with full electronic-state resolution. Through this technique, new fundamental insights into the spatio-temporal photoionization dynamics of molecular shape resonances are obtained. Referencing the ionization delays of  $\text{CF}_4$  to argon, which has a similar ionization potential and is simultaneously measured, leads to almost complete cancellation of any laser-induced effects. Large delays are found in the vicinity of the shape resonance energies and can be attributed to the temporary trapping of

the electron. Further, the dependence of the ionization delays on the electron's angular emission direction in the molecular-frame of reference is studied and the asymmetries observed can be explained by the interference of partial-waves contributing to the resonance.

Next, the coincidence technique is leveraged to investigate the photoionization delays in clusters and in particular how these delays depend on the cluster size. For this, the novel methodology of attosecond size-resolved cluster spectroscopy is introduced and applied to small water clusters as well as argon clusters. In water clusters, a linear increase in ionization delays is found for cluster sizes up to 4-5 molecules. Little change towards larger clusters is observed. It is shown that these delays are proportional to the spatial extension of the created electron hole upon ionization. At first the spatial extension increases with cluster size and then partially localizes through the onset of structural disorder in larger clusters. Results presented for argon clusters indicate that the correlation between orbital delocalization and ionization time delays might be applicable more broadly.

Furthermore, the method of electron-ion coincidence enables the examination of the photoionization delays in several rare gas dimers of varying internuclear distances. Comparing the ionization delays of these dimers to their respective monomers gives rise to a signature of two-center interference. Two-center interference of the photoelectron wavepacket in homonuclear diatomics is a well studied phenomenon, but its effect on the ionization delay has so far only been investigated theoretically. Finally, the angle-resolved ionization delays in the molecular-frame of  $\text{Ne}_2$  are examined, yielding a surprising asymmetry of the delays along the molecular axis, which can only be explained through (partial) localization of the electron hole.

# Zusammenfassung

Elektronendynamiken in Atomen und Molekülen finden auf einer Zeitskala von Attosekunden ( $10^{-18}$  s) statt. Die Photoionisationsdynamik kann mit einem interferometrischen Ansatz unter Verwendung eines Attosekunden-XUV Pump-Pulses und eines Femtosekunden-IR Probe-Pulses gemessen werden. Diese Technik ist bekannt als Rekonstruktion von Attosekunden-Beating durch (By) Interferenz von Zweiphotonenübergängen (Two-photon transitions) (RABBIT). RABBIT ist eine etablierte Technik, bei der die kinetische Energie des Photoelektrons als Funktion der XUV-IR-Zeitverzögerung gemessen wird. In dieser Arbeit wird eine Erweiterung dieser Methode verwendet, die RABBIT mit einer Elektron-Ion-koinzidenten 3D-Impuls-Bildgebungstechnik kombiniert, um Photoionisations-Zeitverzögerungen von Molekülen und Clustern zu messen. Dadurch sind grundlegende Entdeckungen möglich, die neue Perspektiven für unser Verständnis der Attosekundendynamik in Molekülen bieten.

Zunächst wird eine direkte Messung von winkelaufgelösten Photoionisationszeitverzögerungen im Rückstosskoordinatensystem in der Nähe mehrerer Form-Resonanzen von  $\text{CF}_4$ , in Kombination mit voller elektronischer Zustandsauflösung präsentiert. Durch diese Technik werden grundlegende neue Einblicke in die räumlich-zeitliche Photoionisationsdynamik molekularer Form-Resonanzen gewonnen. Die Referenzierung der Ionisationszeitverzögerung

von  $\text{CF}_4$  mit Argon, welches ein ähnliches Ionisationspotential hat und gleichzeitig gemessen wurde, führt zu einer fast vollständigen Aufhebung jeglicher laserinduzierter Effekte. Grosse Zeitverzögerungen finden sich in der Nähe der Resonanzenergien und sind auf das vorübergehende Einfangen des Elektrons zurückzuführen. Weiterhin wird die Abhängigkeit der Ionisationszeitverzögerungen von der Winkelemissionsrichtung der Elektronen im molekularen System untersucht und die gefundenen Asymmetrien können durch die Interferenz von Partialwellen erklärt werden, die zur Resonanz beitragen.

Als nächstes wird die Koinzidenztechnik genutzt, um die Photoionisationszeitverzögerungen in Clustern zu untersuchen und insbesondere wird untersucht, wie die Zeitverzögerungen von der Größe des Clusters abhängen. Dazu wird die neue Methodik der größen aufgelösten Attosekunden-Clusterspektroskopie vorgestellt und auf kleine Wassercluster sowie Argoncluster angewendet. In Wasserclustern findet sich eine lineare Zunahme der Ionisationszeitverzögerungen bis zu einer Grösse von 4-5 Molekülen in einem Cluster, gefolgt von einer geringen Änderung hin zu größeren Clustern. Es wird gezeigt, dass diese Verzögerungen proportional zur räumlichen Ausdehnung des erzeugten Elektronenlochs sind, die zuerst mit der Clustergröße zunimmt und dann teilweise, durch das Einsetzen struktureller Unordnung in größeren Clustern, lokalisiert wird. Die für Argoncluster präsentierten Ergebnisse zeigen, dass die Korrelation zwischen Orbitaldelokalisierung und Ionisationszeitverzögerungen möglicherweise allgemeiner anwendbar ist.

Darüber hinaus ermöglicht die Elektron-Ion-Koinzidenz die Untersuchung der Photoionisationszeitverzögerungen mehrerer Edelgasdimere mit unterschiedlichen Kernabständen. In den Ionisationszeitverzögerungen der Dimere, verglichen mit ihren jeweiligen Monomeren, findet man eine Signatur der Zwei-Zentren-Interferenz. Die Zwei-Zentren-Interferenz des Photoelektronen-Wellenpakets in homonuklearen zweiatomigen Molekülen ist ein gut untersuchtes Phänomen, aber ihr Einfluss auf die Ionisation-

szeitverzögerung wurde bisher nur theoretisch untersucht. Schliesslich werden die winkelaufgelösten Ionisationsverzögerungen im molekularen System von  $\text{Ne}_2$  untersucht, was zu einer überraschenden Asymmetrie entlang der Molekülachse führt, die nur durch eine (partielle) Lokalisierung des Elektronenlochs erklärt werden kann.





# Chapter 1

## Introduction

Looking at our surroundings we experience a world full of dynamics. Animals are moving around, plants are constantly growing, sun and moon are seemingly orbiting the earth and even the solid ground we are living on is shaking from time to time. Everything around us is in constant motion and we have evolved to perceive a large range of dynamics, spanning from processes over long timescales that are recorded and passed on in form of stories and history over generations ( $10^{10}$  s), to the fastest processes our eye can just register with a frame rate of approximately 75 fps ( $\sim 10^{-2}$  s) [1]. So, it does not come as a surprise that studying dynamics has played a central role in scientific research from past to present.

Initially, the timescale of fast processes was limited to what could be observed by eye without additional tools, however this changed with the deployment of short flashes of light to visualize rapid phenomena: in 1864, August Toepler used short light pulses with a variable delay after the ignition of a shock wave to make the propagation of sound waves visible to the human eye [2]. This methodology marks the beginning of pump-probe experiments. Since then the new limit for the shortest timescales that can be studied, is given by the briefest duration of light pulses one can produce. With incoher-

ent light this limit is in the milli- to nanosecond-regime. Through the advances of pulsed laser systems in the second half of the twentieth century, shorter pulses enabled even shorter timescale [3]: a breakthrough in laser development was the invention of modelocking in 1969 [4], which enabled sub-picosecond laser pulses [5] for the first time. With the deployment of femtosecond laser pulses it was suddenly possible to observe the motion of atoms and molecules and thereby track chemical reactions like the formation and breakage of chemical bonds in real-time [6–9]. This established the field of femtochemistry for whose pioneering work Ahmed Zewail was awarded the Nobel Prize in 1999.

The next barrier is of course the sub-femtosecond regime, which was broken just as the new millennium started [10, 11], by employing the technique of high harmonic generation. With the first attosecond pulses the timescale of electronic motion in atoms and molecules came into reach: the quantum mechanical oscillation period  $T_{osc} = 2\pi(\hbar/\Delta E)$  for typical electron binding energies is on the order of attoseconds [3]. The atomic unit of time is defined as  $\tau_a = \hbar/E_H = 24.2$  as, with one Hartree  $E_H = 27.2$  eV, which is twice the binding energy of hydrogen, is also on the attosecond timescale. Accessing the timescales of electronic motion opens up the possibility to study chemical bonds on a more fundamental level and thereby increases our understanding of chemical reactions in general. By gaining control of electron motion in molecular bonds it could even become possible to create - thus far - unknown molecular compounds [3].

The first direct observation of electronic motion inside an atom was reported in 2002 by Drescher et al. [12] - right after the first generation of attosecond pulses was reported. Already shortly afterwards, the control of electron wavepackets on a timescale shorter than 250 as has been reported [13].

The first information about the emission time of an electron was ob-

tained in 2007, when Cavalieri et al. [14] measured a delay of 110 as in tungsten between electrons originating from the 4f orbital and the conduction band. A delay of 21 as in Ne between the emission of an electron from a 2s orbital and the emission from a 2p orbital was found by Schultze et al. in 2010 [15].

Since then, there have been many efforts to extend our knowledge of electron dynamics by measuring photoionization time delays in atoms [15–26], molecules [27–29], solids [14, 30, 31] and even liquids [32]. However, most of the endeavors so far have remained focused on atoms and small molecules, in large part due to the challenge of spectral overlap involved in extracting electron phases from complex systems [33].

In this thesis, the combination of attosecond spectroscopy with electron-ion coincidence detection is used to measure photoionization delays of more complex systems. The focus in doing so lies on leveraging the coincidence technique to measure novel aspects of systems, such as fully angular-resolved delays in the molecular frame of  $\text{CF}_4$ , cluster size-resolved delays of argon and water clusters, as well as ionization delays in rare-gas dimers of various internuclear distances.

In the following an outline of the thesis is given:

*Chapter 2* introduces the overall framework, on which the experimental discussions are based on. In the beginning of the chapter, photoionization will be discussed in the context of scattering theory and the concept of a time delay in the ionization process is established. Next, the generation of attosecond pulses and the experimental techniques we use to measure ionization time delays are explained.

*Chapter 3* explains the experimental apparatus and the process of data analysis in detail. It starts with the description of the laser system and the beamline. Subsequently, the electron-ion coincidence detection chamber is treated together with the target preparation.

The remaining part of the chapter outlines the data processing, calibration procedures as well as the analysis of the RABBIT spectrograms.

*Chapter 4* discusses the molecular-frame-resolved photoionization delays in  $\text{CF}_4$  in the presence of several shape resonances. Large delays, caused by the temporary trapping of the electron are observed and the dependence on the electron's angular emission direction is studied with a partial-wave analysis.

*Chapter 5* presents results of size-resolved photoionization delays for different clusters. First, findings of an increasing delay for increasing cluster size in small  $\text{H}_2\text{O}$  and  $\text{D}_2\text{O}$  clusters are shown together with a thorough investigation on the cause of this effect. In addition, results of photoionization delays in small argon clusters are presented.

*Chapter 6* presents photoionization delays in rare-gas dimers compared to their monomers and investigates how they depend on the electrons kinetic energy. By studying dimers with varying internuclear distances ( $\text{Ne}_2$ ,  $\text{Ar}_2$  and  $\text{Kr}_2$ ) an indication of two-center interference is found for krypton dimers, which show the largest internuclear distance of the dimers investigated. Further, the angular resolved ionization delays in the molecular frame of  $\text{Ne}_2$  are presented.

## Chapter 2

# Attosecond Photoionization Spectroscopy

In this chapter the fundamental concepts of attosecond photoionization spectroscopy are introduced. First, an overview of photoionization and scattering theory will be given and then it is shown how one can define a quantity for photoionization time-delays. Next, the experimental techniques that enable us to measure photoionization time-delays in atoms and molecules are explained in detail.



## 2.1 The Photoionization Process

One of the key discoveries of the 20th centuries is the *photoelectric effect*, for the explanation of which Albert Einstein was awarded the Nobel Prize in 1921. The photoelectric effect describes the emission of an electron when electromagnetic radiation, with frequencies above a certain threshold, hits matter. This process is nowadays classified as *photoionization* or *photoemission* (in condensed phase) and can be schematically written, for the ionization of an effective one-electron atom  $A$ , as [34]

$$A(n, l) + \hbar\omega \longrightarrow A^+ + e^-(E, l'), \quad (2.1)$$

where  $n$  is the principle quantum number and  $l$  is the orbital angular momentum of the bound state.  $e^-$  is a free electron with angular momentum  $l'$  and energy  $E$ , which is related to the wavevector  $\vec{k}$  and depends on the ionization potential  $I_p$  of the atom

$$E = \frac{\hbar^2 k^2}{2m_e} = \hbar\omega - I_p. \quad (2.2)$$

Assuming the photon presents only a weak perturbation to the system, the ionization can be described as a dipole transition between an initial bound state  $|\Psi_i\rangle$  and a final state  $|\Psi_{f,\vec{k}}\rangle$  with the photoionization transition dipole matrix element [35]

$$D_{\vec{k},\vec{n}}^- = \langle \Psi_{f,\vec{k}} | \vec{r} \vec{\epsilon} | \Psi_i \rangle, \quad (2.3)$$

where the dipole operator is the product of the position operator  $\vec{r}$  and the electric field of the ionizing radiation  $\vec{\epsilon}$ . The photoionization cross-section  $\sigma$  gives the probability of this transition and is proportional to its absolute square

$$\sigma \propto |D_{\vec{k},\vec{\epsilon}}^-|^2. \quad (2.4)$$

In photoionization, the final state  $\Psi_{f,\vec{k}}$  is a continuum state and best described by a scattering wave function, since the ionization process can be treated as a scattering process within quantum scatter-

ing theory. In the following an introduction into this formalism is given, since it will be useful in the treatment and interpretation of the content presented in this thesis.

### 2.1.1 Scattering Theory

Let's consider a prototypical scattering problem, where a particle with wavefunction  $\Psi_{\vec{r},t}$  scatters elastically on a central potential  $V(r)$ . The time-dependent Schrödinger equation for this problem is

$$\left(-\frac{\hbar^2}{2m}\Delta + V(r)\right)\Psi_{\vec{k}}(\vec{r},t) = i\hbar\frac{\partial\Psi_{\vec{k}}(\vec{r},t)}{\partial t}, \quad (2.5)$$

where  $m$  is the mass of the particle and  $\Delta$  is the Laplace operator. Since the scattering potential is time-independent, the particle wavefunction can be written as

$$\Psi_{\vec{k}}(\vec{r},t) = \Psi_{\vec{k}}(\vec{r})e^{-iEt/\hbar} \quad (2.6)$$

and the Schrödinger equation then simplifies to its time-independent version

$$\left(-\frac{\hbar^2}{2m}\Delta + V(r)\right)\Psi_{\vec{k}}(\vec{r}) = E\Psi_{\vec{k}}(\vec{r}). \quad (2.7)$$

A solution to equation (2.7) for the asymptotic case of  $r \rightarrow \infty$  and  $V(\infty) = 0$ <sup>1</sup>, consists of the sum of a plane wave and a scattered spherical wave with scattering amplitude  $f(\theta)$  [35]

$$\Psi_{\vec{k}}(\vec{r},\theta) \xrightarrow{R \rightarrow \infty} e^{i\vec{k}\vec{r}} + f(\theta)\frac{e^{i\vec{k}\vec{r}}}{r}. \quad (2.8)$$

Here,  $\theta$  is the polar angle of the spherical coordinate system and  $\Psi_{\vec{k}}(\vec{r})$  is the asymptotic stationary scattering state. The scattering amplitude is directly related to the differential cross-section  $\sigma_{DCS}$  by

$$\sigma_{DCS}(\theta) = |f(\theta)|^2. \quad (2.9)$$

---

<sup>1</sup>Strictly speaking this is only valid for short range potentials (approaches zero more rapidly than  $1/r$ , for  $r \rightarrow \infty$ ), which excludes the Coulomb potential. Instead a *screened Coulomb potential* (also known as Yukawa potential) can be used, which falls off faster in the long range [35, 36].



### Partial Wave Expansion

A full solution of the Schrödinger equation (2.7) can be achieved by an expansion into a series of radial and angular wavefunctions

$$\Psi(\vec{r}) = \sum_{l=0}^{\infty} \sum_{m=-l}^l c_{l,m_l} \frac{u_l(r)}{r} Y_{l,m_l}(\theta, \phi), \quad (2.10)$$

where  $Y_{l,m_l}$  are the spherical harmonics with quantum numbers  $l$  and  $m_l$  for angular momentum and projection of angular momentum respectively and  $c_{l,m_l}$  is some coefficient (see [35] ch. 14 or [37] ch. 6 for a step-by-step solution).  $u_l(r)$  is the radial part of the wavefunction and solves the Schrödinger equation

$$\left( -\frac{\hbar^2}{2m} \frac{d^2}{dr^2} + \frac{\hbar^2 l(l+1)}{2mr^2} + V(r) \right) u_l(r) = E u_l(r). \quad (2.11)$$

The effective potential in this equation contains a new term, which is proportional to  $l(l+1)/r^2$ . This term is known as the centrifugal potential, which is caused by the orbital motion of the particle around the scattering potential. For a vanishing potential  $V(r) = 0$  the asymptotic behavior of the radial wavefunction can be described as [37]

$$u_l^{V=0}(r) \underset{r \rightarrow \infty}{\propto} \sin(kr - l\frac{\pi}{2}). \quad (2.12)$$

And for the general case, with a spherically symmetric potential  $V(r) \neq 0$ , we have

$$u_l(r) \underset{r \rightarrow \infty}{\propto} \sin(kr - l\frac{\pi}{2} + \delta_l). \quad (2.13)$$

Note, that the only difference between (2.12) and (2.13) is a phase shift  $\delta_l$ . Intuitively this means that the effect of an elastic scattering of a particle wave, is just a phase shift compared to the unperturbed wave, in its asymptotic behavior. An illustration of the scattering phase shift due to an attractive potential is shown in Figure 2.1, where the scattered wave (in black) is compared with an unperturbed wave (in red).

For the full solution of the Schrödinger equation in (2.7) we still need a description of the scattering amplitude  $f(\theta)$ , which is found to be [37]

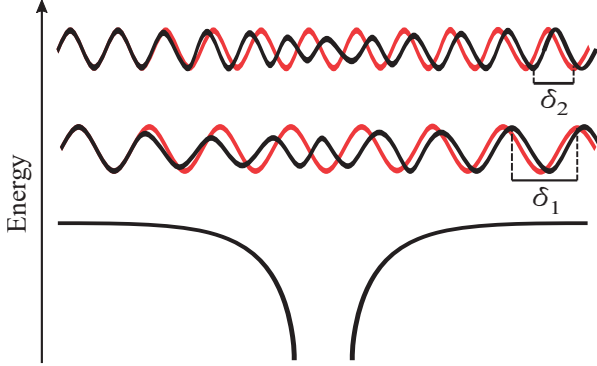


**Figure 2.1:** Illustration of the scattering phase  $\delta$  for an attractive potential. The black line shows an unperturbed wave in comparison to the scattered wave (red line).

$$f(\theta) = \frac{1}{2ik} \sum_{l=0}^{\infty} (2l+1)(e^{2i\delta_l} - 1)P_l(\cos \theta). \quad (2.14)$$

Here,  $P_l$  are the Legendre polynomials with

$$\begin{aligned} P_0(\cos \theta) &= 1 \\ P_1(\cos \theta) &= \cos \theta \\ P_2(\cos \theta) &= 1/2(3 \cos^2 \theta - 1) \end{aligned} \quad (2.15)$$

and so on. The factor  $e^{2i\delta_l}$  is called the scattering matrix element  $S_l = e^{2i\delta_l}$  and gives the ratio of the amplitudes from outgoing and incoming waves<sup>2</sup>. This can be seen when the asymptotic scattering state from (2.8) is written in a new form [35]

$$\begin{aligned} \Psi_{\vec{r},\theta} \simeq & \sum_{l=0}^{\infty} \frac{i^{l-1}(2l+1)}{2kr} P_l(\cos \theta) (-e^{-i(kr-l\pi/2)} + e^{i(kr-l\pi/2+2\delta_l)}) \\ & \sum_{l=0}^{\infty} \frac{i^{l-1}(2l+1)}{2kr} P_l(\cos \theta) (-e^{-i(kr-l\pi/2)} + e^{i(kr-l\pi/2)} S_l). \end{aligned} \quad (2.16)$$

---

<sup>2</sup>The scattering matrix is diagonal only in the case of a spherically symmetric potential. Otherwise, it has off-diagonal terms that represent the mixing of partial waves.

This decomposition of  $f(\theta)$  is called a partial wave analysis of the scattering amplitude and each partial wave stationary scattering state  $\Psi_k^l(\vec{r})$  is a solution to the Schrödinger equation. We see that the scattering with the contribution  $l = 0$  results in a s-wave,  $l = 1$  in a p-wave and  $l = 2$  in a d-wave.

### 2.1.2 Resonance Phenomena

The total cross-section  $\sigma_{tot}$  is a sum of all partial-wave cross-sections  $\sigma_l$  [35]

$$\sigma_{tot} = \sum_l \sigma_l \quad (2.17)$$

with

$$\sigma_l = \frac{\pi}{k^2} (2l + 1) |S_l - 1|^2 = \frac{\pi}{k^2} (2l + 1) \sin^2 \delta_l. \quad (2.18)$$

Where the partial-wave cross-section  $\sigma_l$  specifies the cross-section for each partial wave in the partial-wave expansion (2.10). From (2.17) and (2.18) we see that the scattering cross-section is dependent on the scattering matrix element and hence of the phase shift between scattered and unscattered wave  $\delta_l$ .

Any change of the scattering phase leads to a variation in the cross-section. From (2.18), it can easily be seen that a phase shift of  $\pi/2$  results in the largest cross-section. This (rapid) change of cross-section as a function of energy is often associated with a *resonance*. There are many causes for resonance phenomena, but a particularly common kind of resonance in scattering are *shape resonances*. The phenomenon of shape resonances will also be examined in more detail in chapter 4 of this thesis.

#### Shape Resonances

A shape resonance describes a situation in which a scattered electron with angular momentum  $l > 0$  is trapped in a quasi-bound state formed by the combination of short-range, Coulomb and centrifugal potentials  $\hbar^2 l(l + 1)/(2mr^2)$  [38], as sketched in Figure 2.2.

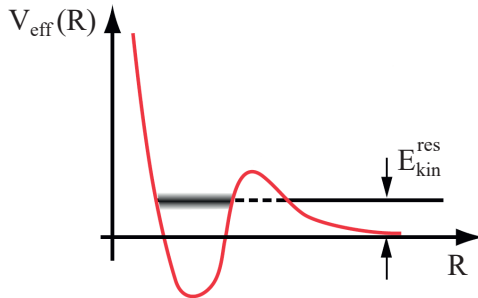


**Figure 2.2:** Schematic representation of the effective potential in a shape resonance for an electron resonance energy of  $E_{kin}^{res}$ . Adapted from [37].

This intermediate state has a finite lifetime  $\tau = \hbar/\Gamma$ , given by the natural linewidth  $\Gamma$ . Eventually, the electron tunnels through the potential barrier and escapes into the continuum [37].

### 2.1.3 Photoionization Time Delays

An interesting question, when thinking about the photoionization process, is how long it takes for the electron to leave the atom or molecule, upon the absorption of a photon. The concept of a time-delay in a scattering event has already been introduced more than 60 years ago by Eisenbud, Wigner and Smith [39, 40]. They proposed that the phase shift  $\delta$  of a scattered wave, as illustrated in 2.1, leads to a different arrival time at a distance  $r$  outside the potential, compared to an unperturbed wave of the same energy. This time-delay is known as Eisenbud-Wigner-Smith delay (or Wigner delay  $\tau_W$  in short). The Wigner delay relates to the scattering phase shift  $\delta_l$  via a derivative with respect to the energy  $E$

$$\tau_W(E) = \hbar \frac{d\delta_l(E)}{dE}. \quad (2.19)$$

This equation already gives the Wigner time for photoionization, which is treated as half a scattering process because the electron wavepacket starts in the center of a potential. For a full scattering process, as it was originally described by Eisenbud, Wigner and

Smith, equation (2.19) is multiplied with a factor of two.

The Wigner time can also be interpreted as the group delay of the outgoing electron wavepacket [41, 42] and gives the delay of a photoelectron wavepacket compared to a free electron of the same energy.

Theoretically the Wigner delay  $\tau_W$  can be calculated by taking the energy derivative of the exponent on the scattering matrix element

$$\tau_W = \frac{d \arg(S_I)}{dE}, \quad (2.20)$$

which is the derivative of the argument of the photoionization dipole matrix element  $D$  (see eq. (2.3)) [43, 44]

$$\tau_W = \frac{\partial \arg(D)}{\partial E} = \frac{\partial}{\partial E} \arg(\langle \Psi_{f,\vec{k}} | \vec{r} \vec{\epsilon} | \Psi_i \rangle). \quad (2.21)$$

The photoionization dipole matrix element can readily be calculated for small molecular targets with quantum scattering programs, such as ePolyScat [45, 46].

Experimentally it is much more challenging to access the Wigner delay due to its short time scales in the attosecond ( $10^{-18}$  s) regime. It took more than 50 years after the theoretical predictions of Eisenbud, Wigner and Smith before time-delays in electron emission were first measured [14, 15, 47]. The established techniques to measure photoionization time delays are *attosecond streaking* [48], which relies on a single attosecond pulse, and *RABBIT* (Reconstruction of attosecond beating by two-photon transition) [10, 49], which uses a train of attosecond pulses. The work presented in this thesis, relies on the latter.

Before establishing the RABBIT technique in more detail in section 2.3, high-harmonic generation as a means to generate attosecond pulses will be introduced in the following.

## 2.2 Attosecond Pulse Generation

The duration of a laser pulse is fundamentally limited by the time-bandwidth relation [50]

$$\Delta E \Delta t \geq \hbar, \quad (2.22)$$

where  $E$  is energy,  $t$  time and  $\hbar$  the reduced Planck constant. If the pulse can be described by a Gaussian shape (see Figure 3.1 b for the pulse shape of the beam used in this work) this manifests itself in a lower limit for the time-bandwidth product

$$\tau \cdot \Delta \nu \geq 0.44. \quad (2.23)$$

Here  $\tau$  is the temporal duration and  $\Delta \nu$  is the spectral bandwidth of the pulse. In order to have a pulse length of  $\tau < 1$  fs, it is necessary to have a spectral bandwidth of at least  $\Delta \nu = 4.4 \cdot 10^{14}$  Hz, which corresponds to 1.8 eV. Since this is already larger than the bandwidth of visible light (ranging from  $\sim 1.5$  eV - 3 eV), producing attosecond pulses requires a central wavelength in the UV to XUV regime. This can be achieved in a laboratory setting utilizing *high-harmonic generation* (HHG) [51–53], which is the generation of high-order harmonics of a fundamental laser field. Until recent developments at free-electron lasers (FEL) [54], this had been the only possibility to generate attosecond pulses.

### 2.2.1 High-Harmonic Generation

The process of high-harmonic generation can be explained in a semi-classical picture, known as the *three-step model* (or simple man's model) [52, 56], illustrated in Figure 2.3. As the name suggests, HHG can be divided into three distinct steps: The presence of a strong laser field bends the Coulomb potential enough that an initially bound electron can tunnel through the barrier in the first step. Second, the electron is now exposed to the laser field and is accelerated by its strong electric field. Within one laser cycle the electron is first moving away from its origin and is then accelerated back towards the parent ion. If the trajectory of the electron leads it right

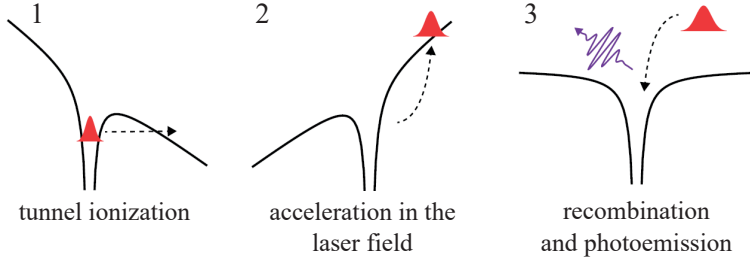


**Figure 2.3:** Illustration of the three-step model. (1) The electron tunnels through the Coulomb potential, (2) is accelerated in the laser field and (3) recombines with the atom, leading to the emission of a high energy photon. Adapted from [55].

back to its origin it can come to a recombination of electron and parent ion, together with the emission of a high energetic photon. This recombination constitutes the third step.

Which electron trajectories recollide with the parent ion depends on its emission time with respect to the laser field. The motion of the electron in the laser field can be modeled in a classical way and some trajectories are shown in Figure 2.4 a for a one-dimensional model. The energy an electron can accumulate in the laser field is shown in Figure 2.4 b as a function of the emission time of the electron. It can be seen that for each final energy of the electron there exist two distinct trajectories, which are known as *short* and *long* trajectories, based on the time it takes the electron to recollide. The maximum possible energy, the electron can acquire, is

$$E_{\max} = 3.17 \cdot U_p \quad (2.24)$$

with the ponderomotive potential

$$U_p = \frac{2e^2 I}{4c\epsilon_0 m_e \omega_0^2}, \quad (2.25)$$

which depends on the intensity  $I$  and the angular frequency  $\omega_0$  of the driving laser field. Upon recollision, the energy of the emitted photon is the combination of electron energy and the ionization potential  $I_p$  of the generation gas. The maximum photon energy, called

## 2.2. Attosecond Pulse Generation

cut-off energy, is then

$$E_{\text{cutoff}} = 3.17U_p + I_p. \quad (2.26)$$

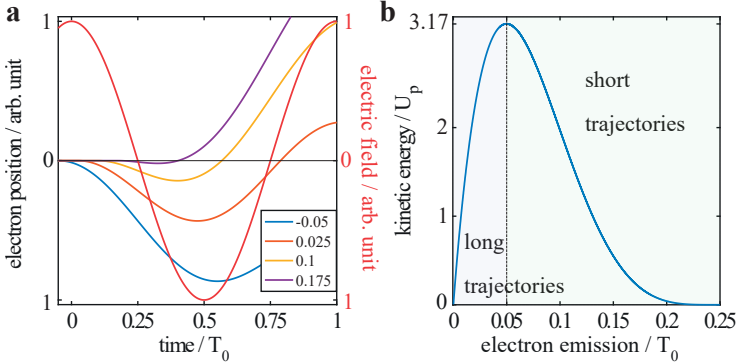


**Figure 2.4:** (a) Multiple one-dimensional electron trajectories with different emission times into the laser field as indicated in the legend. The electric component of the laser field with period  $T_0$  is shown in red. (b) Kinetic energy of electrons at recollision as a function of emission time into the laser field. Emission at an early time after the peak of the electric field leads to long trajectories compared with emission at a later time leading to short trajectories with identical final energies.

The process of ionization, acceleration and recombination happens each half-cycle of the driving field, leading to a train of attosecond XUV pulses (also called *attosecond pulse train*, or APT), separated in time by half the period of the driving field  $T_0$ . This periodicity in time results in a frequency comb of harmonics, spaced by twice the fundamental frequency  $f_0$ . In spherically symmetric generation targets, even harmonics are suppressed due to symmetry reasons and the spectrum consists only of odd harmonics. The spectrum can be described with the formula:

$$f_{2n+1} = (2n + 1)f_0, \quad (2.27)$$

where  $n=1,2,3,\dots$



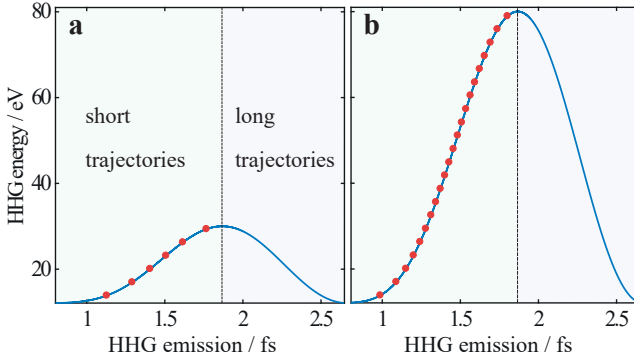


**Figure 2.5:** Energies of the emitted photons for HHG with a driving field of 800 nm in xenon as generation gas ( $I_p=12.1$  eV) as a function of the high harmonic emission time. Electric field intensities were chosen to correspond to cut-off energies of (a) 30 eV and (b) 80 eV. Red dots mark the positions of odd harmonics. The dependence of harmonic energies on the recollision time is known as *attochirp*.

As a result of the classical electron trajectories, the harmonics are emitted at different times in the laser cycle, which leads to a chirp of the attosecond pulse train. This effect is intrinsic to the process of high harmonic generation and commonly referred to as *attochirp*. Depending on the cut-off energy of the high harmonic spectrum, the chirp of consecutive harmonics can be more or less pronounced. This is illustrated in Figure 2.5, where the red dots depict the odd harmonics generated in xenon with a 800 nm driving field. The x-axis spacing of the harmonics corresponds to their time spacing in the attosecond pulse train. The different chirp between a cut-off energy of 30 eV and 80 eV (fig. 2.5 a and b respectively), can clearly be observed.

### Phase Matching

So far the description of high harmonic generation has been limited to the microscopic description of a single atom. Of course, experimentally this process happens simultaneously in multiple atoms on

a macroscopic scale. The coherent emission of XUV light from multiple atoms leads to interference and it needs to be ensured that the XUV photons add up constructively. This is called *phase matching* and is experimentally done by changing the mean distance between atoms (density) or the intensity of the driving field. Depending on the setup used for HHG, there are multiple parameters that have influence on the phase matching, but they can be generally linked to the interaction between target density and intensity of driving field. By choosing specific phase matching conditions it is also possible to suppress the long trajectories [57], which leads to shorter bursts of XUV pulses. This is typically done by moving the gas target downstream of the laser focus. The experimental realization of high harmonic generation in this work is described in chapter 3.2.

## 2.3 The RABBIT Technique

Reconstruction of attosecond beating by two-photon transition (RABBIT) is an interferometric approach to measure the spectral phase of an electron wave packet, upon photoionization. Initially an XUV-APT ionizes a target sample and an electron is released into the continuum with kinetic energy

$$E_{kin}^{HHn} = n \cdot \hbar\omega - I_p. \quad (2.28)$$

Here  $I_p$  is the ionization potential of the target and  $n = 3, 5, 7, 9, \dots$  is the order of the odd harmonic leading to ionization. Throughout the experiments discussed in this thesis the harmonic order  $n$  is ranging from 11 to 19 or less, but it can potentially be much higher (>500) [58].

In the electron energy spectrum this leads to the creation of multiple peaks - called *mainbands* - with a difference in energy of twice the fundamental photon energy  $\hbar\omega$ . To probe the electron emission time, an additional, weak<sup>3</sup> IR field is added to the XUV-APT with

---

<sup>3</sup>In this context weak means that the interaction of the system with the IR field is limited to a single photon interaction and the IR does not lead to a modulation of the Coulomb potential.

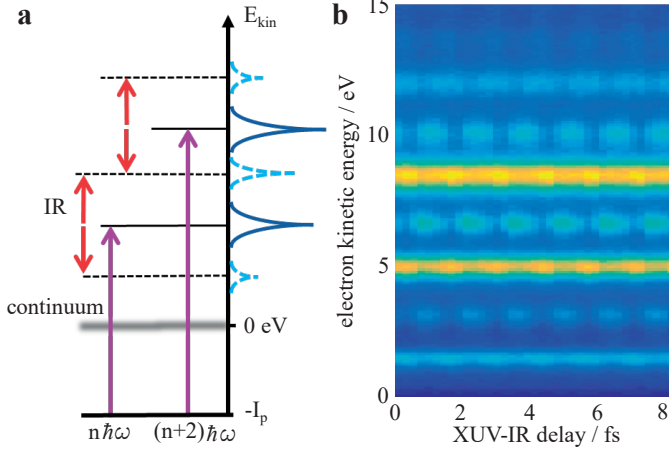


**Figure 2.6:** **(a)** Illustration of the RABBIT technique. The target atom or molecule absorbs an XUV photon with energy  $n\hbar\omega$  and a photoelectron is released into the continuum. The electron can then either absorb or emit an IR photon to generate sidebands (dashed, blue lines). **(b)** Time-resolved electron spectrum (*RABBIT spectrogram*) of argon showing sideband oscillations. Electrons come only out of the HOMO with  $I_p=15.7$  eV. Mainband  $\text{HH}_{13}$  is at 5 eV kinetic energy.

an adjustable delay between them. In the presence of the IR field the photoelectrons can further undergo a continuum-continuum (cc) transition by absorption or emission of a photon. This leads to the creation of sideband electrons with energy

$$E_{kin}^{SB_{n\pm 1}} = n \cdot \hbar\omega - I_p \pm \hbar\omega \quad (2.29)$$

as illustrated in Figure 2.6 a. There are two separate pathways leading to sideband  $SB_{n+1}$ :

1. absorption of  $\text{HH}_n$  followed by absorption of an IR photon
2. absorption of  $\text{HH}_{n+2}$  followed by emission of an IR photon.

This results in an interference of the two pathways, since it is not possible to distinguish them. The interference manifests itself as a beating in the sideband intensity, when changing the delay between XUV-APT and IR as it can be seen in Figure 2.6 b.

The sideband intensity is described by the coherent sum of the two quantum pathways contributing to a sideband of order  $n + 1$  [59]

$$\begin{aligned}
 I_{SB}(\tau) &= |M^{(a)} + M^{(e)}|^2 \\
 &= |M^{(a)}|^2 + |M^{(e)}|^2 + (M^{(a)}(\tau)M^{(e)}(\tau) + c.c) \\
 &= |M^{(a)}|^2 + |M^{(e)}|^2 + 2|M^{(a)}||M^{(e)}| \cos(\arg(M^{(a)*}M^{(e)}))
 \end{aligned} \tag{2.30}$$

with the complex amplitude for the quantum pathway, associated with the absorption of harmonic  $HH_n$  plus absorption of one IR photon

$$M^{(a)}(\tau) = |M^{(a)}| e^{i(\phi_{XUV}^n + \phi_W^n + \phi_{cc,a}^n + \omega_0\tau)} \tag{2.31}$$

and the complex amplitude for the quantum pathway, associated with the absorption of harmonic  $HH_{n+2}$  plus emission of one IR photon

$$M^{(e)}(\tau) = |M^{(e)}| e^{i(\phi_{XUV}^{n+2} + \phi_W^{n+2} + \phi_{cc,a}^{n+2} - \omega_0\tau)}. \tag{2.32}$$

Here  $\phi_{XUV}$  is the phase contribution of the attochirp (see section 2.2), which results in electrons from different mainbands being emitted at different times relative to the IR field.  $\phi_W$  is the Wigner phase, which was introduced in 2.1.3 and  $\phi_{cc,a/e}$  is the additional phase shift the electron experiences due to the continuum-continuum transition of absorption and emission respectively. With

$$\begin{aligned}
 \Delta\phi_{XUV}^{n+1} &= \phi_{XUV}^{n+2} - \phi_{XUV}^n \\
 \Delta\phi_W^{n+1} &= \phi_W^{n+2} - \phi_W^n \\
 \Delta\phi_{cc}^{n+1} &= \phi_{cc,a}^{n+2} - \phi_{cc,e}^n
 \end{aligned} \tag{2.33}$$

equation (2.30) becomes

$$\begin{aligned}
 I_{SB}(\tau) &= |M^{(a)}|^2 + |M^{(e)}|^2 \\
 &\quad + 2|M^{(a)}||M^{(e)}| \cos(2\omega_0\tau - \Delta\phi_{XUV}^{n+1} - \Delta\phi_W^{n+1} - \Delta\phi_{cc}^{n+1}).
 \end{aligned} \tag{2.34}$$

The total phase of the sideband  $\phi_{SB}^{n+1} = \phi_{XUV}^{n+1} + \Delta\phi_W^{n+1} + \Delta\phi_{cc}^{n+1}$  can be extracted from the RABBIT spectrogram, either by fitting a cosine function to the sideband intensity, or by Fourier Transformation. Originally RABBIT was mainly used for pulse characterization by measuring  $\phi_{XUV}$  [60], but more recently the technique has also been used to extract  $\phi_W$  [24]. This is possible by taking the phase difference of the same sideband from different states within one target or from different atomic or molecular species, so that  $\phi_{XUV}$  cancels out. The latter can be achieved by adding an atomic reference gas to the molecular target species. If the reference has a similar ionization potential as the target of interest, this will further lead to a cancellation of  $\phi_{cc}$ , since the cc-phase is mainly dependent on the kinetic energy of the electron [59]. It should be noted that with RABBIT it is only possible to extract phase *differences*, as seen in (2.33) and (2.34). In particular this means we can only determine differences in the Wigner phase between two different target species or between two different states within a single target.



## Chapter 3

# Experimental Methods

In this chapter the experimental setup is introduced. All experiments discussed in this thesis were conducted with the same setup, which can be divided into four distinct parts: laser system, attosecond beamline, reaction chamber and XUV spectrometer. The laser system is the initial stage, where short infrared (IR) pulses are produced, these pulses are then used to generate even shorter XUV pulses in the attosecond beamline. Those XUV pulses are then ionizing a molecular gas beam in the reaction chamber, where the created ions and electrons are detected in coincidence. In a last step, after ionizing the target molecules, the beam enters an XUV spectrometer, to characterize the photon energies. The complete setup is schematically drawn in Figure 3.2.





### 3.1 Laser system

The laser system, supplying the beamline with light, is a combination of a mode-locked Ti:Sa ultrafast laser oscillator Vitara-T-HP and a high-power Ti:Sa amplifier COHERENT® Legend Elite Duo HE+. The output are a few hundred picosecond long laser pulses with a central wavelength of 800 nm and a repetition rate of 5 kHz at 14 W. Before reaching the beamline the pulses are compressed with a reflection grating compressor (1400 lines/mm) to 35 fs with 2 mJ per pulse. The measured as well as reconstructed spectral and temporal profile from a frequency-resolved optical gating (FROG) measurement [61] is shown in Figure 3.1.

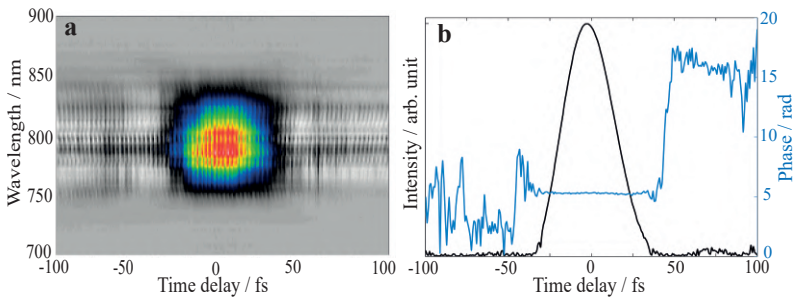


**Figure 3.1:** Measured and reconstructed temporal profile using a home-built FROG setup placed in front of the focus mirror for the high-harmonic generation (labeled number 6 in 3.2). **(a)** Measured FROG trace, **(b)** reconstructed pulse intensity in black and the phase in blue.

### 3.2 Attosecond Beamline

The attosecond beamline is built as a Mach-Zehnder interferometer [62, 63], with one arm being used to generate extreme ultraviolet (XUV) light as a pump, while the other arm serves as a weak IR probe. The whole attosecond beamline is mounted on a single optical table and the pointing of the beam entering the Mach-Zehnder interferometer is stabilized using an active beam stabilization sys-

### 3.2. Attosecond Beamline

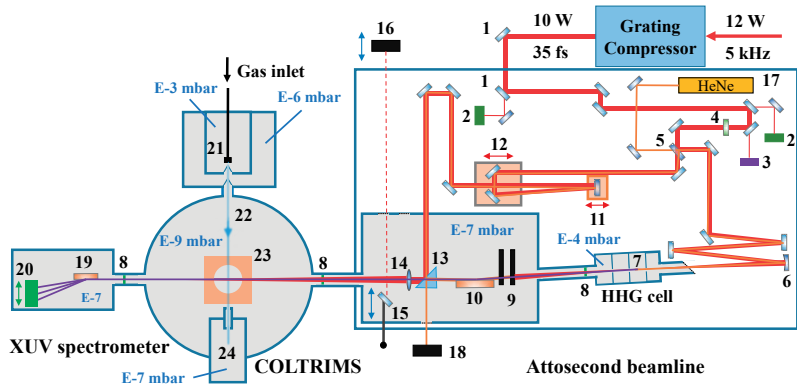


**Figure 3.2:** Schematic view of the full experimental setup, excluding the laser system. (1) Mirror actuator (beam stabilization) (2) photodiode (beam stabilization) (3) photodiode (trigger signal) (4) half-wave plate (5) 70:30 beamsplitter (6) focus mirror,  $f=0.45$  m (7) 6 mm gas target (8) pin hole (9) filter wheels (10) toroidal mirror,  $f=0.5$  m (11) piezo scanner (12) direct current motor (13) holey mirror (14) drilled focus lens,  $f=1.1$  m (15) kick-out mirror (16) CCD camera (17) HeNe laser (active stabilization) (18) CMOS camera (active stabilization) (19) reflection grating, 1200 lines/mm (20) MCP + Phosphor screen (21)  $50 \mu\text{m}$  nozzle (22) gas jet (23) electron/ion spectrometer (24) jet dump. Note that this sketch is not to scale.

$\text{tem}^1$ , consisting of two position detectors and two piezo actuated mirrors. The position detector and mirror actuators are connected via an active closed loop controller with a resolution of less than 100 nm. The placement of the position detectors and actuators can be seen in Fig. 3.2 (labeled as 2 and 3 respectively). The Mach-Zehnder interferometer divides the beam into two separate pathways with a 70:30 beamsplitter (Pos. 5 in Fig. 3.2) and are later co-linearly recombined using a holey mirror (Pos. 13 in Fig 3.2). The more intense part of the beam, in the following referred to as pump beam, is focused into a 3 mm long gas cell by a focus mirror with 45 cm focal length. The gas cell can contain various gases with backing pressures up to 100 mbar. Depending on the gas species and the respective backing pressure, XUV-APT with photon energies

<sup>1</sup>MRC Systems GmbH

ranging between 15 eV and 50 eV are generated via high-harmonic-generation (more details on the HHG process can be found in chapter 2.2). The remaining IR light in the XUV-APT is filtered out by a 100 nm thick metallic filter mounted on a quartz ring<sup>2</sup> (Pos. 9 in Fig. 3.2). The quartz ring allows part of the HeNe beam to pass by the filter, which is needed for the active interferometer stabilization described in 3.2.1. The metallic filter is additionally used to select a specific range of photon energies, since different metals have different transmission curves. In the present work, aluminum (Al) and tin (Sn) filters were used. The transmission curves of selected metal filters are shown together with the relevant high harmonic energies in Figure 3.3. The filtered and diverging XUV-APT is refocused by a nickel-coated toroidal mirror with focus length  $f=50$  cm (Pos. 10 in Fig. 3.2). The toroidal mirror is placed in a 3-f to 3-f configuration, meaning the distance between gas cell and toroidal is  $3 \times 50$  cm = 1.5 m, as is the distance between toroidal and interaction region in the COLTRIMS chamber. In this way the very small spatial distribution of the high-harmonic-generation in the gas cell is imaged into the gas jet. The resulting focal spot size is approximately the size of the imaged IR focus, which can be determined using a kick-out mirror and a CCD camera (Pos. 15 and 16 in Fig. 3.2). The focal spot size is roughly  $120 \mu\text{m}$  in diameter.

The less intense part of the beam serves as the IR probe beam. The pathlength of the IR probe can be adjusted by two linear delay stages (Pos. 11 and 12 in 3.2) with different precision. For pump-probe experiments with time-delays of up to 1 ns, a direct-current motor<sup>3</sup> with 155 mm travel range and a resolution of 50 nm is available. For RABBIT experiments a piezo scanner<sup>4</sup> with a travel range of  $30 \mu\text{m}$  (delays up to 200 fs) and a precision of 0.2 nm ( $\cong 1.33$  as) is used. The IR beam is co-linearly recombined with the XUV-APT by a holey mirror and then focused into the gas jet by a lens ( $f=1.1$  m). The holey mirror and the lens, both have a small hole drilled in their center

---

<sup>2</sup>Lebow Company

<sup>3</sup>L-511, Physik Instrumente GmbH

<sup>4</sup>P-752.2CD, Physik Instrumente GmbH

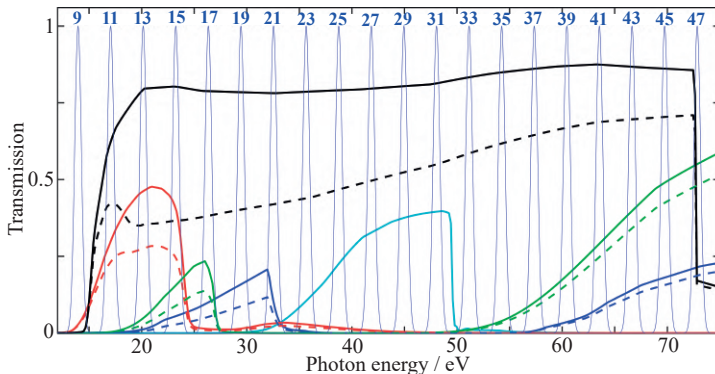


**Figure 3.3:** XUV transmission for several metallic filters. 100 nm Al (black), 100 nm Sn (red), 100 nm Zr (green), 100 nm Ti (blue) and 400 nm Mg+Parylene (cyan). Dashed lines show transmission for 10% oxidation, which is unavoidable during filter installation. Blue Gaussian lines show the position of harmonic orders, labeled in blue.

to let the XUV pass undisturbed. To ensure the co-linear alignment of the pump and probe beams, the kick-out mirror can be placed behind the lens, without breaking the vacuum. With the kick-out mirror inserted, the focus position of pump and probe beam can be imaged on a CCD camera to ensure spatial overlap. The kick-out mirror and CCD camera can also be used to find the temporal overlap between XUV and IR pulses. To do this, one needs to scan the delay between the two beams in steps smaller than the cross-correlation of the pulses (a typical value used lies between 10-30 fs), and if there is sufficient spatial overlap of the foci, it comes to very obvious interference once there is temporal overlap. This interference can easily be observed on the CCD camera in form of interference fringes. Of course we can not actually observe the XUV on our CCD camera, since it is placed outside vacuum, but rather we see the IR light generating the XUV, which is almost identical in its spatial and temporal position. With good alignment the focus position of both IR and XUV are in the center of the electron/ion spectrometer (Pos. 23 in 3.2), which is described in more detail in chapter 3.3. Behind the main chamber the XUV beam enters a photon spec-

trometer to characterize and optimize the high harmonic energies in the spectrum. The XUV spectrometer consists of a reflection grating with 1200 lines/mm and a photon detector composed of a stack of multi-channel-plates (MCP) and a phosphor screen as seen in 3.2 (Pos. 19 and 20). A typical spectrum of the XUV energies, as used in the experiments, is shown in Figure 3.4.

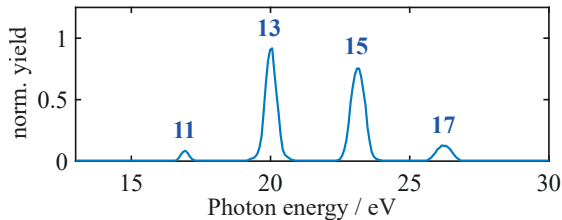


**Figure 3.4:** XUV spectrum of high harmonics generated in a 16 mbar xenon gas target with a length of 3 mm, after transmission through a 100 nm thick aluminum filter. Harmonic orders are labeled in blue.

### 3.2.1 Active Interferometer Stabilization

The length of each interferometer arm is roughly 3 m, which makes it susceptible to small changes in the pathlength. Because a pathlength difference of 1 nm already causes an effective delay of 3.3 as between pump and probe beam, it is necessary to stabilize the length difference between the arms. This is done in an interferometric approach, where a frequency-stable Helium Neon laser (HeNe) (Pos. 17 in 3.2) is coupled into the interferometer through the 70:30 beam-splitter separating the two pathways. In the XUV the 632.8 nm CW light is then recombined and out-coupled via the holey mirror and its interference pattern is read out with a CMOS camera<sup>5</sup> (Pos. 18 in 3.2). The interference is observed as radial fringes, shown in Fig. 3.5 a. The position of the fringes is moving in- or outwards with a change in pathlength difference. In our active interferometer stabilization the position of the fringes is effectively locked with a digital proportional-integral-derivative (PID) algorithm controlling the

<sup>5</sup>Daheng Imaging

piezo scanner, described previously. For this, a suitable part of the image is selected and projected onto one dimension (see yellow rectangle in Fig. 3.5 a and 1-D projection in Fig. 3.5 b). When Fourier transforming the one dimensional spectrum, the phase of the modulation frequency corresponds to the position of the fringes. This phase  $\varphi$  is related to the pump-probe time delay via

$$\tau = \varphi \frac{\lambda}{2\pi c_0} = \varphi \cdot 335.9 \text{ as/rad} \quad , \quad (3.1)$$

where  $\lambda=632.8$  nm is the wavelength of the HeNe laser. Any phase jump larger than  $2\pi$  within two consecutive steps of the feedback loop, can not be properly characterized because any modulo of  $2\pi$  of the phase results in the same value. However, without any major disturbances (such as hitting the optical table, or jumping in the lab) this does not pose a problem. The main limitation of the active phase stabilization is given by the read-out speed of the camera, which is 93 frames per second. With a laser repetition rate of 5 kHz this means that we are unable to correct any shot to shot jitter of the interferometer. Another issue is the 2 nm repeatability of the piezo scanner. It is possible that during long experiments, with many repeating scans the starting position of the piezo scanner changes by few nanometers. This leads to a small drift of the phase difference during long measurement times ( $> 1$  day). If the drift is slow compared to the time of a single scan, it can be accounted for in the offline analysis.

During a scan of the pump-probe delay, the target phase is changing as a step function (see fig. 3.6 a). The deviation from the target phase value, during a typical scan (e.g. no major disturbances in the lab), can be seen in fig. 3.6 b. With this phase error we can calculate the jitter of the delay, which is the full width at half maximum (FWHM) of the phase error distribution (see fig. 3.6 c). The jitter is usually in the range of  $\pm 40$  as for the experiments discussed in this thesis.

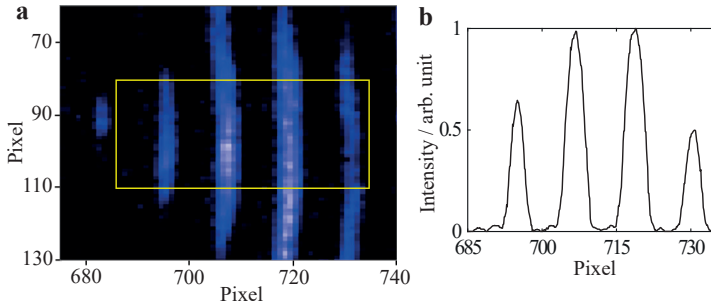


**Figure 3.5:** Interference fringes of the CW HeNe laser for the active phase stabilization between pump and probe arm. **(a)** False color image of the CCD camera showing the interference fringes. The yellow rectangle indicates the section that is used for a projection onto the x-axis, shown in **(b)**.

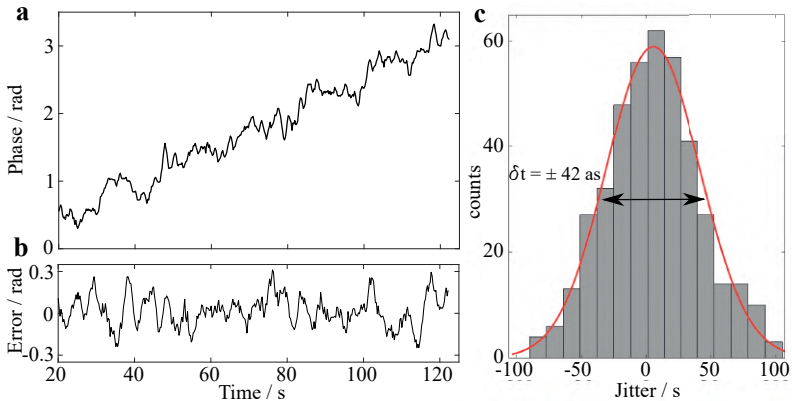


**Figure 3.6:** **(a)** Absolute phase of the modulation frequency, extracted from a Fourier transform of the projected fringes in fig. 3.5 b. During a scan of the delay, the target phase value changes as a step function, with the step size of 0.49 radians every 15 s in this case. This corresponds to steps of 165 as in the delay. **(b)** Discrepancy between the target and recorded phase values. **(c)** The timing jitter during this scan, extracted from (b). The red line shows a Gaussian fit with the FWHM of 84 as.

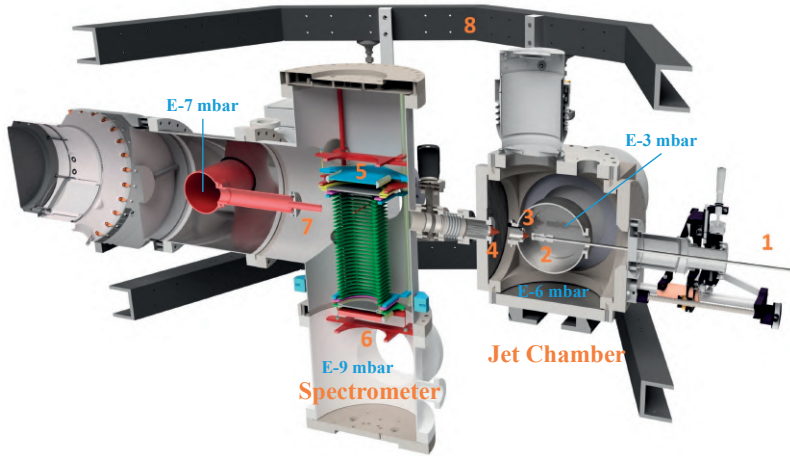


**Figure 3.7:** Drawing of the COLTRIMS spectrometer. (1) Gas inlet (2)  $50\ \mu\text{m}$  nozzle, (3)  $500\ \mu\text{m}$  skimmer, (4) 1 mm skimmer (5) ion detector (6) electron detector (7) beam dump (8) Helmholtz coils.

## 3.3 Detection Chamber

The electron-ion coincidence spectrometer used for these experiments is based on a CoLd Target Recoil Ion Momentum Spectroscopy (COLTRIMS) setup [64, 65]. With COLTRIMS it is possible to detect both ions and electrons from an ionization event with two separate detectors. If the count rates are kept low enough, such that there is at most one ionization event per laser shot, the electron and ion detected are originating from the same molecule and are therefore measured in coincidence. The key parts of the COLTRIMS setup are the electron-ion spectrometer together with the jet chamber for target preparation. Both will be described further in the remaining of this chapter.



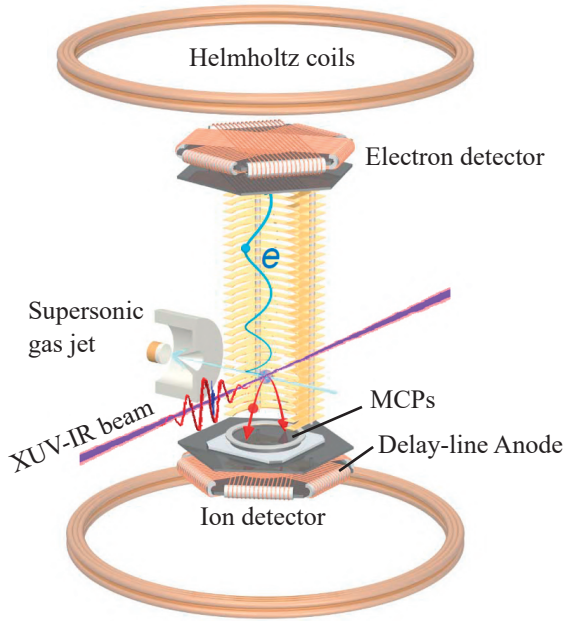


**Figure 3.8:** Illustration of the COLTRIMS spectrometer.

### 3.3.1 Electron and Ion Spectrometer

#### Spectrometer

The central part of the COLTRIMS is the spectrometer. It consists of a stack of copper plates, on which an electric field is applied to accelerate the charged particles towards the respective detector. The copper plates are parallel and separated by 5 mm, 600 k $\Omega$  strong resistors. A 15 mm cutout in two consecutive copper plates enables the XUV beam and the gas jet to enter the spectrometer and cross in its center. A homogeneous extraction field of 1-3 V/cm guides the electrons and ions to their respective detectors. For the ions the extraction field region is 40 mm long, while on the electron side it is 70 mm in length, followed by a 140 mm long field-free region. This 1:2 configuration of extraction and field-free region on the elec-

tron side, is known as Wiley-McLaren geometry [66]. It has the advantage of compensating the initial position spread along the time-of-flight axis, leading to an improved energy resolution. After the extraction/field-free region there is a 8 mm distance with an electric field of 1000 V/cm to increase the kinetic energy of electrons and ions before they hit the MCPs. To prevent stray fields from the high voltage into the extraction and field-free region, a mesh<sup>6</sup> is used to separate the regions. In addition to the electric field, there is a magnetic field applied through a pair of Helmholtz coils, with radius and distance between the coils of 0.6 m and 108 turns in each coil. With the Helmholtz coils a homogeneous magnetic field between 1-10 gauss is applied to the whole spectrometer region. This magnetic field has almost no effect on the ions, due to their high mass, but it forces the electrons on a helical trajectory with a gyration frequency of

$$\omega_{\text{gyr}} = \gamma B = \frac{eB}{m_e} \quad , \quad (3.2)$$

where  $\gamma$  is the gyromagnetic ratio,  $B$  the magnetic field strength,  $e$  the elementary charge and  $m_e$  the mass of the electron. This formula is also known as Larmor's equation [67], applying to any fermions. A schematic drawing of the spectrometer, including the positioning of the Helmholtz coils is shown in Figure 3.8.

## Detectors

The electron and ion detectors can also be seen in fig. 3.8. They consist of a pair of micro-channel plates<sup>7</sup> (MCP's) stacked in chevron configuration in combination with a three-layer delay-line anode<sup>8</sup> (Hexanode), both with an active diameter of 75 mm. The MCP's amplify any signal by prompting an electron avalanche due to the high voltage applied between the two plates ( $\sim 2$  kV). The electron avalanche triggers a short voltage drop at the MCP front, which - in combination with the laser trigger - provides the time-of-flight

---

<sup>6</sup>The mesh is formed by a bee-hive pattern with 1 mm large hexagons and 0.1 mm thick walls, transmission >80%

<sup>7</sup>Photonis USA, Inc.

<sup>8</sup>RoentDek GmbH

signal of the electrons and ions. The released electron cloud causes a further signal on each of the three layers of the delay-line anode, enabling a position detection of electrons and ions with a resolution of  $<0.1$  mm [68].

### 3.3.2 Jet Chamber

The molecular target is prepared via supersonic expansion of a gaseous sample. The adiabatic expansion of a gas from a high pressure region to low pressure results in rapid cooling of the gas sample, which is necessary to achieve sufficient momentum resolution for the ions [69]. A supersonic expansion of the gas is reached by expanding it under high pressure (1-5 bar) through a nozzle (Pos. 2 in 3.7) with a  $d=50$   $\mu\text{m}$  orifice into vacuum ( $10^{-3}$  -  $10^{-4}$  mbar). Behind the nozzle a *zone of silence* forms, where the momentum of the gas is uniform in magnitude and direction. In this zone, with 10 mm distance to the nozzle, a skimmer<sup>9</sup> with 500  $\mu\text{m}$  diameter is placed to form a molecular beam (Pos. 3 in 3.7). A second skimmer with 1 mm opening (Pos. 4 in 3.7) is put 30 mm further downstream to create two differentially pumped stages. After passing the spectrometer, the molecular beam enters another differentially pumped stage, serving as a beam dump through a 30 mm pinhole (Pos. 7 in 3.7). Thereby the ultra high vacuum ( $10^{-9}$  mbar) of the main chamber can be maintained, even with constant gas flow into the chamber. More information on the formation of molecular beams via supersonic expansion can be found in [70, 71].

The final temperature of the molecular beam can be estimated with

$$T_f = \frac{f + 2}{2} \frac{T_i}{S^2} \quad (3.3)$$

with the degrees of freedom  $f$ , the initial temperature  $T_i$  and the speed ratio  $S$ , defined as

$$S = \frac{v_{\text{Jet}}}{\sqrt{k_B T_i / m}}. \quad (3.4)$$

---

<sup>9</sup>Beam Dynamics, Inc

### 3.3. Detection Chamber

Here,  $v_{Jet}$  is the velocity of the molecular beam,  $k_B$  is the Boltzmann constant and  $m$  the molecular mass. Because it is experimentally difficult to accurately determine the speed ratio  $S$ , we use an empirical formula valid for small molecules [71] to get an estimation for the final temperature of the molecular beam:

$$S = 5.4 \cdot (0.75p_0d)^{0.32} \quad (3.5)$$

where  $p_0$  is the backing pressure of the target gas. With a typical backing pressure between 1-2 bar, this results in temperatures around  $T_f=40$  K for  $CF_4$  and  $T_f=10$  K for argon. To allow for pre-heating the sample, the nozzle and the tube connecting nozzle with gas inlet can be heated independently via heating elements and PID controllers. Additionally, a heatable bubbler can be used as gas inlet, as was done for measuring water clusters, which will be discussed in chapter 5.

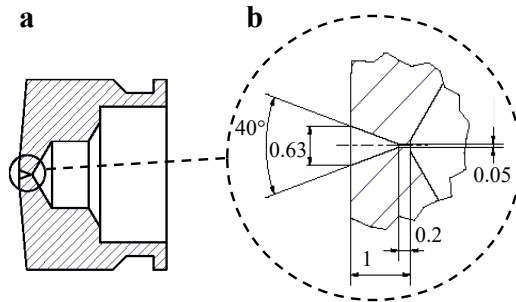


**Figure 3.9:** Drawing of the nozzle design. (a) Side cut through the nozzle, which is mounted on a swagelock connector. (b) Zoom into the nozzle orifice with numerical values given in mm.

The nozzle used throughout the experiments in this thesis, is a home-built conical and continuous nozzle with an opening of  $50 \mu\text{m}$  in diameter and an opening angle of  $40^\circ$  as shown in Figure 3.9.

### 3.3.3 Data Processing

The signals from MCPs and Hexanode are decoupled from the detector operating voltages with high-pass filters and are subsequently amplified by a high-frequency amplifier<sup>10</sup>. The amplified signals are transformed into NIM (Nuclear Instrument Methods) pulses via a constant fraction divider<sup>11</sup> (CFD), which allows for reliable signal detection independent of its height (as long as its above a set threshold). The NIM signals are then converted to digital signals by a time to digital converter<sup>12</sup> (TDC) and stored on a computer. The data is stored in a list mode file (.lmf) format, in which all signals are stored for each event separately. The following information is stored in the data file:

- MCP time signal  $t_{\text{MCP}}$ .
- Time difference between the two ends of each layer of the delay-line anode. For the hexanodes used in this setup with a signal and reference wire for each layer, this constitutes to six signals for each detector:  $t_u^{\text{sig}}$ ,  $t_v^{\text{sig}}$ ,  $t_w^{\text{sig}}$ ,  $t_u^{\text{ref}}$ ,  $t_v^{\text{ref}}$  and  $t_w^{\text{ref}}$ .
- Trigger signal  $t_{\text{trig}}$  of the laser pulses from a photodiode in the beamline (Pos. 3 in 3.2).
- Position of the delaystage.
- Number of recorded event, *eventcounter*.

#### Position and time-of-flight

The raw signals from the delay-line anode and MCP need to be converted to a position and a time-of-flight of each particle in order to calculate the momentum vectors. The time-of-flight is just the difference between the MCP time signals and the time of ionization  $t_{\text{ionization}} = t_{\text{trig}} + t_0$ :

---

<sup>10</sup>FAMP8c, RoentDek GmbH

<sup>11</sup>CFD8c, RoentDek GmbH

<sup>12</sup>TDC8HP, RoentDek GmbH

### 3.3. Detection Chamber

---

$$t_{\text{tof}} = t_{\text{MCP}} - t_{\text{ionization}} = t_{\text{MCP}} - t_{\text{trig}} - t_0, \quad (3.6)$$

where  $t_0$  is a constant time offset caused by the signal runtime in the cables.

The position on the detector in the coordinate system of the hexanode is calculated with

$$\begin{aligned} u &= u_{\text{scale}} \cdot t_u \\ v &= v_{\text{scale}} \cdot t_v \\ w &= w_{\text{scale}} \cdot t_w + O_w. \end{aligned} \quad (3.7)$$

Here  $u_{\text{scale}}$ ,  $v_{\text{scale}}$  and  $w_{\text{scale}}$  are scaling factors connecting the time differences in ns to a position in mm.  $O_w$  is a position offset of the w-layer to ensure that the origin of all layers coincide. The coordinates  $u$ ,  $v$  and  $w$  can be converted to the Cartesian coordinate system via

$$\begin{aligned} X_{uv} &= u, & Y_{uv} &= \frac{1}{\sqrt{3}}(u - 2v) \\ X_{uw} &= u, & Y_{uw} &= \frac{1}{\sqrt{3}}(2w - u) \\ X_{vw} &= v + w, & Y_{vw} &= \frac{1}{\sqrt{3}}(w - v). \end{aligned} \quad (3.8)$$

From the equations in (3.8) one notices the redundant information due to the three layers of the hexanode. This enables reconstruction of the position even if one layer fails.

### Momentum Reconstruction

With the position and time-of-flight information of electrons and ions, it is possible to reconstruct the three dimensional momentum vector after photoionization for both particles. In order to do this it is necessary to consider the forces acting on electrons and ions. This requires accurate information of the electric and magnetic fields to which the particles are exposed to.

The Lorentz force acting on a charged particle is

$$\vec{F}_L = q(\vec{\epsilon} + \vec{v} \times \vec{B}) \quad (3.9)$$

with the charge  $q$ , the velocity  $\vec{v}$ , the electric field  $\vec{\epsilon} = [0, 0, \epsilon_z]$  and magnetic field  $\vec{B} = [0, 0, B_z]$ . Since electric and magnetic field have only a component along the z-direction (corresponding to the tof-direction), equation (3.9) simplifies to

$$\frac{d\vec{v}}{dt} = \frac{q}{m} \begin{pmatrix} v_y B \\ -v_x B \\ \epsilon \end{pmatrix}, \quad (3.10)$$

where  $m$  is the mass of the particle. Solving the Newtons equation of motion for the x- and y-component yields following trajectories (see [69] for detailed calculation)

$$x(t) = \frac{m}{Bq} [v_{0,x} \sin(\frac{Bqt}{m}) + v_{0,y} (1 - \cos(\frac{Bqt}{m}))], \quad (3.11)$$

$$y(t) = \frac{m}{Bq} [v_{0,y} \sin(\frac{Bqt}{m}) - v_{0,x} (1 - \cos(\frac{Bqt}{m}))], \quad (3.12)$$

Here,  $v_{0,x}$  and  $v_{0,y}$  are the initial velocities in x- and y-direction. Further it is assumed that the starting point, i.e. the interaction region, coincides with the origin. For a respective spectrometer length  $L$  and the measured  $t_{\text{tof}}$ , the initial momentum of the particles can then be calculated with

$$p_{x,0} = -\frac{Bq}{2} \left( y + \frac{x}{\tan(Bqt_{\text{tof}}/(2m))} \right), \quad (3.13)$$

$$p_{y,0} = -\frac{Bq}{2} \left( x - \frac{y}{\tan(Bqt_{\text{tof}}/(2m))} \right). \quad (3.14)$$

The electrons are following a circular motion in the xy-plane with the gyration period  $T_{\text{gyr}} = 2\pi m / (Bq)$ , while the ions are so heavy that their x- and y-momentum simplifies to

$$p_{0,x}^{\text{ion}} = m \frac{x}{t_{\text{tof}}} \quad \text{and} \quad p_{0,y}^{\text{ion}} = m \frac{y}{t_{\text{tof}}}. \quad (3.15)$$

An analytical solution for the z-momentum is very complex for more than a single region (see [72] chapter 4.2). It is therefore better solved numerically using the Newton method [73]. Assuming three electric

field regions with lengths  $l_1$ ,  $l_2$  and  $l_3$ , the equation for the initial momentum in z-direction is

$$\frac{p_{0,z}}{m} = -a_1 t_{tof} + \left(1 - \frac{a_1}{a_2}\right) \sqrt{2a_1 l_1} + \left(\frac{a_1}{a_2} - \frac{a_1}{a_3}\right) \sqrt{2(a_1 l_1 + a_2 l_2)} \quad (3.16)$$

$$+ \frac{a_1}{a_3} \sqrt{2(a_1 l_1 + a_2 l_2 + a_3 l_3)}. \quad (3.17)$$

Here,  $a_n = q\epsilon_n/m$  is the acceleration for each field region. For each experiment the electric and magnetic field strengths were chosen carefully to ensure highest resolution and detection efficiency in the relevant region.

## 3.4 Data Analysis

In the initial processing step, the raw data in the list mode file format is converted to a *root* file. Root is an analysis program, developed by CERN (European Organization for Nuclear Research) and it is used for further analysis of our data. In this first step, the signals from delay-line anode and MCP are also converted to a position on the detector and a time-of-flight for electrons and ions, as described in chapter 3.3.3. The second step of the analysis, done in *root*, calculates the 3D momentum vectors and generates the RABBIT spectrograms. The third and last step of the analysis procedure deals with the phase-extraction from the RABBIT spectrograms, which allows for the determination of the photoionization time-delays. In the following section, the calibration methods for the first and second step are outlined and the phase extraction of the RABBIT spectrograms is explained.



### 3.4.1 Calibration

#### Time Offset

The time offset  $t_0$  in equation (3.6) needs to be determined in order to correctly calculate the time-of-flight of all particles. To do this it is possible to use the gyration motion of the electrons in the magnetic field. The trajectory of all electrons starts in the well defined interaction region and after each multiple of the gyration period the trajectory goes through this region again, in the plane orthogonal to the magnetic field. These nodes in the electron trajectories can clearly be seen in Figure 3.10, which plots electron time-of-flight versus the radial position on the electron detector. Because the first node is, by definition, at time zero, an extrapolation of the gyration period gives the time offset  $t_0$  in equation (3.6).

#### Hexanode

To convert the time signals from the delay-line anode to a position on the detector, the scaling factors and position offset of the third layer in equation (3.7) need to be determined. The scaling factors are dependent on the signal velocity and length of the wires. A rough estimate is given by the manufacturer<sup>13</sup> and the exact relative values are further optimized by an automatized algorithm [74], which also gives the offset  $O_w$  of the w-layer.

#### Magnetic Field

The magnetic field value  $B$  can be determined via the gyration period of the electron trajectories

$$T_{\text{gyr}} = \frac{2\pi m_e}{Be}, \quad (3.18)$$

where  $m_e$  is the mass and  $e$  the charge of an electron. The gyration period is the distance between two nodes in Figure 3.10. This plot can be generated for any magnetic field values if the electric field is

---

<sup>13</sup>RoentDek GmbH

set low enough so that the spread in time-of-flight contains at least two nodes. For a typical measurement the electric field is chosen to have the whole electron distribution either between two nodes or to be centered around a single node<sup>14</sup>.

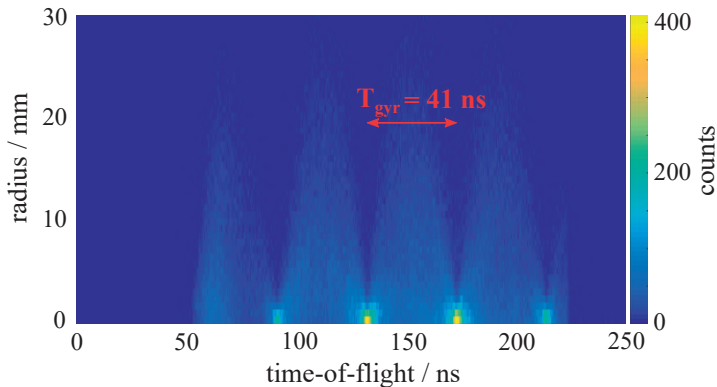


**Figure 3.10:** Radial electron position on the MCP detector versus their time-of-flight. The magnetic field can be determined by the distance of the nodes in the spectrum, which gives the gyration period  $T_{\text{gyr}}$  for the orbital trajectories of the electrons.

#### Electric Field

The electric field can be calibrated by centering the momentum distribution around the origin of the coordinate system. A correct value for the electric field results in a symmetric electron energy distribution in the polar angle  $\theta$  and azimuthal angle  $\varphi$ , as shown in Figure 3.11.

#### Momentum Scaling Factors

In the calculation of electron and ion momentum in 3.3.3, it is assumed that the magnetic and electric fields are homogeneous. Unfortunately this is not exactly the case, due to small field distortions

---

<sup>14</sup>The highest resolution is at tof values in between two nodes, while at the nodes all information is lost.

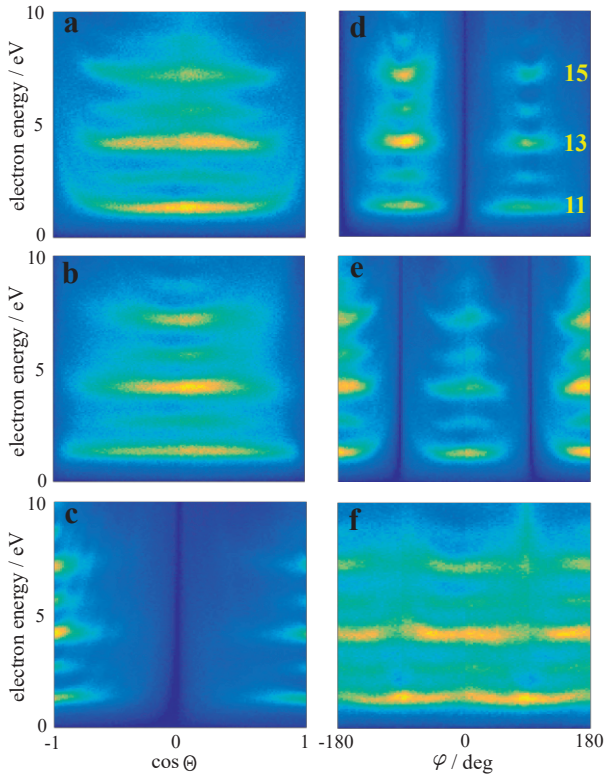


**Figure 3.11:** Electron energy versus different angles in the spherical coordinate system for ionization of argon with XUV and weak IR. (a)-(c) Polar angle  $\theta$  for zenith directions along x-, y- and z-axis respectively. (d)-(f) Azimuthal angle  $\varphi$  in the plane spanned by y- and z-axis, x- and z-axis and x- and y-axis respectively. The mainband peaks 11-15 are labeled in yellow.

from the high electric fields used in the MCP's and other disturbing electric and magnetic fields from laboratory equipment in the vicinity of the spectrometer. The effect of field inhomogeneities can be corrected to a good degree by linear scaling factors for the final momentum. The scaling factors are chosen, so that the final energy of electrons and ions is constant as a function of polar and azimuthal angle of the emission direction. Figure 3.11 shows plots of electron

energy as a function of different angles in the spherical coordinate system. The energy calibration is done by ionization of a reference gas with a well known ionization potential (e.g. argon) with a comb of XUV pulses with known photon energies. Due to the energy conservation in 2.2, we then also know the kinetic energies of the photoelectrons and a scaling factor for the absolute momentum can be adjusted to fit the expected energy values.

### 3.4.2 RABBIT

The final step in the analysis procedure deals with the phase extraction of the RABBIT spectrograms. To compare the photoionization time-delays for different target species or other parameters (such as emission angle, molecular orientation, KER, etc.), a RABBIT spectrogram for each condition is generated and treated separately in the subsequent analysis. This selection of specific event conditions is called *gating* and is possible, because each event is recorded individually with its full 3D momentum vector for both electron and ion.

The gating procedure sets specific conditions for events that constitute a RABBIT spectrogram. Such conditions can be set on the ion mass-over-charge ratio, specific kinetic energy release (KER) of a molecular fragmentation, molecular orientation (only in fragmentation channel), electron emission direction (in molecular and laboratory frame) and more. Figure 3.12 shows an example of three different RABBIT spectrograms obtained from a single measurement.

#### Phase Extraction

As described in detail in chapter 2.3, to get photoionization time-delays, it is necessary to extract the sideband phases from the RABBIT spectrogram. This can be done by fitting a function of the form  $I_{SB} = A + B \cos(2\omega_0\tau - \varphi)$  to the sideband intensity described by

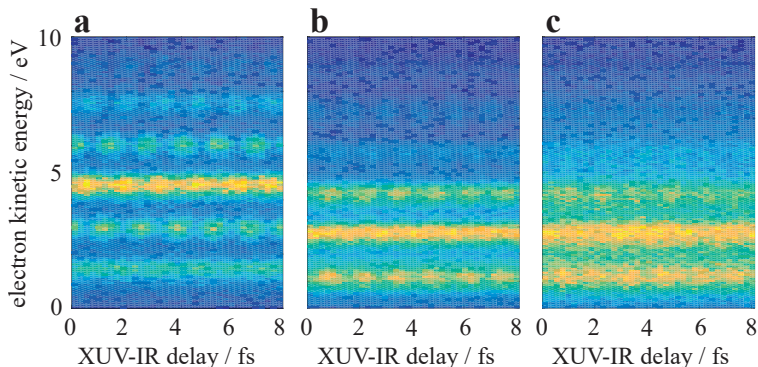


**Figure 3.12:** RABBIT spectrograms from a single measurement on an Ar-CF<sub>4</sub> gas mixture for different gating conditions. **(a)** Ar<sup>+</sup> and electron emission angle of  $\theta_{\text{Lab}}=0\text{-}18^\circ$  and  $\theta_{\text{Lab}}=162\text{-}180^\circ$  with respect to the XUV polarization. **(b)** CF<sub>3</sub><sup>+</sup> and electron emission angle of  $\theta_{\text{Lab}}=0\text{-}18^\circ$  and  $\theta_{\text{Lab}}=162\text{-}180^\circ$  with respect to the XUV polarization. **(c)** CF<sub>3</sub><sup>+</sup> and electron emission angle of  $\theta_{\text{Mol}}=155\text{-}180^\circ$  with respect to the molecular dissociation (recoil) axis, where  $0^\circ$  points along the CF<sub>3</sub><sup>+</sup> momentum vector. The linear false color scale shows the normalized counts.

equation 2.34, with fit parameters  $A$ ,  $B$  and  $\varphi$ . This approach is the most straightforward and very successful for atomic and molecular spectra without spectral overlap [16, 17, 28, 75, 76]. However, the experiments discussed in this thesis mostly deal with molecular species that have significant spectral overlap in the electron energy. To extract phases from those RABBIT spectrograms we therefore use a complex-valued principal components analysis (or *complex fit*) [33], which has previously been used to extract phases from congested RABBIT spectrograms [25, 26, 32].

### Complex Fit

The complex fit method, used throughout the work presented in this thesis, is based on the detailed description in [33]. In the first step we fit the static XUV-only electron spectrum using a set of Gaussians in order to get the relative XUV spectral intensities, cross sections

and spectral widths of the states involved. These parameters are then used in the second step, which consists of extending the fit to the one-dimensional energy spectrum of the XUV+IR electron spectrum by adding a set of Gaussians accounting for sidebands. For this, the time-resolved RABBIT spectrum is integrated over the delay axis. As a result, one obtains Gaussian fit parameters for each main- and sideband peak of the electronic states involved. Next, a Fast-Fourier Transformation (FFT) is done line by line on the photoelectron spectrum along the time-delay axis. The obtained band in the complex-valued FFT at the  $2\omega$  angular frequency component, is fitted by multiplying each Gaussian obtained in the XUV+IR fit with a complex-valued amplitude  $e^{z_j}$ :

$$I_{\text{fit}}(E) = \sum_j p_j(E) e^{z_j} = \sum_j \underbrace{e^{a_j} p_j(E)}_{A_j(E)} e^{ib_j}. \quad (3.19)$$

Here,  $p_j(E)$  is the Gaussian fit for the photoelectron band  $j$ ,  $A_j(E)$  is the Fourier amplitude related to the oscillation amplitude and  $b_j$  constitutes a phase value for each band  $j$ . An example of the complex fit procedure is shown in Figure 3.13.

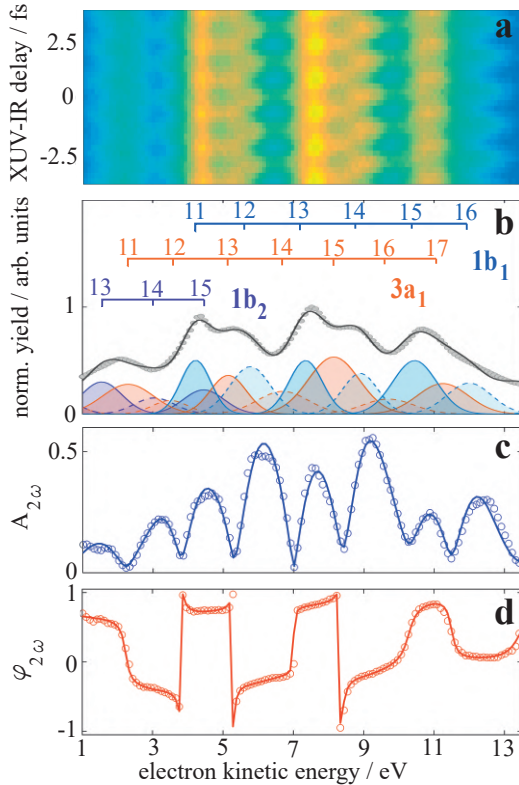


**Figure 3.13:** (a) RABBIT spectrogram of  $\text{H}_2\text{O}$ . (b) Gaussian fits on XUV+IR electron energy spectrum of  $\text{H}_2\text{O}$ . The inset indicates the main- and side-band position of the three accessible states. (c) Amplitude at  $2\omega$  of a Fourier Transformation of the RABBIT spectrogram shown in (a) (circles) and the amplitude of the complex fit (line). (d) Phase at  $2\omega$  of the same Fourier Transformation (circles) and the phase of the complex fit (line).





## Chapter 4

# Molecular-Frame-Resolved Photoionization Time Delays

Photoionization time delays are commonly treated in an angularly averaged fashion and only recently there has been growing interest to investigate the angular dependence of the ionization time delays in atoms with few experimental [17, 18, 20, 77] and theoretical [59, 77–80] studies focused on rare gases.

In molecules the angular dependence of ionization time delays is two-fold, since there is the angular dependence in the laboratory frame (i.e. with respect to the XUV polarization) and the angular dependence in the molecular frame (i.e. with respect to a specific molecular axis) [43]. The latter has, so far, only been examined very little due to the experimental challenges involved when aligning a molecule [27]. There are two possibilities to investigate ionization time delays in the molecular frame of a molecule. One is to align the molecule before it is ionized and the other is to detect the orientation of the molecule at the moment of ionization, which allows

---

post-selection of aligned molecules. The first is limited to polarized molecules [81] and requires the use of an additional synchronized laser pulse, while the latter is limited to the fragmentation channels of molecules satisfying the axial-recoil approximation<sup>1</sup> and it requires the detection of electrons and ions in coincidence.

So far, the only experimental investigation of ionization time delays in the molecular frame has been in 2018 by Vos and co-workers, where they used the electron-ion coincidence technique to measure stereo time-delays of CO [27], i.e. the left-right asymmetry of the photoionization delay, an experiment theoretically proposed by Chacon et al. [82]. There are, however, increasing theoretical efforts to understand the molecular-frame angular dependence of photoionization time delays [41, 43, 82, 83].

In this chapter the fully angular-resolved ionization time delays in the recoil frame of CF<sub>4</sub> are presented and discussed, significantly advancing the complexity of the target molecule and achieving detailed angular resolution (as opposed to left-right) for the first time. CF<sub>4</sub> has been chosen due to its prevalent fragmentation channel, resulting in CF<sub>3</sub><sup>+</sup> + F and for the presence of multiple shape resonances that are responsible for a pronounced angular structure in the RFPADs (Recoil-Frame Photoelectron Angular Distribution) [84] and make it a particularly interesting molecule to study the angular-resolved photoionization dynamics.

---

<sup>1</sup>The axial-recoil approximation is valid when the dissociation is fast compared to the molecular rotation. In a two-body breakup, the emission direction of the ion then coincides with the molecular axis.

---

Details about the publication printed in this chapter are listed below. Text and figures are as in the original publication. Only the style of text, figures and equations has been adapted to match the style used in this thesis. Further the numbering of figures and equations has been changed to match the numbering used throughout the thesis. The same is true for the reference list, which has been included into the reference list at the end of the thesis. The supplementary material, which is part of the original publication, is printed in Appendix A of this thesis.

**Title:** Attosecond Interferometry of Shape Resonances  
in the Recoil Frame of  $\text{CF}_4$   
**Journal:** Science Advances (2021), in press  
**License:** Creative Commons BY



## 4.1 Attosecond Interferometry of Shape Resonances in the Recoil Frame of CF<sub>4</sub>

Saijoscha Heck,<sup>1</sup> Denitsa Baykusheva,<sup>2†</sup> Meng Han,<sup>1</sup> Jia-Bao Ji,<sup>1</sup>  
Conaill Perry,<sup>1</sup> Xiaochun Gong<sup>1,3</sup> and Hans Jakob Wörner<sup>1†</sup>

<sup>1</sup> Laboratorium für Physikalische Chemie, ETH Zürich, 8093 Zürich, Switzerland,

<sup>2</sup> Department of Physics, Harvard University, Cambridge, Massachusetts 02138, USA

<sup>3</sup> State Key Laboratory of Precision Spectroscopy, East China Normal University, Shanghai, China

† E-mail: dbaykusheva@g.harvard.edu, hwoerner@ethz.ch.

Shape resonances play a central role in many areas of science, ranging from nuclear reactions over ultracold chemistry to DNA lesions induced by slow electrons. The real-time measurement of the associated many-body dynamics poses major challenges to the latest techniques of ultrafast science. Here, we present a direct measurement of recoil-frame angle-resolved photoionization delays (RAPIDs) in the vicinity of several shape resonances of CF<sub>4</sub> in combination with full electronic-state resolution. We apply this technique to obtain fundamental new insights into the spatio-temporal photoionization dynamics of molecular shape resonances. We find delays of up to  $\sim 600$  as in the HOMO channel with a strong dependence on the emission direction and a pronounced asymmetry along the dissociation axis. Comparison with quantum-scattering calculations traces the asymmetries to the interference of a small subset of partial waves at the low kinetic energies of the resonances and additionally by the interference of two overlapping shape resonances in the HOMO-1 channel. With increasing energy the time delays become symmetric as a consequence of a larger number of contributing partial waves. Our experimental and theoretical results establish a broadly applicable approach to space-time-resolved photoionization dynamics in the molecular frame.

### Introduction

Shape resonances are quasi-bound states of matter created by the presence of a potential-energy barrier. They play a crucial role in nuclear reactions [85], in cold and ultracold chemistry [86, 87], the existence of exotic ultralong-range molecules [88, 89] and scattering of low-energy electrons with molecules [90, 91]. They are also relevant for understanding dissociative electron attachment, which dominates radiation damage of DNA in aqueous solution [92–94]. In all of these cases, the presence of a potential barrier allows for an extended interaction time between the two unbound particles, which considerably impacts the outcome of the reaction. Most of these interaction times are ultrashort, ranging from femtoseconds in electron attachment to well below one attosecond in nuclear reactions [95]. Hence, a real-time study of the associated many-body dynamics lies at the frontier of present-day capabilities.

A particularly interesting class of shape resonances arises in the context of molecular photoionization. They are created by the combination of the short-range, Coulomb and centrifugal potentials [38] and are therefore sensitive to subtle electron-correlation effects. Following photoabsorption, the electron can be trapped in a shape resonance until it tunnels through the associated potential barrier. The lifetime and the energy at which the resonance occurs are a fingerprint of the underlying multi-electron dynamics. Shape resonances have so far mainly been identified as local maxima in photoionization cross sections, and/or rapid variations in the asymmetry parameter [38], but their definitive identification and characterization has remained challenging [96, 97]. With the advent of attosecond science, time-domain access to shape resonances has become possible [29, 76, 98, 99], but a state- and angle-resolved characterization of these time delays has so far not been achieved.

In this work we demonstrate an experimental method that, for the first time, completely resolves the attosecond photoionization dynamics of non-linear molecules in their recoil frame and the final states of the cation. Our technique thereby simultaneously reveals

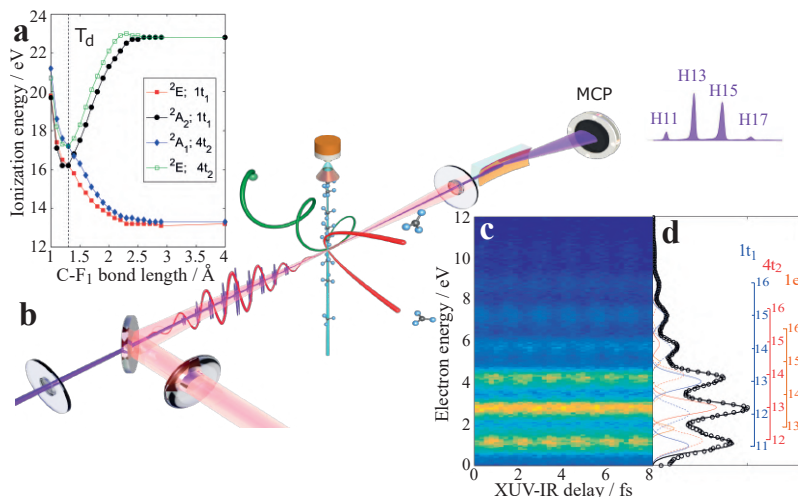


**Figure 4.1: Experimental Overview** (a) Potential-energy curves of the relevant states of  $\text{CF}_4^+$  as a function of the C-F bond length. The state labelling is according to  $C_{3v}$  symmetry of the final state and  $T_d$  symmetry of the ionized orbital. The energy scale was chosen to reflect the experimental vertical ionization energies. Details of the calculations are given in the SM, Section 1.5. (b) Sketch of the experimental setup. The ionic fragments and emitted photoelectrons are measured in coincidence as a function of the XUV-IR delay. The XUV APT is spectrally characterized via an online soft-X-ray spectrometer. (c) RABBIT spectrogram of  $\text{CF}_4$  for  $\theta = 0 - 18^\circ$ . (d) Photoelectron spectrum of  $\text{CF}_4$  created by the APT. The photoelectron bands of the three energetically accessible states are fitted according to their partial cross sections and relative XUV intensities using sums of Gaussians.

#### 4.1. Attosecond Interferometry of Shape Resonances in the Recoil Frame of CF<sub>4</sub>

---

the temporal and the angular manifestations of shape resonances in CF<sub>4</sub> and provides unprecedented information on their photoionization dynamics. Our experimental approach is based on attosecond interferometry, also known as RABBIT (Reconstruction of Attosecond Beating By Interference of Two-photon transitions) [60, 100, 101] in combination with an electron-ion coincident 3D momentum imaging detection scheme (COLTRIMS) [64, 65], as recently applied to atoms and linear molecules [27, 102–105]. This combination of techniques makes it possible to access ionization time delays in the molecular frame of a molecule. Previous work on CO [27] has been limited to a left-right asymmetry, previously called “*stereo*” time delay [82]. Accessing photoionization dynamics in the molecular frame can give detailed insight into the ionization process of molecules and has drawn recent theoretical interest [82, 83, 98, 106]. In contrast to prior work, we achieved full angular- and final-state resolution for the first time.

In RABBIT measurements the amplitude of the sideband oscillates as a function of the time delay  $\tau$  between IR and extreme-ultraviolet (XUV) pulses as

$$I_{SB} = A + B * \cos(2\omega_{IR}\tau - \Phi_{XUV} - \Phi_{Mol}), \quad (4.1)$$

where A and B are constants,  $\omega_{IR}$  is the IR probe frequency,  $\Phi_{XUV}$  is spectral phase of the attosecond pulse train (APT, containing the attochirp) and  $\Phi_{Mol}$  is the molecule-specific phase term. In our experiments, described in more detail in the materials and methods section, the XUV and IR fields are focused into a molecular beam as shown in Fig. 4.1 b. Using argon and CF<sub>4</sub> in a gas mixture allows us to reference the extracted photoionization time delays of CF<sub>4</sub> against the time delays in argon, which eliminates the contribution of the attochirp and minimizes the influence of the continuum-continuum delays due to the similar ionization potentials.

Upon ionization, CF<sub>4</sub> dissociates into CF<sub>3</sub><sup>+</sup> and F, which lowers the initial T<sub>d</sub> symmetry to C<sub>3v</sub>. The time scale of this dissociation has been recently determined to be only 40 fs [58], which is considerably



faster than the rotational period of the molecule [107, 108]. As a consequence, the momentum vector of CF<sub>3</sub><sup>+</sup> is, in excellent approximation, oriented parallel to the C-F axis in the molecular frame (axial-recoil approximation) as illustrated in the top panel of Fig. 4.3. This leads to a highly accurate determination of the electron-emission direction with respect to the dissociating C-F axis in the recoil frame. By detecting the full 3D momentum vector of the ion in coincidence with the 3D momentum vector of the electron, we are therefore able to analyze attosecond photoelectron spectra (RABBIT traces) and extract photoionization time delays for specific electron emission angles  $\theta$  in the recoil frame.

One of the main challenges in extracting photoionization time delays from molecular spectra is the spectral congestion that is caused by the broad bandwidth of XUV-APTs in combination with broad photoelectron spectra. We solved this problem by using the complex-valued principal-component analysis (CVPCA) [33]. A description of this analysis method is given in the materials and methods section. The experimental results are supported by ab-initio quantum-scattering calculations of the RABBIT time delays that are angle dependent, both in the laboratory frame as well as in the molecular frame (see methods and Appendix A for more details).

## Results and Discussion

In a first step, we investigate the shape resonance found in the vicinity of the electronic ground state of CF<sub>4</sub><sup>+</sup>, where we find a photoionization time delay of up to  $\sim 600$  as, relative to argon, which is caused by the resonance. Next, we investigate the time delay in the recoil frame of CF<sub>4</sub>, where we find a pronounced asymmetry in the delays for low kinetic energies. The ionization potentials of the four outer-valence orbitals of CF<sub>4</sub> (...3t<sub>2</sub><sup>6</sup> 1e<sup>4</sup> 4t<sub>2</sub><sup>6</sup> 1t<sub>1</sub><sup>6</sup>) are 22.12, 18.50, 17.49 and 16.20 eV, respectively [109, 110]. Photoionization from one of these orbitals results in CF<sub>4</sub><sup>+</sup> in the states  $\tilde{C}^2T_2$ ,  $\tilde{B}^2E$ ,  $\tilde{A}^2T_2$  or  $\tilde{X}^2T_1$ . None of these CF<sub>4</sub><sup>+</sup> states are stable. The  $\tilde{C}$  state dissociates into CF<sub>2</sub><sup>+</sup> + F<sub>2</sub> and CF<sub>2</sub><sup>+</sup> + F + F, whilst the  $\tilde{B}$ ,  $\tilde{A}$  and  $\tilde{X}$  states dissociate into

#### 4.1. Attosecond Interferometry of Shape Resonances in the Recoil Frame of $\text{CF}_4$

---

$\text{CF}_3^+ + \text{F}$  [111, 112]. Due to the prominence of the latter two states in the photoelectron spectrum, we focus exclusively on the  $\tilde{\text{A}}$  and  $\tilde{\text{X}}$  states, the potential-energy surfaces of which are shown in Fig. 4.1 a. We did not observe any  $\text{CF}_2^+$  in our ion mass spectra.

The photoionization cross section of the  $1t_1$  orbital has a prominent maximum in the  $1t_1 \rightarrow kt_2$  (where  $k$  indicates a continuum state) channel around 2.5 eV (see blue curve in Fig. 4.2 a), which corresponds to the energy of an electron from sideband 12. This overlap in the energy makes this particular sideband perfectly suited to investigate the signatures of the shape resonance. At this point we note that the exact energy of the resonance is debated in the literature [108, 113], but our theoretical results and experimental observation (see Fig. 4.1d) are consistent with those reported by Carlson et al. [113] and Larsen et al. [108] that suggest that the photoionization cross section is enhanced below 3 eV due to the influence of the shape resonance. The results are shown in Fig. 4.2a, where the ionization delays of the  $\text{CF}_4$   $1t_1$  channel referenced to the delay of the  $3p$  electron in argon are shown as a function of the electron kinetic energy. Argon was chosen due to its similar ionization potential (15.76 eV [114]) to the  $\tilde{\text{X}}$  state of  $\text{CF}_4^+$ , which leads to a near-cancellation of the continuum-continuum contribution  $\tau_{cc}$  to the measured delays, because  $\tau_{cc}$  only depends on the electron-kinetic energy [59, 98]. In our calculations we account for the small difference in ionization potentials by referencing  $\text{CF}_4$  electrons with energy  $E_{\text{kin}}^{\text{CF}_4}$  to argon electrons with energy  $E_{\text{kin}}^{\text{Ar}} = E_{\text{kin}}^{\text{CF}_4} + I_p^{\text{CF}_4} - I_p^{\text{Ar}}$  (where  $I_p^{\text{CF}_4}$  refers to either HOMO and HOMO-1). All delays shown throughout this manuscript, both experimental and theoretical, are referenced to the argon delays with electron emission parallel to the XUV polarization direction.

For channel  $1t_1$ , a delay of 614 ( $\pm 190$ ) as is observed at the energy of the shape resonance, which is significantly larger than any previously measured time delays, even in the presence of shape resonances [29, 76, 99]. In Fig. 4.2 c we show the wavefunctions of the

## 4.1. Attosecond Interferometry of Shape Resonances in the Recoil Frame of CF<sub>4</sub>

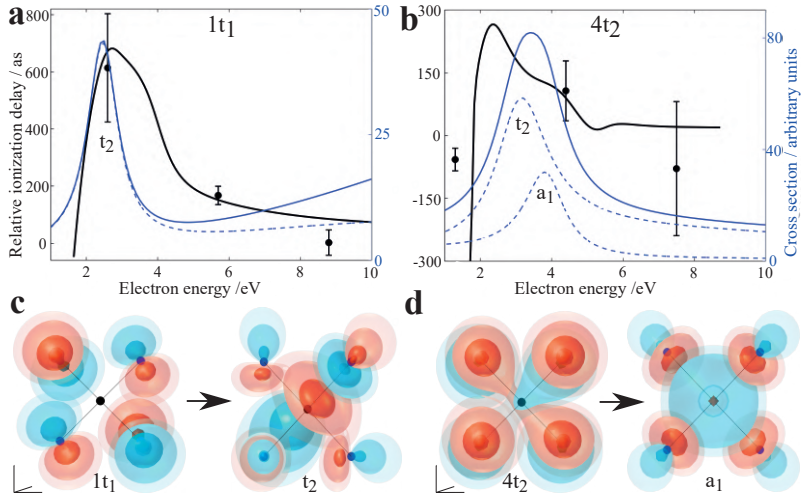


**Figure 4.2: Laboratory-Frame Ionization Delays and Shape Resonances.** Photoionization delays of the (a)  $1t_1$  channel and (b)  $4t_2$  channel. Black filled circles show the experimental values, the black solid line shows the calculated RABBIT delays, including the cc-contribution (see section Materials and Methods for detailed information), the blue solid line is the total cross section including all symmetries and the blue dashed lines are the symmetry-resolved cross sections for  $t_2$  and  $a_1$ . All cross sections are calculated within the same theoretical framework as the delays. Both experimental and theoretical delays are for electrons emitted  $0\text{-}18^\circ$  with respect to the XUV polarization and are referenced to argon using the same angular integration range. The error bars show the standard deviation of the delays extracted from multiple data sets. (c) Three-dimensional orbital wavefunctions for the  $1t_1$  HOMO (left) and the  $t_2$  dipole-prepared wavefunction at the resonance energy (right). The electric field vector of the dipole transition was chosen to lie along one of the C-F bonds, thus creating a superposition of all three degenerate wavefunction components  $1/\sqrt{3}(1t_1^{(x)} + 1t_1^{(y)} + 1t_1^{(z)})$ . (d) Same as (c), but for  $4t_2$  HOMO-1 and its dipole-prepared resonant  $a_1$  wavefunction. Contour levels used are: 0.8, 0.7, 0.35, 0.15 and 0.09. Alternative versions of (c) and (d) using different contour-level values are shown in Fig. A16.

#### 4.1. Attosecond Interferometry of Shape Resonances in the Recoil Frame of $\text{CF}_4$

---

bound orbitals, as well as those of the  $t_2$  photoionization continuum at resonance (the calculation procedure is described in Appendix A). It is evident that the continuum wavefunction has a local maximum at the position of the carbon atom, which is a signature of the cage effect [115]. It additionally has sizable amplitudes on each of the fluorine atoms, which is a necessary condition for being optically accessible from the  $1t_1$  orbital that has no wavefunction amplitude on the carbon atom. This shape resonance is thus truly molecular in character and bears little resemblance to the typical atomic shape resonances arising solely from potential barriers induced by the centrifugal term. The continuum part of the wavefunction is not visible in the plots, due its lower amplitude. A different version of the plots, with a lower iso-contour threshold and hence more visible continuum parts of the wavefunction is shown in Fig. A16 The measured and calculated RABBIT delays agree well with the calculated lifetime of the shape resonance (650 as, see Table A1). This agreement is, however, fortuitous because the choice of a larger angular integration range leads to smaller RABBIT delays (210 as for complete angular averaging). Generally it is difficult to find a simple relationship between RABBIT delays and resonance lifetimes. A possible reason for this is the interference between resonant and non-resonant photoionization channels (in the sense of a Fano treatment) [116]. In cases where the non-resonant contributions are not negligible (as is the case in  $\text{CF}_4$ , see Figs. A8-A9), the Wigner delays deviate from the resonance lifetimes. This is the case because the phase of the photoionization matrix elements is affected by the interference between resonant and non-resonant contributions, which leads to time delays that can significantly deviate from the lifetime of the shape resonance.

The  $4t_2$  channel has two overlapping shape resonances with symmetries  $t_2$  and  $a_1$  and partial cross sections shown in Fig. 4.2 b. Experimentally, we measured a delay of 107 ( $\pm 71$ ) as close to resonance and negative delays of -57 ( $\pm 27$ ) as for energies below and -79 ( $\pm 160$ ) as above the resonances. In Fig. 4.2 d we show the  $4t_2$  orbital and the  $a_1$  continuum wave function at the energy of the corre-

sponding shape resonance. The transition to the  $t_2$  shape resonance is shown in Fig. A15. Both shape resonances in the  $4t_2$  channel also have a local maximum at the position of the carbon atom, as well as amplitude on the fluorine atoms. They also display a strong molecular character and the characteristic signatures of the cage effect.

Our RABBIT calculations agree very well with the experiment for both HOMO and HOMO-1 with the exception of the very low kinetic energy (1.3 eV) of sideband 12 of the HOMO-1. This energy cannot be accessed by our RABBIT calculation, because the absorption pathway would go through negative kinetic energies. Experimentally this is achieved by populating high-lying autoionizing Rydberg resonances below the  $4t_2$  threshold. A decrease towards negative delays for very low electron energies is nevertheless correctly described and overall we find excellent agreement between theory and experiment, which is remarkable for this low-energy range.

Next we look into the Recoil-frame Angle-resolved PhotoIonization Delays (RAPIDs), where we extract the photoionization time delays for specific electron-emission directions relative to the dissociation axis of  $\text{CF}_4^+$  being parallel to the XUV polarization, as illustrated in Fig. 4.3. Since  $\text{CF}_3^+$  remains intact, we cannot access the absolute orientation of  $\text{CF}_3^+$  about that axis. In our calculations this is accounted for by isotropically averaging over the azimuthal angle  $\phi$ . This approach has previously been successfully applied to the dissociative ionization of  $\text{CF}_4$  [108, 117] and resulted in very precise RFPADs (Recoil Frame Photoelectron Angular Distributions).

Figure 4.3 shows the RAPIDs for sidebands 12, 14 and 16 of the  $1t_1$  channel. The most striking feature is the asymmetry of the ionization delays along the dissociation axis with the delay being 250 as larger for the electron emitted along the  $\text{CF}_3^+$  direction in sideband 12 (Fig. 4.3 a). Interestingly, this asymmetry changes direction for higher electron energies, i.e. at sideband 14 where the delay is  $\sim 40$  as larger for electrons emitted in the direction of the neutral fluorine fragment (Fig. 4.3 b). For the even higher electron energies

## 4.1. Attosecond Interferometry of Shape Resonances in the Recoil Frame of $\text{CF}_4$

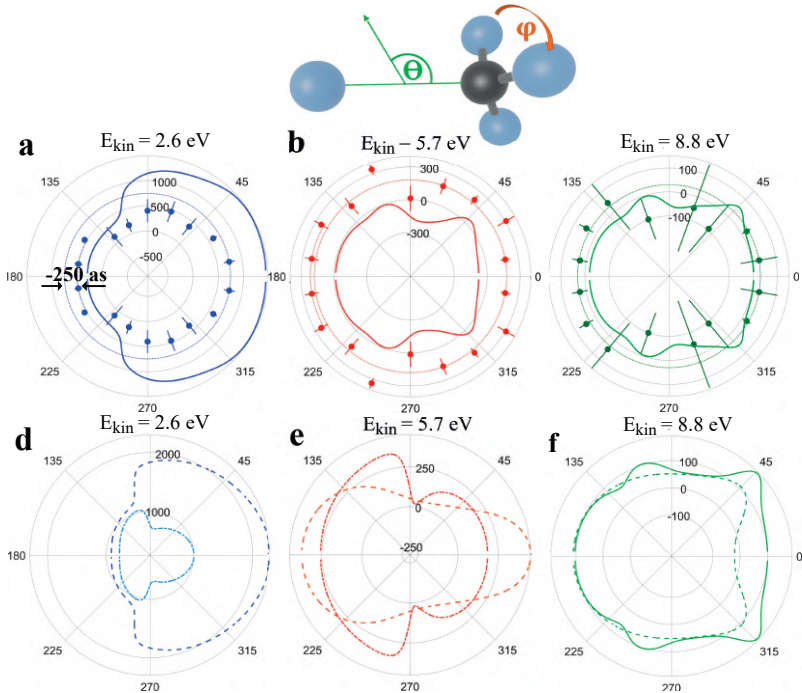


**Figure 4.3: Recoil-Frame Angle-Resolved Photoionization Delays of  $1t_1$ .** Photoionization delays of the  $1t_1$  (HOMO) channel (relative to argon) shown in the recoil frame of  $\text{CF}_4$ . Experimental data (filled circles) is shown together with the calculated RABBIT delays, including all symmetries, partial waves and cc-contribution (thick line), in (a) for sideband 12, (b) sideband 14, and (c) sideband 16. Kinetic energies pertain to  $\text{CF}_4$  electrons. A dashed circle is drawn into the plots to guide the eye. (d), (e) and (f) show the theoretical RABBIT delays relative to argon for the partial-wave combinations of  $l=2,3$  (dot-dashed),  $l=1-3$  (dashed),  $l=1-4$  (thin line, only in f) for the  $t_2$  continuum symmetry. For the partial-wave resolved delays, shown in d-e, the cc-contribution and the argon reference delays are omitted. The schematic drawing of a  $\text{CF}_4$  molecule visualizes the relevant angles.  $\theta$  is plotted in the polar plots and  $\phi$  is averaged over, both in experiment and in theory. In all cases the molecular dissociation axis is chosen parallel to the XUV polarization. All plots are mirrored vertically and error bars show the standard deviation of the delays extracted from multiple data sets. More information on the error analysis and the theoretical calculations is presented in the material and methods section.

of sideband 16, the asymmetry becomes even smaller in the experiment and the delays for emission along the molecular dissociation axis is almost symmetric (Fig. 4.3 c).

These results are qualitatively reproduced in our calculations and can be explained by a partial-wave decomposition of the RABBIT delays. The asymmetry is caused by the interfering contributions of several partial waves at the resonance. At the resonant energy, the contributions of partial waves with  $l=2$  and  $l=3$  are enhanced (Fig. A8), which causes the RAPID to be dominated by only those two partial waves (Fig. 4.3 d). The interference of two partial waves of opposite parity is known to cause maximal asymmetries in the photoelectron angular distributions [118], which is also true in MF-PADs. Our calculations show that such asymmetries also appear in the RAPIDs. The lack of quantitative agreement highlights the difficulty of electron-molecule scattering calculations at low kinetic energies, in particular in the presence of resonances. It is indeed mainly the sum of those two partial waves, which causes the strong asymmetry observed, as can be seen in Fig. 4.3 d. In this case the photoionization dipole matrix element experiences a sign change as a function of energy, which is responsible for a phase shift and results in an inversion of the delay asymmetry from sideband 12 (Fig. 4.3 a/d) to sideband 14 (Fig. 4.3 b/e). Adding more partial waves suppresses the delay asymmetry, yielding almost isotropic delays at the highest sideband resolved in the experiment (SB16) shown in Fig. 4.3 c. Interestingly, the shape of the RABBIT delays in Fig. 4.3 e and 4.3 f are qualitatively very similar, which is a consequence of partial waves contributing with equal weights at energies above the resonance. The energy-dependent asymmetry observed in the RAPIDs must therefore be a final-state effect, as opposed to the interpretation of the stereo time delays in CO [27], which was based on a pure initial-state effect.

A similar behavior is observed in the RAPIDs of the  $4t_2$  channel, shown in Fig. 4.4, where the ionization-delay asymmetry between the CF<sub>3</sub><sup>+</sup> and F direction is 105 as in sideband 12 and 160 as in side-

## 4.1. Attosecond Interferometry of Shape Resonances in the Recoil Frame of $\text{CF}_4$

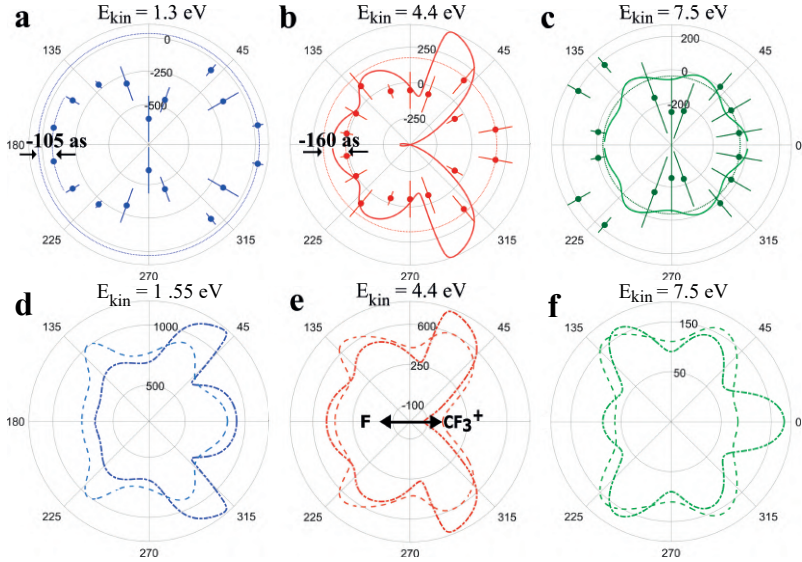


**Figure 4.4: Recoil-Frame Angle-Resolved Photoionization Delays of  $4t_2$ .** Photoionization delays of the  $4t_2$  channel referenced to argon shown in (a) for sideband 12, (b) sideband 14 and (c) sideband 16. Kinetic energies given are for  $\text{CF}_4$  electrons. A dashed circle is drawn into the plots to guide the eye. The filled circles represent the experimental data and the solid line the calculated RABBIT delays, including all symmetries, partial waves as well as the cc-contribution. (d), (e) and (f) show the coherent (dot-dashed) and incoherent (dashed) sum of RABBIT delays of continuum symmetries  $a_1$  and  $t_2$  restricted to the contributions of partial waves  $l=0-4$ . For the partial-wave resolved delays, shown in d-e, the cc-contribution and the argon reference delays are omitted. In both experiment and theory the molecular dissociation axis is parallel to the XUV polarization. All plots are mirrored vertically. Note that the RABBIT calculation is not defined for (a), due to the low energy. For this reason an energy of 1.55 eV was chosen for (d).



#### 4.1. Attosecond Interferometry of Shape Resonances in the Recoil Frame of $\text{CF}_4$

band 14 (larger delays towards the  $\text{CF}_3^+$  fragment) before it becomes symmetric in sideband 16. The  $4t_2$  channel is particularly interesting to study because it contains two overlapping shape resonances of different continuum symmetries, i.e.  $a_1$  and  $t_2$ . The two resonances are close in energy, couple to the same total final-state symmetry and show strong intra-channel coupling as identified in RFPAD measurements [108]. The two resonances have different partial-wave contributions as shown in Fig. A9, with the main contributions for symmetry  $a_1$  being  $l=0, 3$  and  $4$ , while for symmetry  $t_2$  it is  $l=1, 2$  and  $3$ . Qualitatively the asymmetry in the RAPID of sideband 12 can be described by a single-channel calculation for  $a_1$  symmetry using only the dominant partial waves  $l=0, 3$  and  $4$  (see Fig. A9). This is not the case for sideband 14 with an electron energy of  $E_{kin}=4.4$  eV just on the resonance. Neither single-channel calculations for  $a_1$  or  $t_2$  are able to qualitatively reproduce the experimental RAPID. Even the full RABBIT calculation including all partial waves and symmetries (Fig. 4.4 b) does not result in perfect agreement, since the peaks at  $\theta=60^\circ$  and  $\theta=120^\circ$  are reproduced, but the local maximum at  $\theta=0^\circ$  is not. This result highlights the pronounced sensitivity of RAPIDs to the finest details of the photoionization dynamics. Whereas the agreement of the calculated laboratory-frame delay at SB14 with experiment is excellent (Fig. 4.2 b) the deviation in the angle-resolved delays amounts to more than 600 as. Interestingly, a discrepancy between experiment and theory close to  $\theta=0^\circ$  is also visible in the RFPADs recorded in the immediate vicinity of SB14 ( $E_{kin} = 4.3$  eV, see Fig. A6 c). Notably, our calculations agree almost perfectly with the RFPAD calculations including channel coupling [108], but neither of the calculations reproduces the local maximum of the RFPAD in the vicinity of  $\theta=0^\circ$ . In an attempt to go beyond the fixed nuclei approximation, we also varied the C-F bond lengths within the Franck-Condon region, which, however, did not result in better agreement. Since both RFPADs and RAPIDs are sensitive to the amplitudes *and* phases of the photoionization matrix elements, the observed discrepancies suggest that the accuracy of molecular photoionization calculations needs to be improved further and that RAPIDs are a particularly sensitive benchmark for such work.

#### 4.1. Attosecond Interferometry of Shape Resonances in the Recoil Frame of $\text{CF}_4$

---

For higher energies of sideband 16 ( $E_{kin}=7.5$  eV), the agreement between RABBIT delays and experiment is again quite good. The delays are almost symmetric with respect to emission along the dissociation axis, which is a result of the contribution of multiple partial waves, similar to the case of the HOMO channel. A striking feature unique to the RAPIDs of HOMO-1 are the pronounced local maxima at  $\theta=60^\circ$  and  $\theta=120^\circ$ , particularly obvious in the complete calculation shown in Fig. 4.4 b. Those "ears" are a direct result of the interference between the two shape resonances of different symmetries and only appear clearly when adding both symmetries coherently. This is shown in Fig. 4.4 d-e through a comparison of the incoherent and coherent sums of symmetries  $a_1$  and  $t_2$ .

In conclusion, we have reported the first angle- and state-resolved measurements of molecular photoionization delays. We have applied this new capability to characterize the photoionization dynamics of  $\text{CF}_4$  in the vicinity of several shape resonances. In the case of the HOMO channel we measured time delays of up to 614 as caused by electron trapping enhanced by a molecular cage effect. In the case of the HOMO-1 channel we have additionally identified the effects of the interference between two shape resonances of different continuum symmetries on the molecular-frame-resolved photoionization delays. The highly structured and asymmetric time delays in the recoil frame of the molecule and in the vicinity of the shape resonances are qualitatively reproduced by our first-principles quantum-scattering calculations. They are explained in terms of a partial-wave analysis, tracing the reason for the asymmetry to the dominant contribution of only 2-3 partial waves at the resonances. The good overall agreement of experiment and theory, combined with the notable disagreement close to the overlapping shape resonances in the HOMO-1 channel, demonstrates the sensitivity of RAPIDs to the finest details of molecular photoionization dynamics and therefore their considerable potential as benchmarks for future theory developments. These results establish RAPIDs as a sensitive observable for characterizing multi-electron attosecond

dynamics in molecules and improving the description of electron correlation in theoretical methods. The demonstrated experimental and theoretical methods can be readily extended to more complex molecular systems, including e.g. nucleoside anions, which could be used to time resolve the attosecond dynamics underlying dissociative electron attachment and the resulting DNA strand breaks that mediate radiation damage.

## Materials and Methods

### Attosecond Pulse Generation

The optical setup consists of a regeneratively amplified Titanium-Sapphire laser system which delivers 1.2 mJ pulses at 5 kHz repetition rate with a pulse duration of 35 fs (FWHM) and a central wavelength of 800 nm. The laser beam is divided into two pathways with a 70:30 beam splitter, where the more intense part is focused into xenon gas for high-harmonic generation (HHG), resulting in odd harmonics up to 17th order ( $\cong 26.3$  eV). After the HHG cell, a 100-nm thick metallic filter (either aluminum or tin) is placed in front of a nickel-coated toroidal mirror ( $f=50$  cm) to eliminate any residual IR in the XUV path. The less intense part of the initial beam is recombined with the XUV pulse after the toroidal mirror to constitute a Mach-Zehnder interferometer. The path-length difference is controlled by a piezoelectric motor (PI, resolution 0.1 nm). The relative delay between the IR and XUV pulses is actively stabilized in an interferometric approach using a frequency-stabilized helium-neon laser coupled into the XUV-IR Mach-Zehnder interferometer [119], resulting in a time jitter ranging from 40 to 60 as.

### Coincidence Spectrometer

The phase-locked XUV and IR pulses are co-linearly focused into a supersonic gas-jet in a COLTRIMS (COLD Target Recoil Ion Momentum Spectroscopy) spectrometer [64, 65], where the electrons and ions are guided by a weak homogeneous electric field (1-3 V/cm) onto two opposite position- and time-of-flight sensitive detectors. A homogeneous magnetic field (4.2-5.9 Gauss) is additionally applied via a pair of Helmholtz coils, which is tilted to compensate for the earth magnetic field. Each detector consists out of two 75-mm diameter micro-channel plates (Photonis) in Chevron configuration in combination with a three-layer delay-line anode (HEX) with a crossing angle of 60 degrees between the adjacent layers and an active radius of 40 mm (RoentDek). The spectrometer for the electron side consists of a 70-mm extraction region, followed by a 140-mm electric-field-free region. On the ion side the length of the extraction region is 40 mm. Using COLTRIMS we gain access to the full three-dimensional momentum vectors of ions and electrons in  $4\pi$  solid angle. To ensure coincidence detection of ions and electrons the maximum ion count rate was set to 0.3 counts per laser shot. The Ar-CF<sub>4</sub> gas mixture is supersonically expanded into the vacuum chamber through a 50- $\mu$ m diameter nozzle with a backing pressure of 1 bar. Two conical skimmers are located 10 mm and 30 mm behind the nozzle with a orifices of 500  $\mu$ m and 1 mm respectively, as a part of a differential-pumping scheme. The supersonic gas jet is captured by a differentially pumped beam dump after crossing the spectrometer.

### Data Analysis

Ten data sets of CF<sub>4</sub>-Ar gas mixtures were measured, partially under different experimental conditions to optimize the data quality at the low- and high-energy ranges. Parameters that were varied are the HHG phase-matching conditions, such as the xenon gas pressure and the IR intensity, the metallic filter (either Al or Sn), the electric extraction field in the COLTRIMS as well as the magnetic field.

#### 4.1. Attosecond Interferometry of Shape Resonances in the Recoil Frame of CF<sub>4</sub>

The data were then analyzed for argon and CF<sub>4</sub> separately, using a complex-valued principal components analysis (CVPCA), which has been introduced in Jordan et al. [33] and since then successfully used to extract phases in spectrally congested time-resolved electron spectra [25, 26, 120]. The CVPCA is implemented as follows. First we fit the static XUV-only photoelectron spectra using a set of Gaussians in order to get the correct fit parameters describing the relative XUV spectral intensities, cross sections and spectral widths of the states involved. In a second step we fit the 1-D energy spectrum of the time-resolved XUV-IR measurement, obtained by integration over all time delays, using the fitting parameters from the XUV-only fits plus an additional set of Gaussians accounting for the sidebands (see Fig. A17 b in the Appendix A). Then, a Fast-Fourier Transformation (FFT) is done line by line on the photoelectron spectra along the time-delay axis. The obtained band in the complex-valued FFT at the  $2\omega$  angular frequency is fitted by multiplying each Gaussian component obtained in the XUV+IR fit with a complex-valued amplitude  $e^{z_j}$

$$I_{fit}(E) = \sum_j p_j(E)e^{z_j} = \sum_j \underbrace{e^{a_j} p_j(E)}_{A_j(E)} e^{ib_j}, \quad (4.2)$$

where  $p_j(E)$  is the Gaussian fit for the photoelectron band  $j$  (see Fig. A17c-d). This procedure is done for each of the 10 data sets individually resulting in 10 phase values at sideband (SB) 14 and 5 phase values at SB12 and SB16 phases for argon and each electronic state of CF<sub>4</sub><sup>+</sup>. The lower number of phase values for SB12 and SB16 is a result of specifically optimizing 5 measurements for high/low electron-energy conditions, respectively. The extracted phases of argon are then subtracted from the corresponding CF<sub>4</sub> phases to eliminate the intrinsic attochirp, and converted into time delays using a conversion factor of 215 as. The conversion factor is derived using  $T/2\pi$ , where  $T$  is half the period of the probing IR field. Its value was determined through a cosine fit of the sideband beating in argon, to be  $T=1350.9$  as. Argon was chosen as a reference because of its simple photoelectron spectrum and similar ionization potential to the  $1t_1$  (HOMO) of CF<sub>4</sub>. For the final delay values we take the

#### 4.1. Attosecond Interferometry of Shape Resonances in the Recoil Frame of CF<sub>4</sub>

---

average of all measurements and the error is calculated as

$$\sigma_{\tau} = \frac{\sigma}{\sqrt{n}}, \quad (4.3)$$

where  $\sigma$  is the standard deviation and  $n$  is the total number of data sets used to calculate the mean. The particularly large error bars of sideband 12 in the HOMO and sideband 16 in HOMO-1 are a result of the strong overlap of those sidebands with a more intense main band of the other state, as can be seen in Fig. A17 b.

#### Recoil-frame Angle-resolved PhotoIonization Delays (RAPID)

To resolve photoionization time delays in the recoil frame of CF<sub>4</sub> we extract phases only for specific electron-emission directions with respect to the recoil axis. In all RAPIDs, 9 values for the angle between electron- and CF<sub>3</sub><sup>+</sup>-emission directions were chosen, each with a width of 20°, to get a continuous coverage of the angular space. Additionally the recoil frame was fixed to the XUV polarization to allow for less ambiguity and more direct comparison to theory, where the molecular axis was fixed parallel to the XUV polarization. The accepted angle between CF<sub>3</sub><sup>+</sup> and XUV polarization is 0-25° and 155-180°. All angle resolved CF<sub>4</sub> delays in the RAPID are referenced to the same argon delay using

$$\tau_{\text{ref}}^{\text{SBx}}(\theta) = \tau_{\text{CF}_4}^{\text{SBx}}(\theta) - \tau_{\text{Ar}}^{\text{SBx}}(\beta = 0 - 18^\circ), \quad (4.4)$$

where  $\theta$  is the angle between electron emission and the molecular dissociation axis and  $\beta$  is the angle between electron emission and XUV polarization. SBx is the respective sideband. All delays shown in the manuscript are the referenced values  $\tau_{\text{ref}}^{\text{SBx}}$ .

#### Calculation of the RABBIT delays

The emission-angle-resolved sideband intensity  $I_{\text{SB},n}^{\hat{R}}(E_{\text{SB}}, \vartheta, \varphi; \tau)$  for a single molecular orientation (denoted in what follows by the Euler angle set  $\hat{R} \equiv (\alpha, \beta)$ ) is given by the coherent sum of the two interfering pathways:

#### 4.1. Attosecond Interferometry of Shape Resonances in the Recoil Frame of CF<sub>4</sub>

$$I_{\text{SB},n}^{\hat{R}}(E_{\text{SB}}, \vartheta, \varphi; \tau) = \sum_{\Gamma_0} \left| \hat{M}_{\text{a}}^{\Gamma_0}(E_{<}, \vartheta, \varphi) e^{+i\omega_0\tau} + \hat{M}_{\text{e}}^{\Gamma_0}(E_{>}, \vartheta, \varphi) e^{-i\omega_0\tau} \right|^2, \quad (4.5)$$

where  $\vartheta, \varphi$  denote the set of electron emission angles with respect to the molecular frame (defined in Fig. 4.3), and  $\hat{M}_{\text{a}}^{\Gamma_0}$  and  $\hat{M}_{\text{e}}^{\Gamma_0}$  are the amplitudes of the absorption and emission angles, respectively, whereby the “ $\hat{\phantom{x}}$ ” signifies that these quantities are evaluated for a single molecular orientation  $\hat{R}$ .  $\tau$  is the temporal delay between XUV and IR fields, and  $\omega_0$  is the center frequency of the IR pulse driving the HHG process (here, its value is set to correspond to  $\approx 1.55$  eV, or 800 nm). Further,  $E_{\text{SB}} = n\hbar\omega_0 - I_p$  denotes the energy corresponding to the  $n$ -th sideband, and  $E_{\leq} = E_{\text{SB}} \mp \hbar\omega_0$ . The summation over the irreducible representations  $\Gamma_0$  in Eq. (4.5) reflects the fact that the initially occupied HOMO and HOMO-1 of CF<sub>4</sub> are threefold degenerate (with symmetries  $t_1$  and  $t_2$ , respectively).

Experimentally, the collected signal representing the MF-resolved sideband intensity contains contributions from all orientations of the CF<sub>3</sub><sup>+</sup>-fragment around the recoil axis. To account for this situation, the calculated sideband intensity is isotropically averaged over the azimuthal angle  $\varphi$ :

$$I_{\text{SB},n}^{\hat{R}}(E_{\text{SB}}, \vartheta; \tau) = \sum_{\Gamma_0} \int_0^{2\pi} \left| \hat{M}_{\text{a}}^{\Gamma_0}(E_{<}, \vartheta, \varphi) e^{+i\omega_0\tau} + \hat{M}_{\text{e}}^{\Gamma_0}(E_{>}, \vartheta, \varphi) e^{-i\omega_0\tau} \right|^2 d\varphi. \quad (4.6)$$

In a manner analogous to the experimental data analysis procedure, the angle-resolved sideband delay time is extracted from the calculated sideband (s. Eq. (4.6)) by means of a fit using a harmonic function of the form:

$$I_{\text{SB},n}^{\hat{R}}(E_{\text{SB}}, \vartheta; \tau) = a_0 + a_1 \cos(2\omega_0\tau - \Delta\Phi_{\text{Mol}}(E_{\text{SB}}, \vartheta)). \quad (4.7)$$

The corresponding angle-resolved delay associated with SB  $n$  is then given by  $\tau_{\text{SB}}^n(\vartheta) = \frac{\Delta\Phi_{\text{Mol}}(E_{\text{SB}}, \vartheta)}{2\omega_0}$ . It is this quantity that we refer to as “RABBIT” delay throughout the manuscript. As the expression in Eqs. (4.5) and (4.6) feature an incoherent sum over the contributing

#### 4.1. Attosecond Interferometry of Shape Resonances in the Recoil Frame of CF<sub>4</sub>

---

degenerate orbitals ( $\Gamma_0$ ), it is in general not possible to give a convenient closed-form analytical expression for  $\tau_{\text{SB}}$ . The emission-angle dependent calculated intensity for sidebands 12, 14, and 16 for the RABBIT process involving photoionization from the HOMO resp. HOMO-1 orbital of CF<sub>4</sub> are reproduced in Figs. A1 and A2 in the Appendix A. The black curves indicate the position of the maximizing phase  $\Phi_{\text{Mol}}(E_{\text{SB}}, \vartheta)$  at each angle.

The theoretical molecular-frame-resolved RABBIT delays presented in the main text have been evaluated for a configuration where the laser electric field vector (defining the laboratory frame) points along the dissociating C-F-bond, i.e. for coincident laboratory and molecular frames ( $\alpha = 0, \beta = 0$ ). The partially-averaged delays introduced in Fig. 4.2 have been averaged over all orientations (Euler angles  $\alpha, \beta$ ) using a 50-point Lebedev grid, whereby the integration over the *laboratory-frame* emission angles has been restricted to an emission cone with an opening angle of  $18^\circ$ , as in the experiment.

In principle, the above approach closely follows the formalism introduced in Ref. [43]. There are, however, two distinctions. First, Eq. (4.6) takes into account the degeneracy of the initially occupied orbital, which plays an important role in non-linear molecules. Second, in the current manuscript we adopt the following approximation for the “two-photon” (XUV+IR) matrix elements:  $\hat{M}_{a/e}^{\Gamma_0}(E_{\text{SB}}, \vartheta, \varphi) \approx M_{1h\nu,a/e}^{\Gamma_0}(E_{\text{SB}}, \vartheta, \varphi) T_{\text{cc}}(E_{\text{SB}}, E_{\text{SB}}^{\leq})$ , where  $M_{1h\nu,a/e}$  is the one-photon photoionization matrix element and  $T_{\text{cc}}(E_{\text{SB}}, E_{\text{SB}}^{\leq})$  is the long-range “continuum-continuum” contribution introduced in Ref. [121]. In other words, we ignore the angular momentum couplings in the second step of the XUV+IR-photoionization process. The continuum-continuum matrix element is evaluated using the “P+A’ ” formula (see Eq. (100) and following text) in Ref. [121]. The calculation of the one-photon photoionization matrix elements (in what follows, these will be referred to as “photoionization (PI) matrix elements” for brevity). The procedure for their calculation is outlined in the Appendix A and is identical with the formalism of Ref. [43].

The reference RABBIT delays for Ar are calculated following a con-



#### 4.1. Attosecond Interferometry of Shape Resonances in the Recoil Frame of CF<sub>4</sub>

ceptually analogous procedure, whereby we directly employ the formula for the two-photon matrix elements given in Eq. (24) of Ref. [122]. For completeness, we reproduce this expression below. Note that we have omitted the energy-independent terms and other constant factors, and have slightly adapted the notation in order to ensure consistency with the rest of this text:

$$\begin{aligned}
 M_{a/e}^{m_i}(E_{\text{SB}}^{\lessgtr}, \vartheta, \varphi) = & \\
 & N_{k_{\text{SB}}^{\lessgtr}} N_{k_{\text{SB}}} \frac{1}{|k_{\text{SB}} - k_{\text{SB}}^{\lessgtr}|^2} \exp \left[ -\frac{\pi Z}{2} \left( \frac{1}{k_{\text{SB}}^{\lessgtr}} - \frac{1}{k_{\text{SB}}} \right) \right] \frac{(2k_{\text{SB}}^{\lessgtr})^{iZ/k_{\text{SB}}^{\lessgtr}}}{(2k_{\text{SB}})^{iZ/k_{\text{SB}}}} \\
 & \frac{\Gamma \left[ 2 + iZ(1/k_{\text{SB}}^{\lessgtr} - 1/k_{\text{SB}}) \right]}{(k_{\text{SB}}^{\lessgtr} - k_{\text{SB}})^{iZ(1/k_{\text{SB}}^{\lessgtr} - 1/k_{\text{SB}})}} \sum_{L=l_i, l_i \pm 2} Y_{Lm_i}(\vartheta, \varphi) \\
 & \sum_{\lambda=l_i \pm 1} \langle Y_{Lm_i} | Y_{10} | Y_{\lambda m_i} \rangle \langle Y_{\lambda m_i} | Y_{10} | Y_{l_i m_i} \rangle \\
 & \langle R_{k_{\text{SB}}^{\lessgtr}} | r | R_{n_i l_i} \rangle i^{-\lambda} e^{i\eta_{\lambda}(k_{\text{SB}}^{\lessgtr})}. \tag{4.8}
 \end{aligned}$$

In the above equation,  $k_{\text{SB}}$  and  $k_{\text{SB}}^{\lessgtr}$  correspond to the momenta associated with the energies  $E_{\text{SB}}$  and  $E_{\text{SB}}^{\lessgtr}$ , i.e.  $k_{\text{SB}} = \sqrt{2E_{\text{SB}}}$  and  $k_{\text{SB}}^{\lessgtr} = \sqrt{2E_{\text{SB}}^{\lessgtr}}$ .  $Y_{lm}(\vartheta, \varphi)$  represent spherical harmonics,  $Z = 1$ , and  $\Gamma(x)$  is the complex Gamma function.  $\eta_{\lambda}(k_{\text{SB}}^{\lessgtr})$  denotes the scattering phase shift, and  $\langle R_{k_{\text{SB}}^{\lessgtr}} | r | R_{n_i l_i} \rangle$  corresponds to the radial matrix element for the dipole transition involving the bound-state wavefunction  $R_{n_i l_i}$  (here,  $n_i = 3$  and  $l_i = 1$ ) and the continuum function  $R_{k_{\text{SB}}^{\lessgtr}}$  with asymptotic momentum  $k_{\text{SB}}^{\lessgtr}$ . We extract the one-photon photoionization matrix elements  $\langle Y_{\lambda m_i} | Y_{10} | Y_{l_i m_i} \rangle \langle R_{k_{\text{SB}}^{\lessgtr}} | r | R_{n_i l_i} \rangle i^{-\lambda} e^{i\eta_{\lambda}(k_{\text{SB}}^{\lessgtr})}$  from our ePolyScat calculations [45, 46] (see Appendix A). The associated sideband intensity is calculated from the incoherent sum of the contributions of all three degenerate  $p$ -orbitals ( $m_i = 0, \pm 1$ ). The corresponding reference delays are subsequently extracted from a fit procedure as in the case of CF<sub>4</sub>.

### Acknowledgments

We thank A. Schneider and M. Seiler for their technical support and M. Reiher as well as C.J. Stein for providing the potential-energy surfaces of  $\text{CF}_4^+$ . We gratefully acknowledge funding from the Swiss National Science Foundation (SNSF) through projects 206021\_170775 and 200021\_172946, as well as ERC Project No. 772797. D.B. acknowledges funding from the SNSF through project P400P2\_194343. **Author contributions** S.H. proposed the study, performed the measurements with contributions of X.G., M.H., J-B.J., C.P., and analyzed the data; X.G. designed and built the experimental setup with contributions from S.H.; D.B. developed the theoretical methods and carried out the calculations; H.J.W. supervised the project; S.H., D.B. and H.J.W. wrote the manuscript with input from all coauthors. **Competing Interests** None to declare. **Data and materials availability** All data needed to evaluate the conclusions in the paper are present in the paper or the supplementary materials.

## 4.2 Conclusion and Outlook

In this chapter it was demonstrated, that by combining attosecond spectroscopy with coincidence techniques, it is possible to extract fully angular-resolved photoionization time delays in the molecular frame, even for larger molecules. Further, the information gained in this process, allows fundamental insights into the spatio-temporal photoionization dynamics of molecular resonances.

The generation of RAPIDs, as demonstrated in this chapter, can in principle be used for all molecules that can be aligned in one way or another and have a resolvable electronic spectrum. Considering, that the combination of attosecond and coincidence spectroscopy is a rather new experimental technique [123] and that the number of such experimental setups is steadily growing, the investigation of molecular-frame resolved ionization time delays offers the potential to become an exciting new area of ultrafast spectroscopy.

## Chapter 5

# Attosecond Spectroscopy of Clusters

Since the introduction of attosecond metrology, several studies on different solids have revealed the potential to gain insight into electron dynamics in light-matter interactions [124–127]. In liquids, however, the access to attosecond spectroscopy has remained much more limited, due to the number of experimental challenges involved. A recent measurement of photoionization time delays in liquid water, has revealed delay differences of up to 70 as between liquid- and gas-phase water [32]. The authors could show that the delay difference can be decomposed into a delay that is sensitive to the local environment the electron experiences and a delay caused by non-local mechanisms, such as scattering on neighboring molecules [128]. Although they could show that the contribution of the non-local mechanism to the observed delay difference can be neglected, the physical origin of the delay remains unaccounted for. The reason for this can partly be found in the complexity of the system, which leaves complete quantum scattering calculations out of reach. Hence, a more rigorous investigation of the ionization time-

---

delay difference between liquid- and gas-phase water is desirable. A possible approach can be to study water clusters and thereby bridging the gap between gas- and liquid phase in an almost continuous manner. Doing this requires the detection of electrons and corresponding ions in coincidence, in order to be able to allocate the electrons to the cluster of origin.

In this chapter, attosecond metrology of size-resolved clusters is demonstrated on molecular and atomic clusters. In the journal publication presented in section 5.1, the novel technique of attosecond size-resolved cluster spectroscopy is introduced and the ionization delay differences of small water clusters are investigated. In section 5.2 experimental results of attosecond spectroscopy on argon clusters are presented and section 5.3 concludes the findings.

Details about the publication printed in this chapter are listed below. Text and figures are as in the original publication. Only the style of text, figures and equations has been adapted to match the style used in this thesis. Further the numbering of figures and equations has been changed to match the numbering used throughout the thesis. The same is true for the reference list, which has been included into the reference list at the end of the thesis. The supplementary material, which is part of the original publication, is printed in Appendix B of this thesis.

**Title:** Attosecond spectroscopy of size-resolved water clusters  
**Journal:** *ArXiv* (under review in Nature)  
**URL:** <https://arxiv.org/abs/2106.09459>  
**Published:** 17<sup>th</sup> June 2021  
**License:** Non-exclusive distribution License

## 5.1 Attosecond Spectroscopy of Size-Resolved Water Clusters

X. Gong<sup>1,2,\*</sup>, S. Heck<sup>1,\*</sup>, D. Jelovina<sup>1</sup>, C. Perry<sup>1</sup>, K. Zinchenko<sup>1</sup>, H. J. Wörner<sup>1,†</sup>

<sup>1</sup>Laboratorium für Physikalische Chemie, ETH Zürich, 8093 Zürich, Switzerland

<sup>2</sup>State Key Laboratory of Precision Spectroscopy, East China Normal University, Shanghai, China

\* These authors contributed equally to this work.

† e-mail: hwoerner@ethz.ch

Electron dynamics in water are of fundamental importance for a broad range of phenomena [129–131], but their real-time study faces numerous conceptual and methodological challenges [120, 132, 133]. Here, we introduce attosecond size-resolved cluster spectroscopy and build up a molecular-level understanding of the attosecond electron dynamics in water. We measure the effect that the addition of single water molecules has on the photoionization time delays [100, 134–137] of water clusters. We find a continuous increase of the delay for clusters containing up to 4-5 molecules and little change towards larger clusters. We show that these delays are proportional to the spatial extension of the created electron hole, which first increases with cluster size and then partially localizes through the onset of structural disorder that is characteristic of large clusters and bulk liquid water. These results establish a previously unknown sensitivity of photoionization delays to electron-hole delocalization and reveal a direct link between electronic structure and attosecond photoemission dynamics. Our results offer novel perspectives for studying electron/hole delocalization and its attosecond dynamics.

Electronic dynamics in water play a central role in a broad range of scientific and technological research areas ranging from radiation chemistry to photocatalysis. The dynamics induced by ionization of water are of particular relevance since they initiate the processes underlying radiation damage [130, 131, 138]. The ionization of water is predicted to lead to the formation of a delocalized electron hole, followed by its localization on one water molecule and proton transfer to a neighboring molecule, forming  $\text{H}_3\text{O}^+$  and  $\text{OH}$  [139]. The latter step has been time-resolved only very recently using one-photon extreme-ultraviolet (XUV) photoionization of water clusters [132] and strong-field ionization of liquid water [133]. Both experiments independently determined a 30-50 fs time scale for proton transfer. The formation of the delocalized electron hole, as well as its localization have so far escaped experimental scrutiny because of their sub-femtosecond time scales.

In this work, we access the attosecond time scale of the photoionization dynamics of water on the molecular level by introducing attosecond size-resolved cluster spectroscopy (ASCS). Coupling attosecond interferometry [100, 103, 137, 140] with electron-ion coincidence spectroscopy, we determine photoionization delays for water clusters of increasing size, achieving single-molecule resolution. Photoionization time delays of  $(\text{H}_2\text{O})_n$  are found to continuously increase from  $n = 1$  to  $n = 4 - 5$ . We show that this increase directly reflects the augmenting delocalization of the electron hole created in the ionization process. For these small clusters, we find a linear relationship between the photoionization time delays and the first moment of the electron-hole density created in the ionization process. Beyond  $n = 4 - 5$  the photoionization delays vary little, an effect that we attribute to the partial localization of the electron hole caused by the onset of structural disorder characteristic of larger clusters and bulk liquid water. These assignments are further confirmed by calculations on the O-1s photoionization delays of water clusters, which display these effects even more clearly owing to the

atomic character of the orbitals. As we show below, the present results also confirm the interpretation of photoemission delays from liquid water [120].

Our work thus also reveals a possible experimental access to the spatial delocalization of electronic wave functions, which has always been difficult to characterize. Electron delocalization plays a fundamental role in the properties of solids, where the perfect translational symmetry of single crystals creates fully delocalized electronic wave functions (or Bloch waves), which are disrupted by local disorder in a phenomenon known as Anderson localization [141, 142]. The delocalization of electronic wave functions is also central for understanding the aromaticity of molecules, charge transfer between a metal atom and its ligands, or between a solute and a solvent. The electronic structure of water clusters and liquid water has so far mainly been accessible through quantum-chemical calculations, which have predicted partial (de)localization of the electronic wave functions [143]. Experimental access to this information has however not been reported so far.

Figure 5.1 provides a conceptual overview of our measurements. An XUV attosecond pulse train (APT) generated through high-harmonic generation is focused into a supersonic water-cluster beam, where it is spatio-temporally overlapped with a near-infrared (IR) laser pulse. The APT and IR pulses are phase locked through an actively-stabilized Mach-Zehnder interferometer. The three-dimensional momentum distributions of electrons and ions generated from this interaction are detected in coincidence using COLd Target Recoil Ion Momentum Spectroscopy (COLTRIMS) [65, 144, 145] [see Methods for details]. The photoionization time delays of water clusters are measured by recording photoelectron spectra as a function of the time delay between the overlapping APT and IR pulses, in coincidence with each ionic fragment. As shown in the inset of Fig. 5.1 a, single-photon XUV ionization gives rise to the main bands (MB) in the photoelectron spectra, whereas the additional IR interaction creates sidebands (SB).

## 5.1. Attosecond Spectroscopy of Size-Resolved Water Clusters

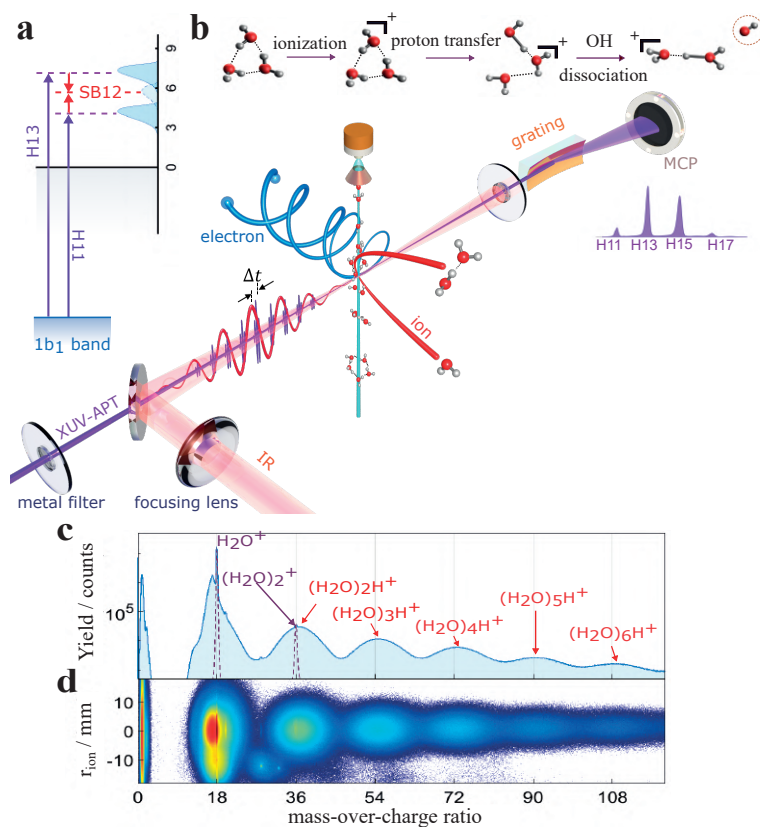


**Figure 5.1: Attosecond size-resolved cluster spectroscopy.** (a), Experimental setup: The charged cluster fragments and emitted photoelectrons are measured in coincidence as a function of the APT-IR delay. The XUV APT is characterized via an online soft-X-ray spectrometer. The inset on the left illustrates ionization by two neighboring harmonic orders and the creation of the sideband spectrum. (b), Dissociative-ionization mechanism of the water trimer, illustrating the only relevant fragmentation pathway for all observed cluster sizes. (c), Mass spectrum of the cluster beam photoionized by an APT as a function of the mass-over-charge (MOC) ratio. (d), Two-dimensional MOC spectrum of water cluster species as a function of position on the ion detector.



The unique assignment of the coincident attosecond photoelectron spectra to a specific cluster size is possible because of a dissociative-ionization mechanism that is general for small ( $< \sim 20$  molecules) water clusters at low ionization energies (Fig. 5.1 b). Following outer-valence single ionization, water clusters undergo rapid proton transfer, followed by the loss of a single OH unit on a sub-picosecond time scale [146–154], such that each detected fragment  $(\text{H}_2\text{O})_n\text{H}^+$  mainly originates from the neutral  $(\text{H}_2\text{O})_{n+1}$  precursor for  $n < 6$  (see Appendix B for details). The observed mass spectrum (Fig. 5.1 c) indeed shows a well-resolved progression of broad peaks that is easily assigned to  $(\text{H}_2\text{O})_n\text{H}^+$  with  $n = 2 - 6$ . The width of the peaks is caused by the kinetic-energy release in the dissociative photoionization, as highlighted in Fig. 5.1 d, which shows the mass spectrum as a function of the detected position radius of the ions on the detector ( $r_{\text{ion}}$ ). The only unprotonated species ( $\text{H}_2\text{O}^+$  and  $(\text{H}_2\text{O})_2^+$ , purple dashed curves) originate from the photoionization of  $\text{H}_2\text{O}$  and  $(\text{H}_2\text{O})_2$ , respectively. The broad distribution peaking at a MOC of 17 is  $\text{OH}^+$  originating from the dissociative ionization of  $\text{H}_2\text{O}^+$ . A fraction of the photoionized dimers remains bound, leading to the sharp  $(\text{H}_2\text{O})_2^+$  peak, and the remainder dissociates to produce  $(\text{H}_2\text{O})\text{H}^+$ . Analogous results have been obtained following the ionization of  $\text{D}_2\text{O}$  clusters. The corresponding mass spectra are shown in Fig. B7.

Figure 5.2 shows the attosecond photoelectron spectra (APS) obtained in coincidence with each cluster size. The APS measured in coincidence with  $\text{H}_2\text{O}^+$  (Fig. 5.2 a) is dominated by the contributions of harmonic orders 11, 13, and 15, and ionization from the two outermost ( $1b_1$  and  $3a_1$ ) molecular orbitals of  $\text{H}_2\text{O}$ . The black line shows a fit using the literature values of the vertical binding energies. The filled spectra correspond to the decomposition of the APS in MB (full colored lines) and SB (dashed lines) spectra. Figures 5.2 b and 5.2 c show the characteristic oscillations with a period of 1.33 fs in the APS coincident with  $\text{H}_2\text{O}^+$  and  $(\text{H}_2\text{O})_2\text{H}^+$ , respectively. The remaining APS are shown in Fig. B3. Analogous results obtained for  $\text{D}_2\text{O}$  clusters are shown in Fig. B8. The SB-intensity os-

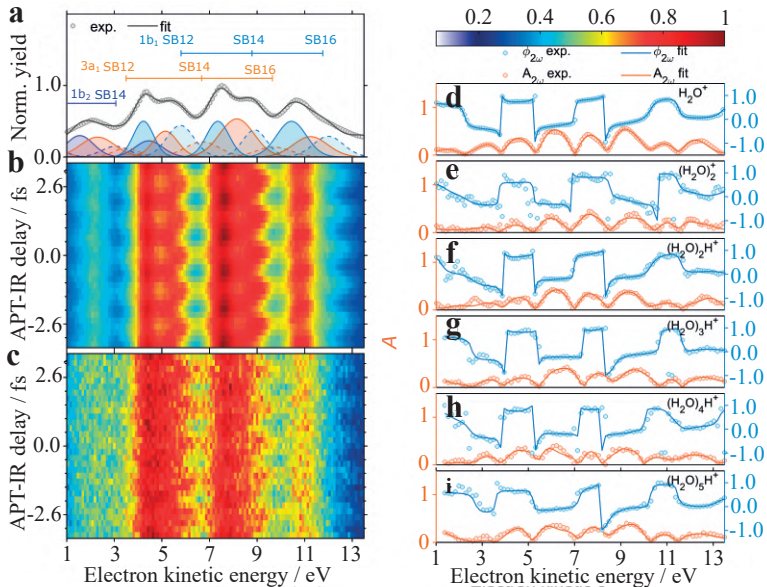


**Figure 5.2: Attosecond photoelectron spectroscopy of size-selected water clusters.** Attosecond photoelectron spectra created by overlapping XUV-APT and IR pulses and detected in coincidence with  $\text{H}_2\text{O}^+$ , integrated over the APT-IR delay (a) and shown as a function of APT-IR delay (b). (c), Same as (b), but detected in coincidence with  $(\text{H}_2\text{O})_2\text{H}^+$ . The false-color map for (b) and (c) is shown in the top right corner. (d) to (i), The Fourier transforms at  $2\omega$  of the attosecond photoelectron spectra detected in coincidence with (d)  $\text{H}_2\text{O}^+$ , (e)  $(\text{H}_2\text{O})_2^+$ , (f)  $(\text{H}_2\text{O})_2\text{H}^+$ , (g)  $(\text{H}_2\text{O})_3\text{H}^+$ , (h)  $(\text{H}_2\text{O})_4\text{H}^+$ , (i)  $(\text{H}_2\text{O})_5\text{H}^+$ , shown in terms of their modulation amplitude ( $A_{2\omega}$ , orange color) and phase ( $\phi_{2\omega}$ , blue color). The experimental data and the fitted curves are shown as open circles and solid lines, respectively.

cillations take the form  $A_q \propto A_{2\omega,q} \cos(2\omega(\tau - \tau_q)) + B_q$ , where  $\omega$  is the angular IR frequency,  $\tau$  is the experimentally varied APT-IR delay,  $\tau_q = \tau_q^{\text{XUV}} + \tau_q^{\text{sys}}$ ,  $\tau_q^{\text{XUV}}$  is the harmonic emission time, and  $\tau_q^{\text{sys}}$  is the system-specific photoemission time delay. Here, we determine relative photoemission delays between water clusters  $(\text{H}_2\text{O})_n$  and  $\text{H}_2\text{O}$ , as a function of  $n$ , which cancels the contribution of  $\tau_q^{\text{XUV}}$ . Because the ionization energies vary by less than 0.6 eV from  $n = 1 - 6$ , the relative measurement also causes negligible contributions of the continuum-continuum (or Coulomb-laser coupling) delays [44, 121] on the order of 4-6 as for SB12-14.

The main challenge in the determination of photoionization time delays from such measurements is the considerable spectral overlap. We therefore use a general procedure, introduced [155] and validated in our recent work [120], that resolves this challenge. Instead of integrating the APS oscillations over specific spectral regions, our approach fully accounts for the spectral overlap. Briefly, we Fourier transform the APS along the time-delay axis and then fit the complex-valued Fourier transform at the  $2\omega$  frequency by assigning a specific phase shift to each spectral component of the MB and SB spectra. Details are given in the Appendix B. We keep the spectral positions and amplitudes fixed to values determined from the delay-integrated spectra (see, e.g., Fig. 5.2 a and B3). The success of this fitting procedure is highlighted by the excellent agreement between the experimental data (circles in Figs. 5.2 d-i) and the fits (full lines). The robustness of the fitting procedure to variations of the initial guesses is shown in Fig. B6.

Figures 5.3 a and 5.3 b show the cluster-size-resolved photoionization time delays corresponding to the  $1b_1$  photoelectron bands from monomer to hexamer, relative to the monomer delay, as determined from SB12 and SB14, respectively. The time delays measured in SB12 (18.6 eV photon energy) increase as a function of the cluster size up to the tetramer, followed by little variation. The results for SB14 show a similar behavior, with indications of a slightly slower convergence as a function of cluster size. The latter results can be

## 5.1. Attosecond Spectroscopy of Size-Resolved Water Clusters

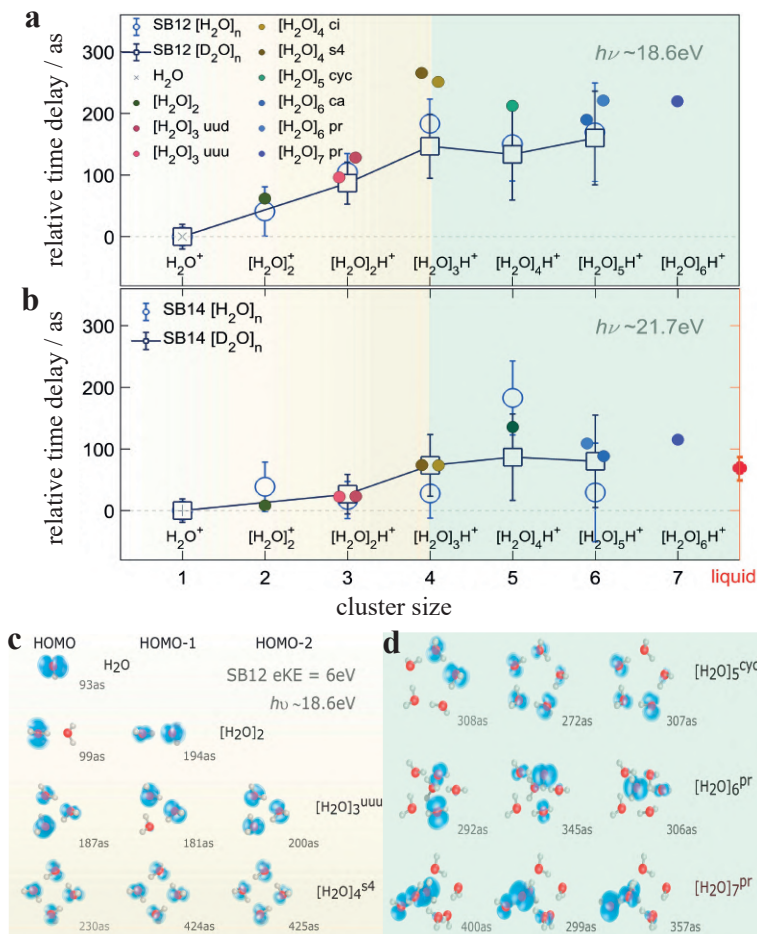


**Figure 5.3: Size-resolved photoionization time delays of water clusters.** (a), Time delays for photoionization out of the  $1b_1$  band of water clusters, relative to  $\text{H}_2\text{O}$  (or  $\text{D}_2\text{O}$ ), measured in SB12 (empty circles). The error represents the combined uncertainty from the timing jitter and standard deviation. The calculated delays (filled symbols) were obtained for a kinetic energy of 6.0 eV. (b), Same as a, but measured for SB14, or calculated with eKE = 9.1 eV, additionally showing the relative photoemission time delay of liquid water reported in Ref. [120]. (c), Electron density map and calculated absolute photoionization delays of the 1-3 highest-occupied orbitals of the  $1b_1$  band of water clusters, highlighting the effect of delocalization (orange shading), followed by partial localization ((d), green shading).

compared to our recent measurements of bulk liquid water, which yielded a photoemission delay of  $69 \pm 20$  as relative to the water monomer for SB14 [120], indicated as the red dot in Fig. 5.3 b. The close agreement between the H<sub>2</sub>O- and D<sub>2</sub>O-cluster results suggest that nuclear-motion effect are not relevant within the accuracy of the present measurements.

To understand the mechanisms governing these delays, we performed *ab-initio* quantum-scattering calculations of the photoionization delays (see Appendix B and Ref. [98] for details). Starting from the trimer, each water cluster exists in several isomeric forms [156–163]. At the low temperatures reached in our supersonic expansion, only one or two isomers are thermally populated, as detailed in Appendix B (Table B1). We used the equilibrium geometries of the most stable cluster isomers reported in Ref. [157] to perform electronic-structure calculations with a correlation-consistent valence-triple-zeta (cc-pVTZ) basis set. These served as an input to the photoionization calculations performed by solving the electron/water-cluster-ion scattering problem at the experimentally relevant scattering energies using the iterative Schwinger variational principle [45, 46]. The input orbitals, scattering potentials and scattering wave functions were all represented by single-center expansions using a typical maximal angular-momentum value of  $\ell = 50$ , whereby numerical convergence with respect to this parameter was ensured. The photoionization time delays, resolved as a function of photoemission direction in the molecular (cluster) frame and the cluster orientation in the laboratory frame, were obtained and subsequently angularly averaged using the partial photoionization cross sections as weighting factors (for details, see Appendix B). These calculations yielded angular-integrated one-photon-ionization (or Wigner) delays. We have compared these delays to two-photon (XUV+IR or RABBIT) delays obtained by additionally including the effect of the IR field on the photoionization delays. The results, shown in Figs. B9-B13, establish the close correspondence of the one- and two-photon delays in the case of water clusters, both angle-resolved and angle-integrated, and therefore support our compar-

ison of the angle-averaged one-photon delays with the observables of the present experiment. Using this methodology, photoionization delays were obtained for each of the  $n$  orbitals of  $(\text{H}_2\text{O})_n$  that contribute to the  $1b_1$  band of each water cluster. The cross-section-weighted average of these delays (defined in Eq.(1) in the Methods section) are shown as the large filled symbols. The agreement between theory and experiment is excellent (Figs. 5.3 a and 5.3 b).

Figures 5.3 c and 5.3 d show the densities of the highest-occupied molecular orbitals of the  $1b_1$  band of the most stable isomer of each cluster size, together with their absolute photoionization delays. Figure 5.3 c suggests that the increasing orbital delocalization correlates with the increasing time delay. The HOMO of the dimer has almost the same time delay as the monomer, whereas the delocalization of the HOMO-1 in the dimer leads to an increase of the time delay by nearly 100 as. This comparison also shows the very small effect ( $\sim 6$  as) of electron scattering on the neutral  $\text{H}_2\text{O}$  neighbor in the dimer. Among the trimer orbitals, it is also the most delocalized orbital (HOMO-2) which has the largest photoionization delay (200 as). The tetramer orbitals are perfectly delocalized over all molecules, owing to the  $S_4$  symmetry of its most stable isomer, which leads to the largest photoionization delays (up to 425 as) found in our calculations.

Interestingly, a further increase of the cluster size does not increase the delays further. The reason is obvious from Fig. 5.3 d. Most larger clusters than the tetramer have a lower symmetry, many of them having no symmetry elements at all. This leads to a localization of the orbital densities on a small number of typically 2-3 neighboring molecules. This effect is reflected as a stagnation of the associated photoionization delays around values of  $\sim 300$  as in SB12. This observation suggests that the disorder-induced orbital localization in the larger clusters causes the experimentally observed saturation of the measured photoionization delays at the largest cluster sizes measured in this work.

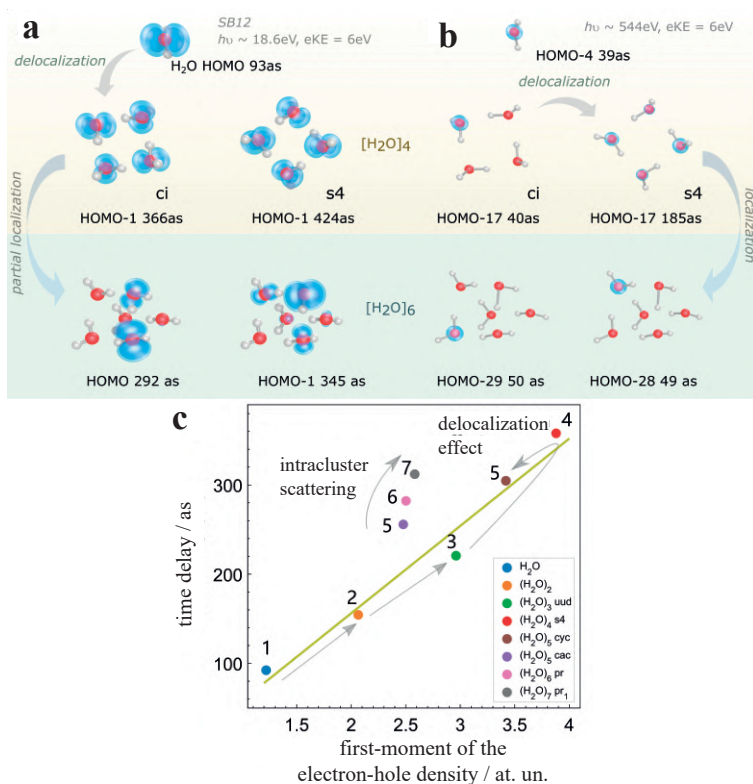


**Figure 5.4: Effect of orbital delocalization on photoionization delays of water clusters (a),** Photoionization delays for the  $1b_1$  band of water clusters for a kinetic energy of  $eKE = 6.0$  eV, corresponding to the experimental measurements in SB12. **(b),** Same as (a), but for the  $O1s$ -band of water clusters using the same kinetic energy, and a correspondingly adjusted photon energy. **(c),** Correlation between the photoionization time delays and the first moment of the electron-hole density of the  $1b_1$  band of water clusters ( $eKE = 6.0$  eV).

To further verify this surprisingly simple relation between time delays and orbital localization, we performed additional calculations on the oxygen-1s orbitals of the water clusters, with complete results shown in Appendix B (Figs. B14-B19). The O1s-orbitals have the advantage of remaining essentially atomic in character and not being significantly modified by hydrogen bonding and orbital hybridization. For this reason, they allow us to isolate the effect of orbital (de)localization even more clearly. The results obtained for the O1s-band are shown in Fig. 5.4 b, where they are compared to the results for the  $1b_1$  band (Fig. 5.4 a). This comparison further supports our interpretation. The photoionization delay remains essentially unchanged from the monomer (39 as) to the tetramer ci (40 as), where the O-1s orbital is fully localized, but increases to 185 as in the tetramer s4, where the O-1s orbital is fully delocalized as a consequence of the high symmetry. Increasing the cluster size further results in a complete localization of the O-1s orbital, which leads to a remarkable decrease of the photoemission delay to 49-50 as in the hexamer. The photoionization delays of the O1s orbitals in the hexamer being practically identical with the monomer (39 as) highlights, both, the direct link between photoionization delay and orbital delocalization and the very small effect (a few attoseconds) of electron scattering on the neutral  $H_2O$  moieties of the clusters.

Finally, we establish a quantitative link between time delays and electron-hole delocalization. Figure 5.4 c shows a correlation plot between photoionization delays of the  $1b_1$  band of the water clusters  $(H_2O)_n$  and the first moment of the electron-hole density in the  $1b_1$  band of the singly-ionized clusters  $(H_2O)_n^+$  (defined in Eqs. (2)-(3) in Methods). The most stable isomers of all clusters from  $n = 1$  to  $n = 5$  display a nearly perfect linear relationship between the two quantities, as indicated by the straight line in Fig. 5.4 c (correlation coefficient  $\rho = 0.984$ ). This representation also highlights the continuous increase of the delocalization from  $n = 1$  to  $n = 4$ , followed by partial localization at  $n = 5 - 7$ , visible in the fact that the second-most stable isomer of  $n = 5$  and the most stable isomers of  $n = 6$  and 7 have nearly the same first moment of the electron-hole



density. Interestingly, the delays of the latter three isomers display a continuous, yet very small increase, which we assign to intracuster scattering, quantifying this effect as well.

These results have a range of interesting implications. First, they demonstrate the sensitivity of photoionization delays to orbital delocalization in water clusters, which, to our knowledge, has not been experimentally accessible in any form of matter so far. Second, they reveal the mechanism that is responsible for orbital localization in liquid water on the molecular level, i.e. the onset of structural disorder. This effect is reminiscent of Anderson localization in solids [141]. Whereas perfect crystals with translational symmetry have fully delocalized bands, the presence of defects causes their localization, which has a multitude of interesting consequences in solid-state physics. The orbital localization in liquid water can thus be viewed as a consequence of its structural disorder.

We have introduced a new technique, ASCS, and have applied it to measure photoionization time delays of size-resolved water clusters. This study has revealed an unexpectedly simple relationship between orbital localization and time delays, establishing an experimental pathway to probing electron-hole localization in complex matter. Looking forward, our methods can be used to temporally resolve both local and non-local electronic relaxation dynamics in size-resolved water clusters, such as Auger decay, intermolecular Coulombic decay [164, 165] and electron-transfer-mediated decay [166]. More generally, they will facilitate a molecular-level understanding of attosecond electron dynamics in the liquid phase, with implications for the elementary processes underlying chemical reactivity and biological function.

### Methods

#### Laser Setup and Attosecond-Pulse Generation

The experimental setup is based on a regeneratively amplified Titanium-Sapphire laser system which delivers near-infrared (IR) femtosecond laser pulses with 1.2 mJ energy at 5 kHz repetition rate, a central wavelength of 800 nm and 36 fs pulse duration (full-width at half-maximum in intensity). This laser beam is split with a 70:30 beam splitter and the more intense part is focused into a 3 mm long, xenon-filled gas cell to generate an extreme-ultraviolet attosecond pulse train (XUV-APT) via high-harmonic generation. A coaxial 100-nm aluminum foil on a quartz ring is placed before a nickel-coated toroidal mirror ( $f = 50$  cm) to spectrally filter the XUV spectrum and eliminate the residual IR pulse co-propagating with the XUV beam. The XUV spectrum was characterized with a home-built XUV spectrometer consisting of a 100-nm aluminum film, an aberration-corrected flat-field grating (Shimadzu 1200 lines/mm) and a micro-channel-plate (MCP) detector coupled to a phosphor screen. The XUV-APT is recombined with the remaining part of the IR beam after the toroidal mirror via a perforated silver mirror to constitute a Mach-Zehnder interferometer. The path length difference, i.e. the time delay between the overlapping XUV-APT and IR pulses is controlled via a high-precision direct-current motor (PI, resolution 0.1  $\mu\text{m}$ ) and a piezoelectric motor (PI, resolution 0.1 nm), constituting a combined delay stage operating on femtosecond and attosecond time scales, respectively.

#### Coincidence Spectrometer

The phase-locked XUV-APT and IR pulses are collinearly focused into the supersonic gas jet in a COLTRIMS (COLd Target Recoil Ion Momentum Spectroscopy) [65, 144, 145] spectrometer. The electrons and ions created by XUV photoionization are guided by a weak homogeneous electric field ( $3.20 \text{ V}\cdot\text{cm}^{-1}$ ) and a homogeneous magnetic field (6.70 G) towards two time- and position-sensitive detec-

tors at opposite ends of the spectrometer. The detectors consist of two MCPs (Photonis) in Chevron configuration, followed by a three-layer delay-line anode (HEX) with a crossing angle of 60 degrees between adjacent layers and an active radius of 40 mm manufactured by RoentDek. For the electrons, the length of the extraction region is 7 cm, followed by a 14 cm field-free region. A homogeneous magnetic field is applied over all regions by a set of Helmholtz coils, which are tilted to counteract the earth's magnetic field. The COLTRIMS gives access to the typical electron-ion coincidence measurement with full three-dimensional momentum resolution in  $4\pi$  solid angle. The momentum resolution of electrons is  $\Delta p_x = \Delta p_y = 0.001$  a.u. and  $\Delta p_z = 0.056$  a.u., where  $x$  corresponds to the direction of light propagation,  $y$  is the direction of the supersonic gas jet and  $z$  is the time-of-flight direction. The photoelectron kinetic energy is calibrated via the XUV-APT photoelectron spectrum of argon with an ionization potential of  $I_p \sim 15.8$  eV.

### Cluster source

The neutral water clusters [167, 168] are formed in a continuous supersonic expansion into vacuum with a water vapor pressure of 0.3 MPa through a 50  $\mu\text{m}$  nozzle orifice and pass through two conical skimmers (Beam Dynamics) located 10 mm and 30 mm downstream with a diameter of 200  $\mu\text{m}$  and 1 mm, respectively. The liquid water is maintained at 408 K to give rise to a sufficient vapor pressure in a container of 0.7 L to support a stable water-cluster beam for a duration of 120 hours. The water-cluster source is coupled to the COLTRIMS via two differential pumping stages. To maintain the ultrahigh vacuum in the main reaction chamber, a differentially pumped beam dump captures the molecular beam after the interaction region.

### Definition of the calculated quantities

The calculation of the orbital-specific photoionization delays is described in the main text and in more detail in Appendix B. Here, we additionally define the cross-section-averaged delays shown in Figs. 5.3 a, 5.3 b as large empty circles and also in Fig. 5.4 c. Since the contributions of individual orbitals to the  $1b_1$  band of the water clusters cannot be resolved, we introduce the cross-section-average of the time delays over the  $n$  orbitals constituting the  $1b_1$  band of  $(\text{H}_2\text{O})_n$  as follows:

$$\tau(E) = \frac{\sum_{i=1}^n \sigma_i(E) \tau_i(E)}{\sum_{i=1}^n \sigma_i(E)}, \quad (5.1)$$

where  $\sigma_i(E)$  is the photoionization cross section of orbital  $i$  of the  $1b_1$  band at the photon energy  $E$  and  $\tau_i(E)$  is the corresponding photoionization time delay.

In Fig. 5.4 c, we additionally show the first moment of the electron-hole density, calculated using ORBKIT package [169]. In the case of a single orbital (with index  $i$ ) this is defined as

$$\mathcal{M}_i = \frac{\int \rho_i(\vec{r} - \vec{r}_i) |\vec{r} - \vec{r}_i| d^3r}{\int \rho_i(\vec{r}) d^3r}, \quad (5.2)$$

where  $\rho_i(\vec{r})$  is the density of orbital  $i$  and  $\vec{r}_i$  is its center of charge. In analogy to the time delays, we also define a cross-section average of the orbital delocalization as

$$\mathcal{M} = \frac{\sum_{i=1}^n \sigma_i \mathcal{M}_i}{\sum_{i=1}^n \sigma_i}, \quad (5.3)$$

## Addendum

**Acknowledgment** We thank A. Schneider and M. Seiler for their technical support. **Funding** We gratefully acknowledge funding from an ERC Consolidator Grant (Project No. 772797-ATTOLIQ), and project 200021\_172946 as well as the NCCR-MUST, funding instruments of the Swiss National Science Foundation. D. J. thanks the European Union's Horizon 2020 programme (FP-RESOMUS - MSCA 801459) program for a fellowship and A. Schild for introduction to ORBKIT. The results have been obtained on the ETH Zürich Euler cluster and the NCCR-Cluster supercomputer.

**Author contributions** X.G. and S.H. carried out the experiments and analysed the experimental data. X.G. constructed the experimental apparatus with contributions from S.H., K.Z. and C.P. D.J. and H.J.W. performed the theoretical calculations. X.G., S.H., and H.J.W. wrote the initial manuscript. All authors discussed and reviewed the manuscript.

**Competing Interests** The authors declare no competing interests.

**Supplementary information** is available for this paper.

**Correspondence and requests for materials** should be addressed to H.J.W.

**Data availability statement** All data is available from the corresponding author on request.

## 5.2 Argon Clusters

To see if the observed increase of ionization time delay in the water clusters also applies other systems, a similar experiment as described in the previous section was performed on argon clusters. The bonding between argon atoms inside a cluster is much weaker compared to the molecules in a water cluster. This is due to the weak

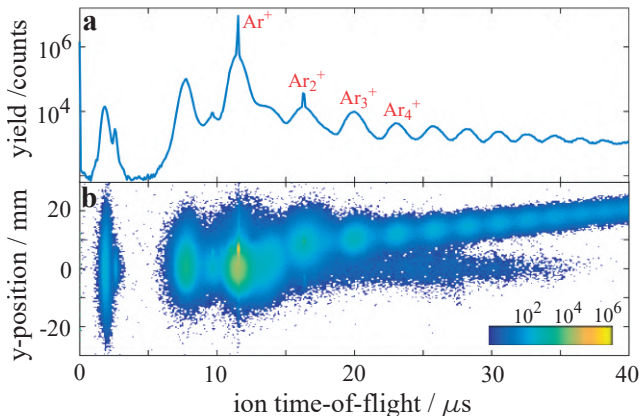


**Figure 5.5:** (a) Time-of-flight spectrum of the ions with the yield on a logarithmic scale. The position of  $\text{Ar}^+$  and several clusters are marked in red. (b) Same as in (a), but with the y-position on the detector on the y-axis and the yield represented by a logarithmic false color scale. The y-direction in the laboratory frame, corresponds to the propagation direction of the gas jet. Note that the peaks at 2  $\mu\text{s}$  and 7.7  $\mu\text{s}$  are by  $\text{H}^+$  and  $\text{OH}^+$ , due to remains of water in the vacuum chamber.

interaction between the atoms, which is solely based on the van der Waals force [170]. This circumstance also leads to relatively large internuclear distances in the clusters (e.g.  $R_{\text{Ar}_2} = R_{\text{Ar}_3} = 3.8 \text{ \AA}$ ).

This changes for the charged argon clusters, which have a much stronger bond owing to charge-induced dipole interaction [170]. Therefore, the charged clusters also have shorter equilibrium internuclear distances than their neutral counterparts. Upon vertical ionization the ionic cluster configuration is far from its equilibrium and, hence, have a lot of potential energy, which leads to a myriad of fragmentation [171]. The variety of fragmentation pathways makes it impossible to assign ionic cluster fragments to a specific cluster size at time of ionization. Respectively, the interpretation of extracted ionization delays presents a rather ambiguous task.

The argon cluster were generated by supersonic expansion of argon into the vacuum chamber with a backing pressure of 1 bar. The cluster yield can be seen in Figure 5.5 a, where the ion yield is plotted as a function of time-of-flight. The peaks caused by counts of  $\text{Ar}^+$ ,  $\text{Ar}_2^+$  and larger clusters are indicated in the figure. For  $\text{Ar}^+$  and  $\text{Ar}_2^+$ , a combination of a narrow peak and a broad distribution can be observed, while for  $\text{Ar}_3^+$ ,  $\text{Ar}_4^+$  and larger clusters there is only a broad distribution. A broad distribution in the time-of-flight implies that the ions have kinetic energy upon ionization and therefore serves as an indication for fragmentation. The narrow peaks in  $\text{Ar}^+$  and  $\text{Ar}_2^+$  are caused from ions which did not undergo a fragmentation process and the broad distributions surrounding it are the fragmented ions with kinetic energy. In Fig. 5.5 b, the same is shown with the addition of the detector position of the ions in y-direction. In this way, one can clearly differentiate between ions originating from the gas jet or the background, because the propagation of the gas jet is along the y-direction. Atoms, that are ionized in the gas jet, have a constant momentum in y-direction, which causes an offset on the detector, linear to the ions time-of-flight.

Argon has a simple energy spectrum, with ionization only from the 3p orbital for harmonics up to order 17. The corresponding ionization potentials for  $3p_{3/2}$  and  $3p_{1/2}$  are 15.7 eV and 15.9 eV [172]. In Figure 5.6 a the RABBIT spectrogram for  $\text{Ar}^+$  is shown, which only contains a single band, because the spin-orbit splitting can not be resolved. 5.6 b and 5.6 c contain the RABBIT spectrograms for  $\text{Ar}_2^+$  and the fragmented ( $\text{Ar}_4^+$ )<sub>frag</sub> respectively. The sideband oscillations can clearly be observed in all three cases. To extract the ionization time delays from those RABBIT spectra, the sideband intensity is fitted with equation (2.30), as detailed in chapter 2.3.

To compare the ionization delays of argon monomer with argon clusters, delays are extracted from RABBIT spectrograms comprising electrons that were recorded in coincidence with several of the detected charged cluster fragments. The delay differences between argon clusters and monomer, from a multitude of data sets, are

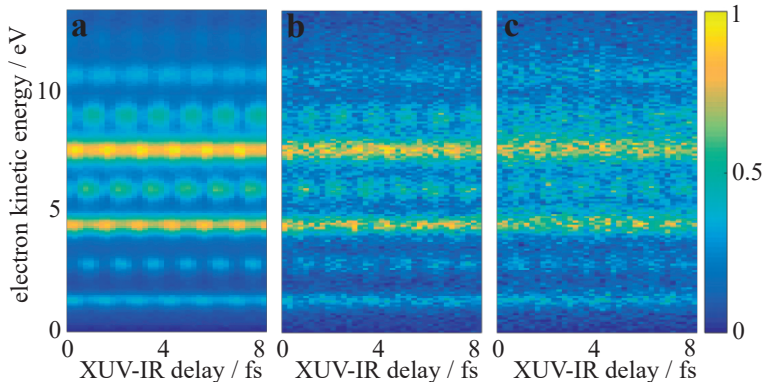


**Figure 5.6:** RABBIT spectrograms for electrons in coincidence with (a)  $\text{Ar}^+$ , (b)  $\text{Ar}_2^+$  and (c)  $(\text{Ar}_4^+)_{\text{frag}}$ , from a single experimental data set. Counts are normalized and shown in false color. The sidebands 12 and 14 are at 2.8 eV and 5.9 eV respectively.

shown in Figure 5.7, where gray stars represent the delays of individual data sets, and blue circles give the mean of all data sets with the standard deviation given as error bars. Fig. 5.7 a-c give the delay differences for sideband 12-16. It can be seen that any measured delays between clusters and monomer are only small and even zero within the error bars. Merely for sideband 12 (Fig. 5.7 a) there seems to be a measurable delay difference converging to  $\sim 25$  as for larger clusters. Similar to the results presented in the beginning of this chapter in Fig. 5.3, the delays are expected to be largest for the lowest sideband (SB12 in this case), which is a consequence of the energy-dependent scattering phase shift as illustrated in Fig. 2.1. The observed delay difference between argon monomer and clusters at sideband 12 could well be a sign of the delocalization in rare gas clusters affecting the photo ionization dynamics, similar to the observation in water clusters. However, due to the indistinct fragmentation dynamics of neutral argon clusters only an average of various cluster sizes is measured. Nevertheless, there is some relation between the measured ionic cluster fragments and the corresponding neutral mother clusters:  $(\text{Ar}_2^+)_{\text{frag}}$  originates mainly from



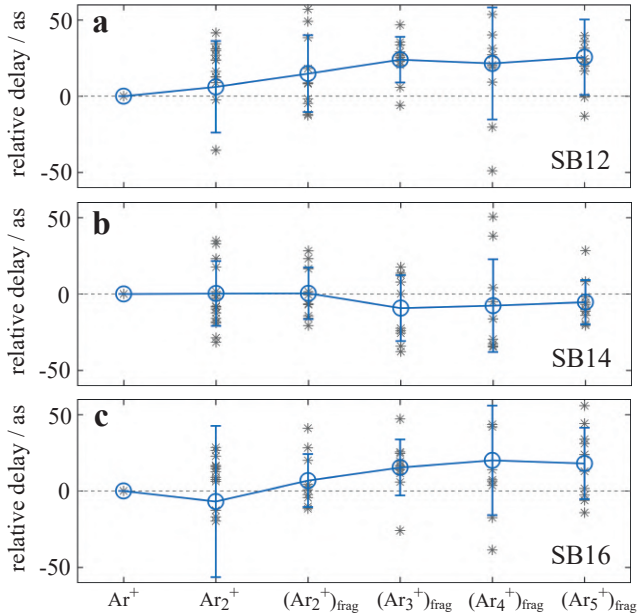


**Figure 5.7:** Relative ionization delays of argon clusters, referenced to argon monomer (e.g.  $\tau(Ar_n) - \tau(Ar)$ ) for (a) SB12, (b) SB14 and (c) SB16. Gray stars show the relative delays obtained from individual measurements and blue circles represent the mean of all measurements. The error bars give the standard deviation of the mean from the individual results. The subscript 'frag' in the x-axis label indicates that the ions are fragmented parts from a larger cluster of unknown size.

## 5.2. Argon Clusters

Cluster size n for $\text{Ar}_n$	Point group of most symmetric configuration [173]	number of symmetry elements h
3	$C_3$	3
4	$T_d$	24
5	$D_{3h}$	12
6	O	24
7	$D_{5h}$	20
8	$T_d$	24
9	$C_3$	3
10	$T_d$	24
14	$O_h$	48
19	O	24
20	$T_d$	24

**Table 5.1:** Point group and number of symmetry elements h for various cluster sizes  $\text{Ar}_n$ .

neutral clusters  $\text{Ar}_n$ , with  $n=3-10$ , whereas for  $(\text{Ar}_3^+)_{\text{frag}}$  and larger fragments the original cluster size is mainly  $\text{Ar}_n$ , with  $n>10$  [171]. Observing the significant delay differences in sideband 12 only from  $(\text{Ar}_3^+)_{\text{frag}}$  on and larger clusters, it follows that the difference in photoionization time delay of argon clusters compared to the monomer is largest for clusters consisting of more than 10 atoms.

This seems different to the finding in water clusters where no further increase in ionization delay was found beyond the tetramer  $((\text{H}_2\text{O})_4)$ . But rare gas clusters exhibit much higher symmetry than water clusters, with even clusters larger than 10 atoms having multiple symmetry elements. The point groups and symmetry elements for argon clusters up to  $n=20$  are listed in table 5.2, from which it can be seen that clusters larger than 10 atoms are among the most symmetric ones. Hence, the observation of the largest ionization time delays for argon clusters consisting of more than 10 atoms, indicates that orbital delocalization in rare gas clusters indeed has an impact on photoionization delays.

## 5.3 Conclusion and Outlook

In conclusion we have demonstrated the feasibility of cluster-size resolved attosecond metrology on the example of molecular and atomic clusters. In water clusters we found an increase in photoionization time delays for increasing cluster size, relative to a single water molecule. This increase in ionization delay is correlated with the orbital delocalization and hence the total symmetry of the cluster. In water clusters the first-moment of the electron-hole density, which serves as a measure for the degree of delocalization, increases up to the tetramer, which has the most symmetric isomer with  $s_4$  point group. For a further increase in cluster size, partial localization sets in due to decrease in symmetry, causing the ionization delays to converge to a constant value close to the delays found in liquid water [32]. A possible exception to this is the octamer, which also has  $s_4$  symmetry but neither experimental nor theoretical results were available at the time of writing.

In argon clusters, the ionization-delay differences between clusters and the single atom are generally smaller than in water, with the largest delays found for clusters consisting of more than 10 atoms. In contrast to water clusters, rare gas clusters are highly symmetric, even for large systems ( $> 10$  atoms), with the highest symmetry found in a cluster consisting of 14 atoms. Even though the ionization delays in argon clusters allow only very restricted interpretation, due to the ambiguous fragmentation pathways, the results constitute a further indication of how photoionization dynamics are affected by symmetry and orbital delocalization.

The results presented in this chapter thereby set the foundation for further work on cluster-size resolved attosecond spectroscopy and the investigation of orbital delocalization and its effect on ionization and electron dynamics.



## Chapter 6

# Attosecond Spectroscopy of Rare Gas Dimers

Two-center interference is one of the most prominent effects in quantum mechanics. The first double-slit experiment has been carried out by Thomas Young in 1801 with light [174]. It then took until 1960 - long after the wave nature of particles became known - until the double-slit experiment was demonstrated with electrons [175]. Shortly after that, it was noted by Cohen and Fano, that the electron wave from the photoionization of a diatomic homonuclear molecule, is similar to the one behind a double slit [176]. Since then, there have been numerous investigations on two-center interference in diatomic homonuclear molecules [177–186]. So far, the majority of the studies were looking at the effects on partial and total cross-sections of ionization, where oscillations in the cross-section as a function of electron energy were found [177, 179, 180, 182, 184, 186], even for unaligned molecules [176, 187]. More recently, the signature of the two-center interference has been found in the yield of high-harmonic generation from  $\text{CO}_2$  [178, 188–191] and  $\text{H}_2$  [181, 192]. From chapter 2.1 it is known that a variation in cross-section is often

---

associated with a change of the Wigner time delay and therefore one can expect that the effect of two-center interference might be observable in the photoionization time delays of diatomic molecules. Indeed, strong variations of the Wigner delay as a result of two-center interference in diatomic molecules have been predicted theoretically [193–195], but - to the best of my knowledge - not yet experimentally observed. Which electron energies are most affected by the interference strongly depends on the internuclear distance of the diatomic molecule, i.e. the slit distance. For larger internuclear distances, also electrons with a longer de Broglie wavelength and smaller kinetic energy are affected. Ning et al. predicted a sharp increase in the ionization delay of  $\text{H}_2^+$  at 105 eV and 340 eV at an internuclear distance of 1.587 Å [195]; they further showed the position of the peaks decrease in energy with increasing nuclear distance. This was confirmed by Liao et al., who calculated the molecular-frame-resolved Wigner delay for a heterogeneous diatomic molecule with an internuclear distance of 2.116 Å and found pronounced peaks in the stereo time-delay difference from an electron emitted to the left or right around 55 eV and 195 eV [194].

Because for diatomic molecules with internuclear distances around 1-3 Å (as it is common), a measurable effect of the two-center interference is only expected for high electron energies ( $> 50$  eV), it is experimentally challenging to investigate. A solution to this, can be to increase the internuclear distances, by studying atomic rare-gas dimers, which have much larger atomic separation (3-5 Å) due to the nature of their van der Waals interactions, keeping them weakly bound.

A further advantage of rare-gas dimers is the possibility to compare time delays to the monomer, which have very similar ionization potentials. This minimizes the influence of other sources of changing ionization delays, such as laser-induced delays [196]. The effects of the two-center interference on the ionization delays, can thus be more easily and clearly identified.

In section 6.1, the energy-dependent photoionization time delay dif-

---

ferences in monomer and dimer of neon, argon and krypton are investigated. Section 6.2 studies the ionization delays in the molecular frame of neon and section 6.3 concludes this chapter.





## 6.1 Two-Center Interference in Dimers

### Introduction

The molecular double slit can be described by the superposition of two spherical waves

$$\Psi_{1,2} = \frac{1}{|r|} \cdot e^{i(k(r \pm R/2) + \Phi_{1,2})} \quad (6.1)$$

departing at the two atoms with internuclear distance  $R$ , momentum  $k$  and initial phase  $\Phi$  [197]. The electron wavepacket can only be described by two departing waves from the two atoms if the electron hole is delocalized between the atoms. In this case interference between the two wavepackets analogous to the double slit interference takes place. In Figure 6.1 the orbital diagram is shown for the neon dimer for the four highest occupied orbitals, which are formed from the 2p orbitals of each neon atom. The orbital diagram is schematically identical for the argon and krypton dimers. From the three-dimensional wavefunctions in Fig. 6.1 it can be seen that each orbital is fully delocalized over both atoms, but the coherent superposition of two orbitals with different parity (e.g. g and u) will lead to localization of the wavefunction on one atom. The effect of the delocalization and localization of the wavefunction and its role in the two-center interference has been demonstrated by M. Kunitski et al. [197] in the year 2019. In a strong-field ionization experiment of neon dimers they were able to isolate the symmetry of the remaining ion and thereby observe both gerade and ungerade type of interference. The superposition of both causes the interference pattern to vanish.

### Experiment

As discussed in chapter 5.2, the bonding between the two atoms in a rare gas dimer is only due to weak van der Waals interaction and therefore the internuclear distances are particularly large:

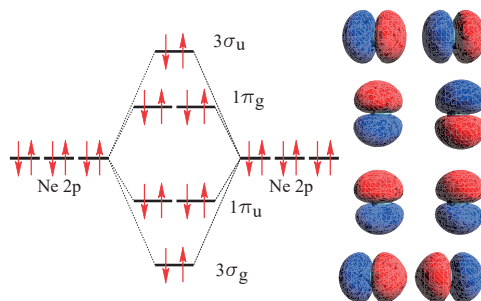


**Figure 6.1:** Highest-occupied molecular orbitals of the neon dimer, formed from the 2p orbitals of each neon atom. On the right side, the three-dimensional orbital wavefunctions are shown for the respective orbitals. The wavefunctions were calculated using ORCA [198, 199].

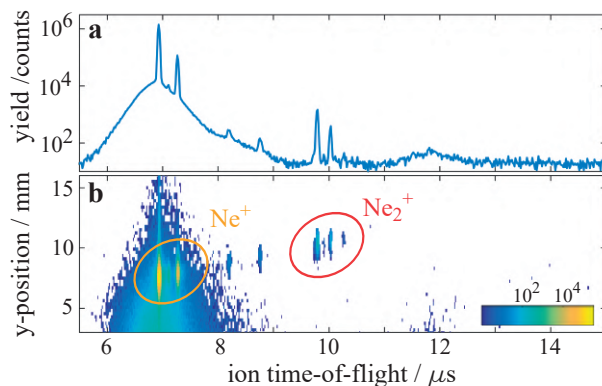


**Figure 6.2:** (a) Time-of-flight spectrum of the ions from a neon gas jet with the yield on a logarithmic scale. (b) Same as in (a), but with the y-position on the detector on the y-axis and the yield represented by a logarithmic false color scale. The y-direction in the laboratory frame, corresponds to the propagation direction of the gas jet. Note that the isotopic distribution of neon is  $^{20}\text{Ne}$ : 90.48%,  $^{21}\text{Ne}$ : 0.27% and  $^{22}\text{Ne}$ : 9.25% and all isotopes are observed.

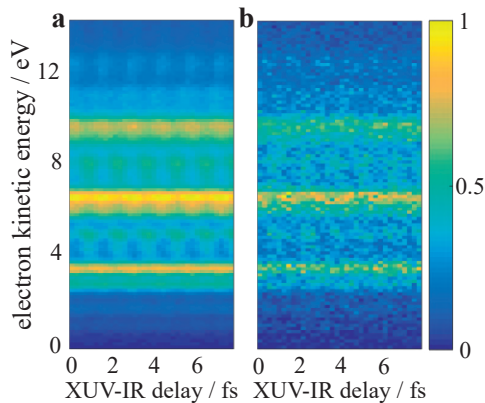


**Figure 6.3:** RABBIT spectrograms for electrons in coincidence with (a)  $\text{Kr}^+$  and (b)  $\text{Kr}_2^+$ , from a single experimental data set. The electron emission angle is  $\theta_{\text{Lab}} = 0 - 25^\circ$ , where  $\theta_{\text{Lab}}$  represents the polar angle in the laboratory frame. Counts are normalized and shown in false color. The sidebands 12 and 14 are at 4.5 eV and 7.6 eV, respectively.

$R_{\text{Ne-Ne}}=3.337 \text{ \AA}$  [200],  $R_{\text{Ar-Ar}}=3.8 \text{ \AA}$  [201] and  $R_{\text{Kr-Kr}}=4.01 \text{ \AA}$  [202]. This makes them well suited to study the effects of two-center interference, but it also makes the experimental preparation of the dimers inefficient. The clusters are generated by supersonic expansion of the rare gas through a  $50 \mu\text{m}$  nozzle (see 3.3.2), with a backing pressure of 3 bar for neon, 1 bar for argon and 0.5 bar for krypton. Under these conditions the relative yield of undissociated dimers was between 0.05-0.1% for  $\text{Ne}_2$  and 0.5-1% for  $\text{Ar}_2$  and  $\text{Kr}_2$ . The yield of all ions is shown in Fig. 6.2, Fig. 5.5 and Fig. C1 for neon, argon and krypton, respectively. In the top panel of those figures, the total yield as a function of ion time-of-flight is shown in counts and the bottom panel shows additionally the y-position on the detector. It can be seen that the yield of larger clusters is very different for the three rare gases. In neon there are no larger clusters observed, while in krypton there are some  $\text{Kr}_2^+$  and  $\text{Kr}_3^+$  fragments from larger clusters detected and the time-of-flight spectrum of argon shows ions up to  $\text{Ar}_{10}^+$  and larger.

To study the effect of the two-center interference on the ionization time delays, a RABBIT experiment is performed (see chapter 3.4.2) with electrons measured in coincidence with the ions. The RABBIT spectrograms are then analyzed for the un-fragmented monomer (i.e. with zero kinetic-energy release) and dimer separately. By only considering electrons from the un-fragmented ions, contributions from other clusters are excluded. The RABBIT spectrograms for monomer and dimer are shown in Fig. C2, Fig. 5.6 and Fig. 6.3 for neon, argon and krypton, respectively. In the RABBIT spectrograms it can be seen that only the HOMO state of each gas is ionized, leading to a simple electronic spectrum with isolated main and sidebands. The ionization potentials of the monomer are  $IP_{\text{Ne}}=21.6$  eV [172],  $IP_{\text{Ar}}=15.7$  eV [172] and  $IP_{\text{Kr}}=14.1$  eV [172] with the IP of the dimers being only slightly lower [203–205]. The RABBIT spectrograms of argon and krypton were analyzed by fitting a cosine to the sideband intensity according to equation (2.30). For neon the complex-fit analysis, described in chapter 3.4.2, was used because the high IR intensity of the probe<sup>1</sup> causes some contribution of  $4\omega$  as can be seen in Fig. 6.8.

For each gas sample there were multiple experiments performed using different harmonic spectra, yielding several data sets with a different range of sidebands available. Each data set was analyzed separately and in the remaining chapter the ionization delays discussed are the mean values of all individual data sets and error bars show the standard deviation. There are 3, 13 and 6 data sets available for Ne, Ar and Kr respectively.

## Results

In Figure 6.4 the relative ionization delays between dimer and monomer  $\tau_{\text{rel.}} = \tau_{\text{dimer}} - \tau_{\text{monomer}}$  are shown for neon, argon and krypton as a function of electron energy. For neon, only two sidebands are available (SB16 and SB18) with a delay difference of 15

---

<sup>1</sup>The IR intensity was set to a high value in an attempt to increase the sideband intensity of the weak dimer signal.

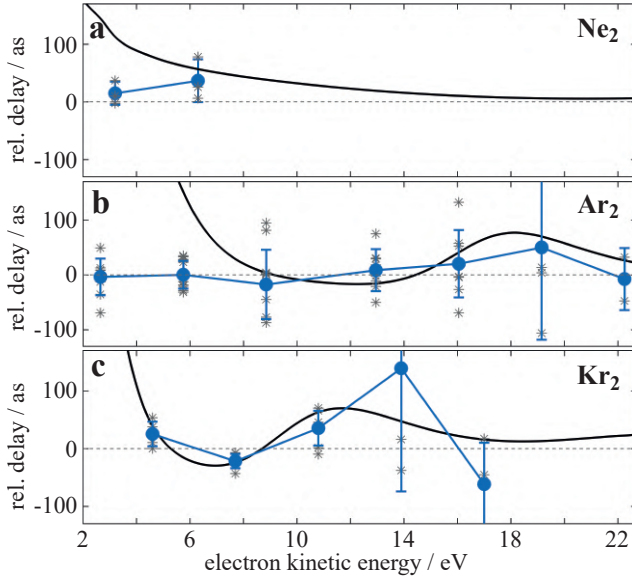


**Figure 6.4:** Relative ionization delays as a function of energy between dimer and monomer for **(a)** neon, **(b)** argon and **(c)** krypton. Filled blue circles give the mean of the experimental data with the standard deviation as error bars for an electron emission angle relative to the XUV polarization of  $\theta_{\text{Lab}} = 0 - 25^\circ$ . Grey asterisks show the individual relative delays of each data set. The black lines show theoretical one-photon ionization delay differences for  $\theta_{\text{Lab}} = 0^\circ$ . They were calculated using the ePolyscat molecular scattering code [206, 207].

( $\pm 17$ ) as and 36 ( $\pm 36$ ) as. With two experimental data points, it is of course not possible to observe an oscillation, but according to the calculated delay difference shown in Fig. C3, an oscillation is not expected until above 30 eV electron energy. Further, the significance of the standard deviation is unfortunately very limited due to the small number of data sets (only 3) available for neon.

In argon most of the relative delays are within  $\pm 15$  as with error bars significantly larger. Only at 19 eV electron energy the delay reaches 50 as, which coincides well with the calculated maximum of the oscillation at 18.2 eV. Unfortunately the error at this particular energy is too large ( $\pm 155$  as) to interpret the delay as caused by two-center interference.

This is different for krypton delays in 6.4 c, where the first three observed delays are 25 ( $\pm 20$ ) as, -22 ( $\pm 13$ ) as and 35 ( $\pm 30$ ) as. Also the delays at higher energies show a continuation of the oscillation with delays of 140 ( $\pm 200$ ) as and -60 ( $\pm 75$ ) as, however, with much larger error. Overall the calculated delay difference for  $\text{Kr}_2$  shown as a black line in 6.4 c, seems to agree well with the experiment, with a minimum at 6.8 eV and a maximum at 11.8 eV.

## Discussion

The relative ionization delays presented in Figure 6.4 show an increasing signature of two-center interference from  $\text{Ne}_2$  to  $\text{Kr}_2$ , which can be explained by the increasing internuclear distance of the rare gas dimers:  $R_{\text{Ne-Ne}}=3.337 \text{ \AA}$  [200],  $R_{\text{Ar-Ar}}=3.8 \text{ \AA}$  [201] and  $R_{\text{Kr-Kr}}=4.01 \text{ \AA}$  [202]. The dependence on the internuclear distance has already been observed by Ning et al. [195], where an intuitive picture for maxima in the Wigner delay of  $\text{H}_2^+$  is provided. The differential cross-section (DCS) in the molecular frame of  $\text{H}_2^+$  shows the signature of the semiclassical path interference between the emitted electron waves of the two centers. Destructive interference leads to minima in the DCS when electron momentum  $p_e$  and internuclear distance  $R$  satisfy the condition

$$p_e \cdot R = p_e R \cos \theta_{\text{Mol}} = (2n + 1)\pi \quad . \quad (6.2)$$

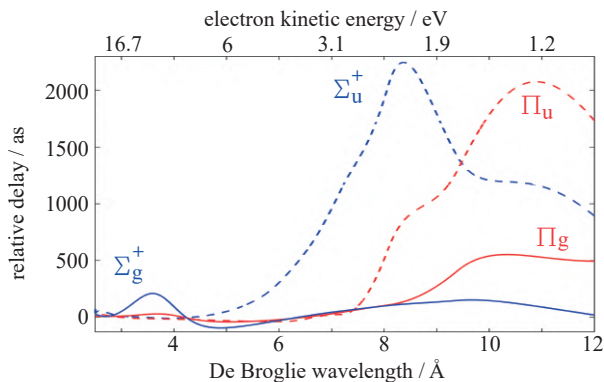


**Figure 6.5:** Orbital resolved one-photon ionization delays of  $\text{Kr}_2$  referenced to Kr as function of de Broglie wavelength of the photoelectron. Sigma states are shown in blue, Pi states in red, gerade parity with a solid line and ungerade parity with a dashed line.

The minimum in the differential cross-section is accompanied by a  $\pi$  phase shift in the transition matrix element (see chapter 2.1), leading to a maximum in the Wigner delay [195].

The effect of the internuclear distance can also clearly be observed in Fig. 6.4, where the local maxima of the calculated delays (black lines) are moving to lower energies from argon to krypton.

Interestingly it appears that this peak in the Wigner delay is observable even after integration along the angles in the molecular frame, since the experimental data as well as the calculations shown in Fig. 6.4 are angular averaged in the molecular frame and angular resolved in the laboratory frame. Further, the calculations in Fig. 6.4 are cross-section-weighted over all four molecular orbitals illustrated in Fig. 6.1 and hence the combination of states with gerade and ungerade parity should lead to at least some cancellation of an observable interference [197]. Indeed, an investigation of the orbital resolved delays of the krypton dimer in Figure 6.5 reveals that the delays of orbitals with gerade and ungerade symmetry exhibit some - although weak - anti-cyclic behavior. Here the orbital resolved relative delays are shown as a function of the de Broglie wavelength

$\lambda_{dB} = h/p_e$ , where  $p_e$  is momentum of the photoelectron. A peculiarity we note is that both gerade states show a maximum around 3.7 Å, while the states of ungerade parity have a maximum around 8.4 Å, roughly coinciding with  $R_{\text{Kr-Kr}}$  and  $2R_{\text{Kr-Kr}}$  respectively. However, the magnitude of the local maxima vary significantly for each of the four orbitals, which is also the reason of the surviving oscillation in the full, cross-section weighted calculation.

Experimentally, the combination of orbitals with different parity is actually mostly prevented due to analysis of electrons in coincidence with the stable dimer ions. In Figure 6.6, the potential energy of a charged rare gas dimer  $\text{Rg}_2^+$  is sketched as a function of internuclear distance. From the potential energies and the indicated Franck-Condon region for ionization from the neutral ground state it can be seen that by far the most stable ionic dimer results from ionization out of the  $\sigma_u$  molecular orbital. This is additionally supported by work of high resolution threshold photoelectron spectroscopy of  $\text{Ne}_2$ ,  $\text{Ar}_2$  and  $\text{Kr}_2$ , which found that ionization out of the  $\sigma_u$  orbital has a much higher cross-section than ionization out of the  $\pi_u$  and  $\pi_g$  orbitals for all species [208]. This allows the conclusion that the experimental delays reported in Fig. 6.4 are almost exclusively from the  $\sigma_u$  molecular orbital, which one would expect to result in a stronger observable of two-center interference than an equally weighted contributions from all states. However, close scrutiny of the orbital resolved delays in Fig. 6.5 reveals that the  $\Sigma_u^+$  state does not have any local maximum below 6 Å (e.g. above 4.1 eV) but is flat in the region where the oscillation is observed in the experimental delays.

This discrepancy between experimental and theoretical observation has not been resolved at the time of writing and is still being investigated. A possible source of errors could lie in the simple nature of the calculations presented here, which are based on Hartree-Fock (HF) wavefunctions and for which no proper convergence tests have been performed at the time of writing. The HF method is known to have limited accuracy in describing open-shell molecular systems. Additionally, scattering calculations for low energy electrons



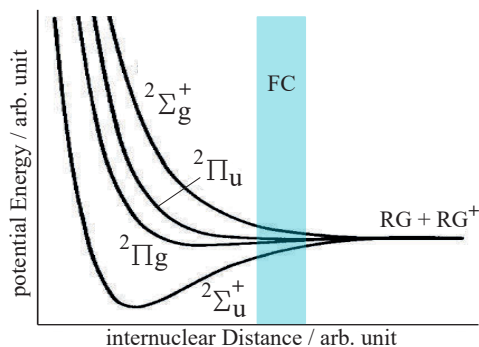


**Figure 6.6:** Schematic drawing of the potential energy of an ionized rare gas dimer  $Rg_2^+$ , as a function of internuclear distance. The Franck-Condon region for ionization from the neutral ground state is marked by the blue opaque area. Note that spin-orbit coupling is omitted for simplicity. Adapted from [208, 209], which used the polarization configuration interaction (POL-CI) method for calculations [210].

are methodologically particularly demanding and typically theoretical Wigner delays are only shown for electron energies larger than  $\sim 5$  eV [28, 29, 75, 76].

## 6.2 Molecular-Frame-Resolved Delays of Neon Dimer

As can be seen in Figure 6.2, neon is the only rare gas measured that does not form clusters larger than the dimer<sup>2</sup>. Due to this circumstance it is possible to ascribe any of the  $Ne^+$  ions with kinetic energy to the neon dimer and hence to access the electrons of a dissociation channel of  $Ne_2^+$  in the molecular frame. By extracting RABBIT spectrograms for specific angles between the  $Ne^+$  ion momentum and electron momentum one can then obtain ionization delays for the respective electron emission direction in the molecular frame.

<sup>2</sup>This can be concluded from the missing broad distribution around the sharp dimer peak, which implies that there are no  $Ne_2^+$  ions originating from fragmentation of a larger cluster.

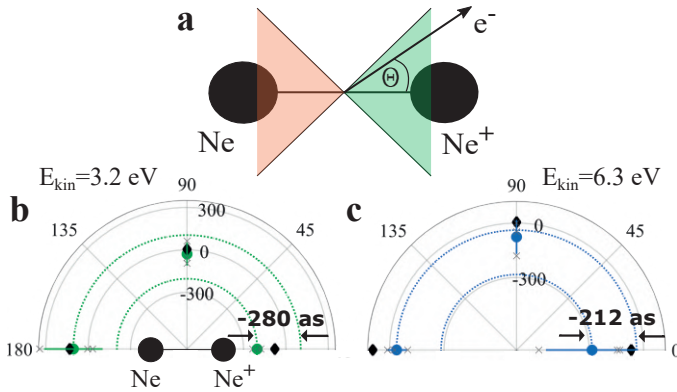


**Figure 6.7:** Molecular frame ionization delays of  $\text{Ne}_2^+$  relative to  $\text{Ne}^+$  for (b) SB16 and (c) SB18. (a) Sketch of the molecular frame of  $\text{Ne}_2^+$  with the emission direction of the electron defined by the polar angle  $\theta = \theta_{\text{Mol}}$  in the molecular frame. The orange and green area indicating the angular cone for emission left or right along the molecular axis respectively. The angular ranges for the shown delays are:  $\theta_{\text{Mol}} = 0 - 45^\circ$ ,  $\theta_{\text{Mol}} = 45 - 135^\circ$  and  $\theta_{\text{Mol}} = 135 - 180^\circ$ . For all of them the reference is  $\text{Ne}^+$  with  $\theta_{\text{Lab}} = 0 - 45^\circ$  and  $\theta_{\text{Lab}} = 135 - 180^\circ$ . Grey asterisks represent delays from individual data sets, filled circles show the mean and the error bars are the standard deviation. Theoretical one-photon ionization delays for a localized electron hole and for the same angular ranges are plotted as black diamonds. Dashed half circles are drawn at the experimental delay values of left and right emission directions to guide the eye. Theoretical calculations were performed by Robert Luchese.

Unlike in chapter 4, where delays for several emission directions in the recoil frame of  $\text{CF}_4$  were extracted, here it was only possible to analyze three angular ranges of the polar angle  $\theta_{\text{Mol}}$  in the molecular frame due to insufficient statistics.

Figure 6.7 shows the relative ionization delays between  $\text{Ne}_2^+$  and  $\text{Ne}^+$  for three different angular ranges of the polar angle  $\theta_{\text{Mol}}$  in the molecular frame of the neon dimer. A strong left-right asymmetry of the delays can be observed with the delays for electron emission parallel to the axis along the neutral atom and orthogonal to the molecular axis being almost zero, whereas for electron emission along the ion, large negative delays of more than -200 as for both sideband 16 (Fig. 6.7 b) and sideband 18 (Fig. 6.7 c) were measured.

In order to observe an asymmetry along the axis of a diatomic molecule, it is necessary to break the symmetry of the molecule. One possibility to achieve this is in a diatomic heteronuclear molecule, as it was done by Vos and coworkers when they measured an asymmetry of the ionization delays in the molecular frame of CO [75]. Interestingly, they observed a delay difference of more than -150 as, with the smaller delay measured for the electron emitted along the ion direction, analogous to our observation. Due to  $\text{Ne}_2$  being a homonuclear diatomic with a fully symmetric ground state, other ways to break the symmetry must be considered. In this case, breaking the symmetry requires a coherent mixing of states with gerade and ungerade parity, which leads to (partial-) localization of the orbital [211]. This approach of symmetry breaking in homonuclear diatomic molecules has been demonstrated multiple times by means of an external laser field coupling states of different parity [212–216], through the entanglement of autoionizing states of different parity [217, 218] and even through the coupling of g and u states through the photoelectrons Coulomb field [219, 220].

Due to the particularly strong laser field that was used in the case of the neon measurement (see Fig. 6.8), a coupling of g and u through the IR field seems to be a realistic possibility. This is further supported by the particularly strong coupling between the  $\Sigma_g$  and  $\Sigma_u$  states due to large transition dipole moments in rare gas dimers [221, 222].

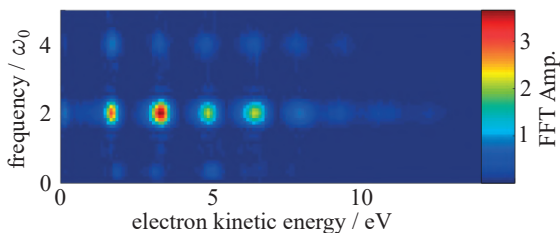


**Figure 6.8:** FFT amplitude of neon RABBIT spectrogram shown in Fig. C2a. The presence of an oscillation at  $4\omega_0$  is a sign of continuum-continuum transitions including 2 IR photons due to high IR intensity.

The localization of the electron hole on one side of the molecule as a consequence of the coherent superposition of gerade and ungerade wavefunction presents a simple explanation for the asymmetric ionization delays along the molecular axis of  $\text{Ne}_2$ . The localization results in a non-centered starting position of the electron wavefunction, which then experiences a different potential landscape for left or right emission direction. The dependence on the mean position of the electron along the molecular axis has also been suggested as the source of asymmetric ionization delays in CO [75]. This interpretation is further supported by preliminary theoretical calculations of the angular resolved one-photon ionization delays for a localized electron hole in the photoionization of  $\text{Ne}_2$ , shown as black diamonds in Fig. 6.7. Those calculations were performed by Robert Lucchese using the ePolyscat molecular scattering code [206, 207]. Good qualitative agreement is observed with delay asymmetries of -209 as (SB16) and -160 as (SB18) in the calculations.

However, so far no mechanism causing a symmetry breaking in  $\text{Ne}_2$  could be unambiguously identified and, both experimental and theoretical, investigations are still ongoing at the time of writing. Further, the large error bars in combination with the limited number of data points prevents one from drawing a final conclusion, highlighting the need for additional experimental studies.

## 6.3 Conclusion and Outlook

In this chapter the role of localization and delocalization in the photoionization delays of rare gas dimers was discussed and first experimental results were presented. Delocalization of the electron hole in a diatomic molecule results in two-center interference, which manifests itself in an observable change in the Wigner delay [195]. So far, the effect of two-center interference on the Wigner delay has been investigated only theoretically [193–195] and the results presented here constitute a first experimental attempt. By studying several rare gas dimers it is possible to investigate the influence of the internuclear distance on the ionization delays. For  $\text{Kr}_2$  an oscillating delay as a function of electron energy is observed, which might be a signature of two-center interference.

Further, an indication for at least partial localization of the electron hole has been observed in the molecular-frame ionization delays of  $\text{Ne}_2$ . In this case the IR field necessary for the RABBIT experiment might couple states of gerade and ungerade parity, leading to partial localization of the electron hole, which in turn causes a highly asymmetric ionization delay along the molecular axis of  $\text{Ne}_2$ .

The difficulties of these experiments are mainly due to the very low dimer yield in the cluster generation, which requires long acquisition times (approximately 48 h per data set). Because it is challenging to maintain stable experimental conditions over such a long period of time, the quality of the experimental data presented in this chapter, does not allow to reach a final conclusion on this topic. Instead, this chapter should motivate further experimental and theoretical investigations of ionization time delays in rare gas dimers, where the occurrence of effects associated with both orbital localization and delocalization, provide an exciting subject to study.

In particular with high repetition laser sources becoming more broadly available, the experiments will become easier to realize and efforts can be undertaken to improve the angular resolution in the molecular frame of  $\text{Ne}_2$  and other rare gas dimers, where the effect

of two-center interference is expected to be much stronger [195] and can be studied in more detail. Also interesting would be the investigation of these effects in the xenon dimer, which has an even larger internuclear distance of  $R_{\text{Xe-Xe}} = 4.36 \text{ \AA}$  [223]. Due to the spin orbit splitting of 1.31 eV between  $\text{Xe}^+ \ ^2P_{1/2}$  and  $\text{Xe}^+ \ ^2P_{3/2}$ , a better energy resolution than available in the present experimental setup, is necessary to clearly resolve sideband and mainband peaks which are separated by 1.55 eV in the present experimental conditions.

# Chapter 7

## Conclusion

In this thesis, the combination of attosecond spectroscopy and coincidence detection was leveraged to investigate the photoionization time delays of molecules and clusters in ways that have previously not been attempted. The results presented provided new insights into the electron dynamics in molecular systems and serve as an example of the possibilities that can be achieved by combining attosecond and coincidence spectroscopy. This thesis shall thereby motivate further experimental investigations of more complex systems that will increase our understanding of electron dynamics in molecules.

A COLTRIMS type detector, combined with an XUV-IR interferometer had been used to measure 3D momentum- and time-resolved electron and ion spectra of molecules and clusters. Following the RABBIT technique, ionization time delays were extracted and their dependence on electron emission angle in the molecular and laboratory frame, electron-kinetic-energy dependence and cluster-size dependence was investigated.

In chapter 4 the coincidence technique allowed for the simultaneous measurement of  $\text{CF}_4$  and argon, where the HOMO of  $\text{CF}_4$  has a similar ionization potential as the HOMO of Ar. Thereby it was possible to experimentally cancel effects of laser-induced delays and determine the ionization time delay in the presence of strong shape resonances. Further, detecting electrons in coincidence with the 3D momentum-resolved  $\text{CF}_3^+$  ion made it possible to analyze the angular resolved ionization time delays in the recoil frame of  $\text{CF}_4$ . For the first time, ionization delays in the entire angular space in reference to the molecular axis were extracted and the highly structured RAPIDs could be explained with a partial-wave analysis of the RABBIT delays. This type of analysis procedure is in principal not limited by the size of the molecule and fully molecular-frame-resolved ionization delays of more complex systems can be envisioned.

Due to the coincidence capabilities it was also possible to compare the photoionization delays of clusters with different sizes, for the first time, which was demonstrated in chapter 5. In water clusters, it was shown that an increase in cluster size causes a simultaneous increase in ionization delay. This could be attributed to the increasing orbital delocalization in the clusters due to an increase in symmetry. When the cluster size exceeds 4 molecules, structural disorder sets in and causes the partial localization of orbitals. At this point the ionization delay converges to a constant value, which is close to the time delay previously measured in liquid water. Thereby, the underlying principle, or at least an important contribution to the changing ionization time delays from gas-phase to liquid-phase water could be unraveled.

In addition to water clusters, it could be shown that a similar increase of the ionization delays is measured in argon clusters, which indicates a more general validity of the correlation between ionization delays and orbital localization/delocalization, promising to reveal new insights about the electronic structure for many other systems.



Chapter 6 covered the fundamental quantum effect of two-center interference in homonuclear diatomics. The comparison of electron-energy resolved ionization delays between different rare gas dimers and their monomers, revealed the dependence of interference maxima and minima on the internuclear distance. In  $\text{Kr}_2$  an experimental indication is found that the quantum interference of the two-center photoemission imprints itself onto the ionization delay of the electron. Additional experimental and theoretical work is needed to investigate this effect further. Rare gas dimers provide an ideal system due to the range of internuclear distances available for the different rare gas dimers as well as the comparison with the monomers which cancels any laser-induced delays.

With the coincidence capabilities it was also possible to study ionization delays in the molecular frame of the neon dimer, which revealed strongly asymmetric delays along the molecular axis. This symmetry breaking fundamentally requires a localization of the electron hole, which is in direct contradiction to the delocalization of the orbital required for the two-center interference. The role of localization and delocalization of the orbitals in homonuclear diatomics is still an open question and the ionization delays in  $\text{Ne}_2$  provide an exciting system to investigate this very fundamental problem further.



# Appendix A

## Supplementary Material for 'Attosecond Interferometry of Shape Resonances in the Recoil Frame of CF<sub>4</sub>'

Saijoscha Heck,<sup>1</sup> Denitsa Baykusheva,<sup>2†</sup> Meng Han,<sup>1</sup> Jia-Bao Ji,<sup>1</sup> Conaill Perry,<sup>1</sup> Xiaochun Gong<sup>1,3</sup> and Hans Jakob Wörner<sup>1†</sup>

<sup>1</sup> Laboratorium für Physikalische Chemie, ETH Zürich, 8093 Zürich, Switzerland,

<sup>2</sup> Department of Physics, Harvard University, Cambridge, Massachusetts 02138, USA

<sup>3</sup> State Key Laboratory of Precision Spectroscopy, East China Normal University, Shanghai, China

† E-mail: dbaykusheva@g.harvard.edu, hwoerner@ethz.ch.

## Theoretical methodology

### Quantum-scattering Calculations

The calculation of the CF<sub>4</sub> photoionization matrix elements  $M_{1hv,a/e}^{\Gamma_0}(E_{\text{SB}}^{\leq}, \vartheta, \varphi)$  has been performed using the ePolyScat molecular scattering codes described in Refs. [45, 46]. The electronic struc-

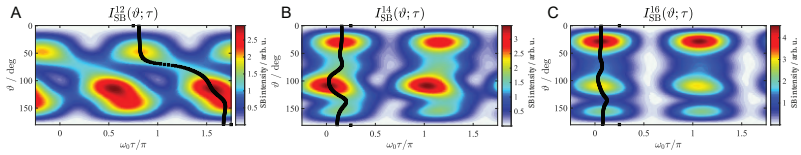


**Figure A1:** Calculated angle-resolved sidebands for the  $1t_1$  HOMO of  $\text{CF}_4$ . Theoretically predicted sideband intensity for SB12 (A), SB14 (B), and SB16 (C), displayed as a function of the emission angle  $\vartheta$  and the XUV-IR delay  $\tau$ . The black dots signify the position of the extremal phase  $\Phi_{\text{Mol}}(E_{\text{SB}}, \vartheta)$  at each angle.

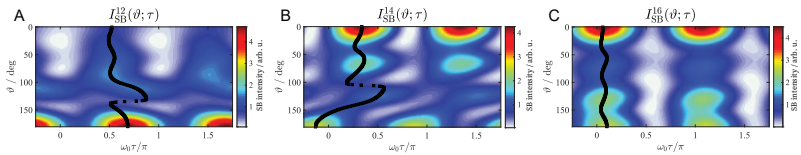


**Figure A2:** Calculated angle-resolved sidebands for the  $4t_2$  HOMO-1 of  $\text{CF}_4$ . Theoretically predicted sideband intensity for SB12 (A), SB14 (B), and SB16 (C), displayed as a function of the emission angle  $\vartheta$  and the XUV-IR delay  $\tau$ . The black dots signify the position of the extremal phase  $\Phi_{\text{Mol}}(E_{\text{SB}}, \vartheta)$  at each angle.

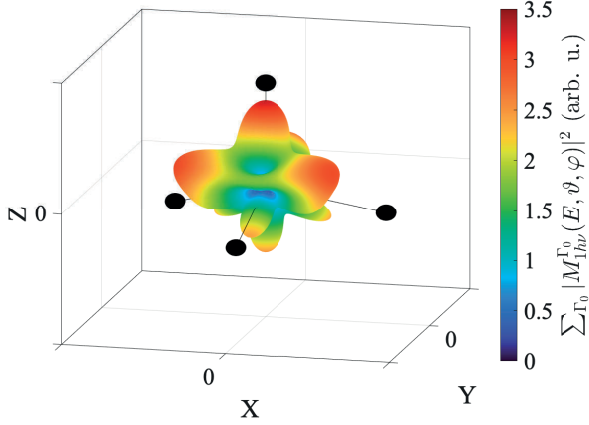


**Figure A3: Calculated MFPAD for photoionization from the  $4t_2$  (HOMO-1) channel.** The shown MFPAD corresponds to an electron kinetic energy of  $E_{kin} = 3.2$  eV. The Euler angles are set at  $\alpha = 0^\circ, \beta = 0^\circ$ , i.e. the laboratory and the molecular frames coincide. The black spheres show the positions of the fluorine atoms.

ture of  $\text{CF}_4$  has been calculated with the Hartree-Fock (HF) method using a cc-pVTZ basis set. The single-center partial-wave expansion in the scattering calculations has been truncated at  $l_{max} = 60$ , which ensures converged results. Given the set of matrix elements  $I_{lm\mu}(E)$  output by ePolyScat, the emission- and orientation-angle-dependent photoionization matrix elements have been calculated via:

$$M_{1h\nu}^{\Gamma_0}(E, \vartheta, \varphi) = \sum_{lm\mu} I_{lm\mu}^{\Gamma_0} Y_{lm}(\vartheta, \varphi) Y_{1\mu}(\beta, \alpha) \quad (7.1)$$

The molecular frame employed in the theoretical calculation is depicted in Fig. A3 and Fig. 4.3 of the main text. The molecular z-axis corresponds to the emission angle  $(\vartheta, \varphi) = (0, 0)$ , i.e.  $(\vartheta = 0, \varphi = 0)$  points along the (dissociating) C–F bond. For illustrative purposes, in Fig. A3 we also plot the squared amplitude of a selected MF-angle-resolved matrix element at  $\alpha = 0, \beta = 0$ . This quantity corre-

sponds to the molecular-frame photoelectron angular distribution, MFPAD.

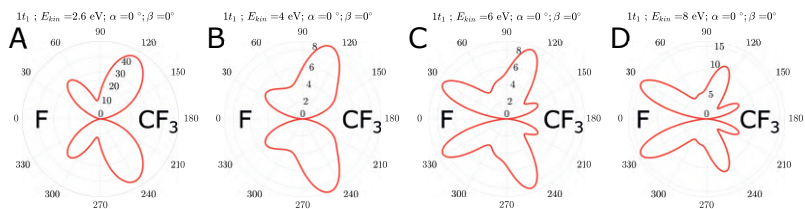


**Figure A4: Calculated MFPADs.** The MFPADs for the  $1t_1$  (HOMO) channel shown in this figure have been calculated with ePolyScat, i.e. the same methodology used for the calculation of the time delays.

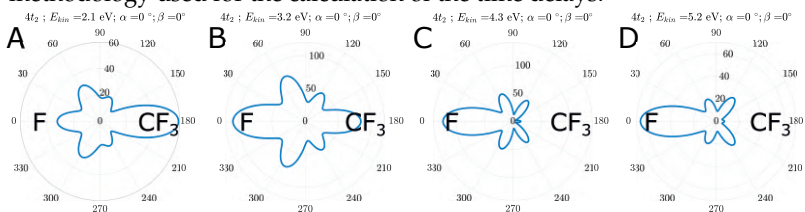


**Figure A5: Calculated MFPADs.** Same as Fig. A4 for the  $4t_2$  (HOMO-1) channel. The overall very good agreement with, both, experimental MFPADs and more sophisticated multi-channel calculations based on the complex Kohn variational method [108], both shown in Fig. A6, demonstrate the accuracy of the ePolyScat calculations.

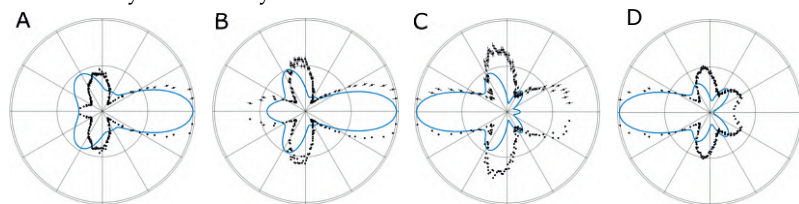


**Figure A6: Experimental and calculated MFPADs of the  $4t_2$  (HOMO-1) channel from previous work.** MFPADs adapted from Larsen et al. [108], shown here to demonstrate the agreement of our calculations with previous experimental and theoretical data. (A)  $E_{kin}=2.1$  eV, (B)  $E_{kin}=3.2$  eV, (C)  $E_{kin}=4.3$  eV and (D)  $E_{kin}=5.2$  eV.

To assess the accuracy of the ePolyScat calculations used in our work, MFPADs obtained with the photoionization matrix elements described above have been compared to previous calculations and experimental data presented in Ref. [108]. Figure A4 displays the MFPADs for photoionization from the HOMO and Figure A5 from the HOMO-1 of  $\text{CF}_4$ . The direct comparison of Figs. A5 and A6 validates the accuracy of our calculations.

## Laboratory-Frame angular resolved delays

In Figure 4.2 of the main text we show laboratory frame angular resolved delays for an emission angle of  $0\text{-}18^\circ$ . This angle was chosen, because it is the angular range with the most electron yield and also with the best energy resolution. Nevertheless, the question arises how much the delays caused from the shape resonances depend on the choice of emission angle. In Fig. A7 we show the ionization delays of  $\text{CF}_4$  for both HOMO and HOMO-1 referenced to argon, with an electron emission angle of  $25^\circ\text{-}55^\circ$ . The black solid line shows the calculated RABBIT delays for the same angular range and reference. It can be seen, that also in this angular range the agreement between theory and experiment is good. Further, there is no qualitative difference of the delays observed for the angular range of  $0\text{-}18^\circ$ , shown in Figure 4.2. Due to the choice of electric and magnetic field parameters, we are unable to access delays for full angular integration.

## Partial wave analysis of the RABBIT delays

In this section, we present a detailed analysis of the photoionization cross sections and RABBIT delays discussed in this work on the basis of a partial wave decomposition. This approach clarifies the key mechanisms underlying the photoelectron trapping in the shape resonances and its manifestation in the measured RABBIT delays.

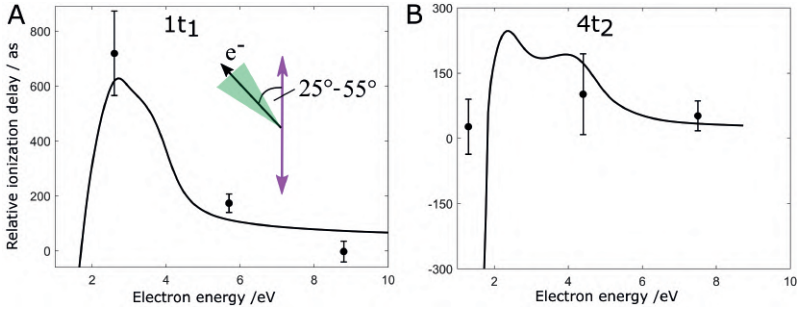


**Figure A7: Laboratory-Frame Photoionization delays.** Delays for channel (A)  $1t_1$  and (B)  $4t_2$ . Black filled circles show the experimental values, the black solid line shows the calculated RABBIT delays. Both experimental and theoretical delays are for electrons emitted  $25^\circ$ - $55^\circ$  with respect to the XUV polarization and are referenced to argon using the same angular integration range. The emission angle is visualized in the inset of (A), where the green shaded area shows the angular range and the purple double arrow indicates the XUV polarization. The error bars show the standard deviation of the delays extracted from multiple data sets.

We first discuss the HOMO channel. Figure A8 shows the cross section of the  $1t_1 \rightarrow kt_2$  photoionizing transition. It clearly reveals the presence of a shape resonance at a kinetic energy of  $\sim 2.3$  eV, which is dominated by an f-wave ( $l = 3$ ) contribution. No shape resonances have been found in the relevant energy range in the other continuum symmetries ( $a_2$ , e and  $t_1$ ).

The HOMO-1 channel features two shape resonances, one of  $a_1$  symmetry (Fig. A9A) and one of  $t_2$  symmetry (Fig. A9B). The two resonances lie close in energy and overlap within their respective widths. Both of them are dominated by f-wave contributions, as in the case of the HOMO channel. The  $a_1$  shape resonance additionally has contributions from s- ( $l = 0$ ) and g- ( $l = 4$ ) waves, whereas the  $t_2$  shape resonance has p- ( $l = 1$ ) and d- ( $l = 2$ ) wave contributions. We note that p- and d-waves do not contain the totally symmetric irreducible representation and are therefore excluded from contributing to the  $a_1$  shape resonance by symmetry.



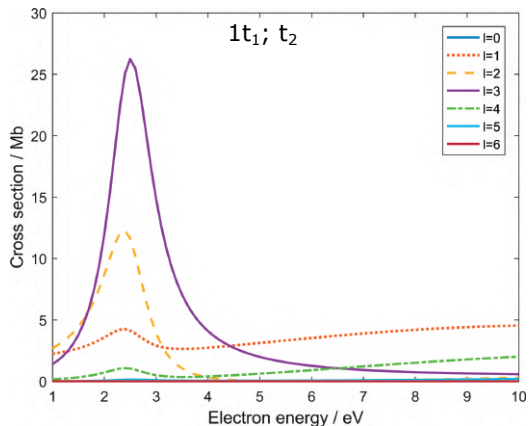


**Figure A8:** Partial-wave decomposition of the HOMO( $1t_1$ )  $\rightarrow$   $kt_2$  cross section.

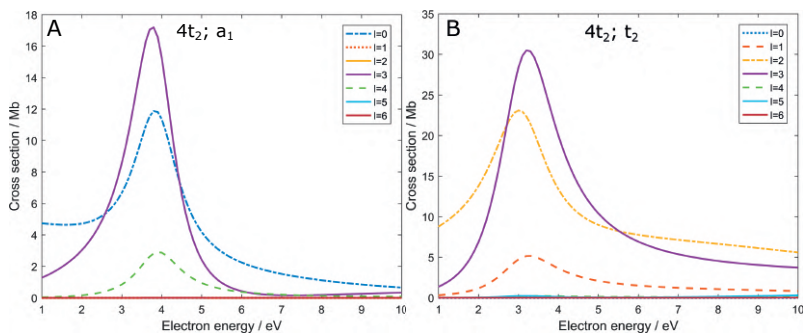


**Figure A9:** Partial-wave decomposition of the HOMO-1 cross sections. For channels (A) HOMO-1  $\rightarrow$   $ka_1$  and (B) HOMO-1  $\rightarrow$   $kt_2$ .

To determine the lifetimes of the respective resonances we fit the symmetry-resolved cross sections using the Fano formalism [224]

$$f(x) = A \frac{(q + \frac{x-E_0}{\Gamma/2})^2}{1 + (\frac{x-E_0}{\Gamma/2})^2} + B, \quad (7.2)$$

channel	lifetime		resonance	Fano
	$\tau / \text{as}$	$\Gamma / \text{eV}$	position $E_0 / \text{eV}$	parameter $q$
$1t_1 \rightarrow kt_2$	650	1.01	2.43	26.8
$4t_2 \rightarrow ka_1$	457	1.44	3.91	-7.6
$4t_2 \rightarrow kt_2$	370	1.78	3.02	6.67

**Table A1: Lifetimes and Fano-fit parameters of shape resonances.**

where  $q$  is the Fano parameter,  $\Gamma$  the linewidth,  $E_0$  the resonance position,  $A$  an amplitude and  $B$  an offset. The lifetime is then calculated with the relation  $\tau = \hbar/\Gamma$ . In Table A1 we show the resonance lifetimes together with the fit parameters.

In the following, we study the angle dependence of the photoionization delays in the molecular frame and analyze the contributions of individual partial waves. When the analysis is restricted to a single partial wave, we always obtain delays that are forward-backward symmetric along the dissociation axis. Any asymmetry is therefore the signature of the interference of at least two partial waves. In the following, we hence chose different subsets of partial waves and displayed the corresponding molecular-frame RABBIT delays. For all partial-wave resolved delays shown, the cc-contribution and the argon reference delays are omitted. The partial-wave analysis of the RABBIT delays in the HOMO channel is shown in Fig. 4.3 of the main text. Here, we present the corresponding analysis of the HOMO-1 channel.

As shown in Fig. A9 and Fig. 4.2 of the main text, the HOMO-1 channel contains two overlapping shape resonances of symmetries  $a_1$  and  $t_2$ , respectively. Here, we discuss the partial-wave decomposition of the angle-resolved photoionization delays for each continuum symmetry separately first, before showing the results of the complete calculation.

Figures A10 and A11 show the delays obtained from a calculation that is restricted to the  $a_1$  continuum symmetry and  $l = 0, 3$  or  $l = 0, 3, 4$ , respectively. Note that  $l = 1, 2$  are not contributing to the  $a_1$  continuum symmetry. The comparison of the two figures shows that the qualitative asymmetry of the delays is already captured by  $l = 0, 3$  alone. In SB12, the addition of  $l = 4$  has a large effect, both on the angular variation and the absolute values of the delays, whereas it has only a minor effect in the case of SB14 and SB16.

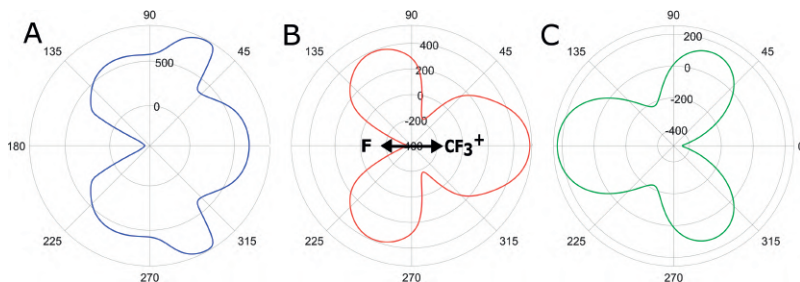


**Figure A10: Partial-wave-resolved RABBIT delays of the HOMO-1 channel with continuum symmetry  $a_1$ .** Restricted to the contributions of partial waves with  $l=0$  and  $3$  for (A)  $E_{\text{kin}}^{\text{CF}_4}=1.55$  eV for SB12, (B) SB14 and (C) SB16. All delays are referenced to argon.

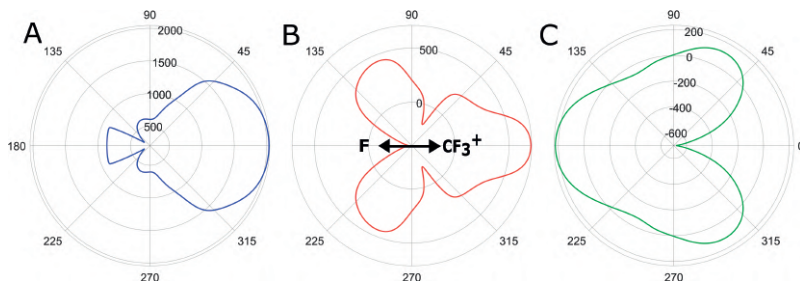


**Figure A11: Partial-wave-resolved RABBIT delays of the HOMO-1 channel with continuum symmetry  $a_1$ .** Restricted to the contributions of partial waves with  $l=0, 3$  and  $4$  for (A)  $E_{\text{kin}}^{\text{CF}_4}=1.55$  eV for SB12 (B) SB14 and (C) SB16. All delays are referenced to argon.

Figures A12 and A13 show the delays obtained from a calculation that is restricted to the  $t_2$  continuum symmetry and  $l = 2, 3$  or  $l = 1, 2, 3$ , respectively. Note that  $l = 0$  is not contributing to the  $t_2$  continuum symmetry. The comparison of the two figures again shows that most features in the angular dependence of the delays are already captured by  $l = 2, 3$  alone. In SB12, the addition of  $l = 1$  has a visible effect on the angular variation of the delays, whereas it has only a minor effect in the case of SB14 and SB16.

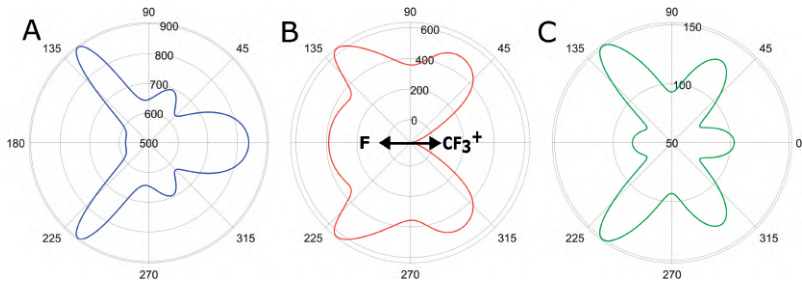


**Figure A12: Partial-wave-resolved RABBIT delays of the HOMO-1 channel with continuum symmetry  $t_2$ .** Restricted to the contributions of partial waves with  $l = 2$  and  $3$  for (A)  $E_{\text{kin}}^{\text{CF}_4} = 1.55$  eV for SB12, (B) SB14 and (C) SB16. All delays are referenced to argon.

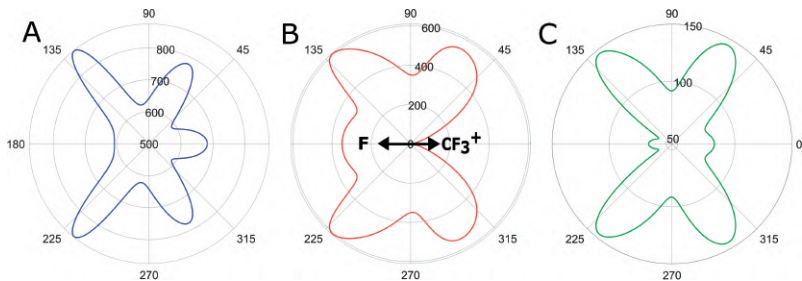


**Figure A13: Partial-wave-resolved RABBIT delays of the HOMO-1 channel with continuum symmetry  $t_2$ .** Restricted to the contributions of partial waves with  $l = 1, 2$  and  $3$  for (A)  $E_{\text{kin}}^{\text{CF}_4} = 1.55$  eV for SB12, (B) SB14 and (C) SB16. All delays are referenced to argon.

Figure A14 shows the angle-resolved delays obtained by including all continuum symmetries and all significantly contributing partial waves ( $l = 0 - 4$ ). The comparison with Figs. A11 and A13 shows that the total delays are not a simple linear combination of the delays obtained for specific continuum symmetries. The importance of interference phenomena is further supported by the direct comparison of the results of a coherent and incoherent addition of the symmetry-resolved photoionization matrix elements in Fig. 4.4 of the main text.

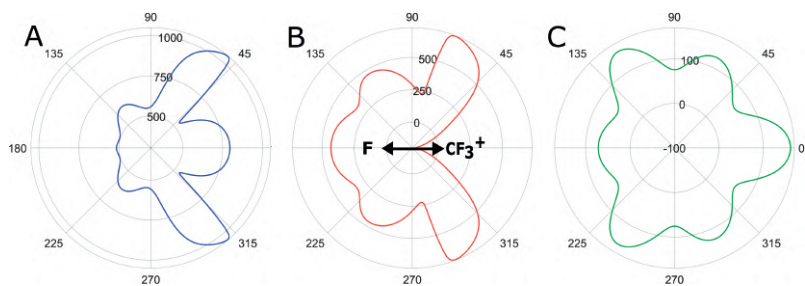


**Figure A14: Partial-wave-resolved RABBIT delays of the HOMO-1 channel with all continuum symmetries.** Restricted to the contributions of partial waves with  $l = 0, 1, 2, 3$  and  $4$  for (A)  $E_{\text{kin}}^{\text{CF}_4} = 1.55$  eV for SB12, (B) SB14 and (C) SB16. All delays are referenced to argon.

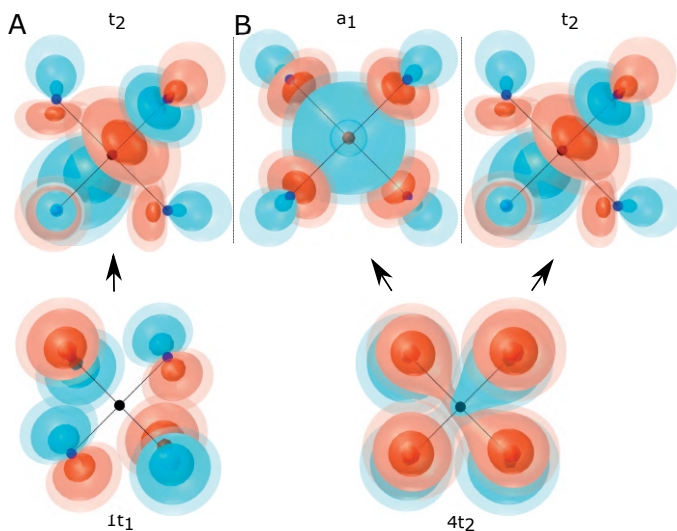
## Graphical representations of the shape-resonance wavefunctions

In this section, we discuss the continuum wave functions at the energies of the three relevant shape resonances in more detail. These wavefunctions were obtained using the resonance-search algorithm implemented in ePolyScat [45, 46]. These calculations use a single-active-electron approximation and are therefore slightly less accurate than the regular ePolyScat calculations used throughout the remainder of this work. They nevertheless have the benefit of providing the energy positions, lifetimes and single-electron continuum wavefunctions of the shape resonances, which offer an intuitive understanding of their spatial and temporal properties.

Both the initial orbitals as well as the resonant wavefunctions are calculated in a coordinate system where the C-F bonds span a tetrahedron with vertices given by  $(\pm r_{\text{CF}} \cos \alpha/2, \pm r_{\text{CF}} \cos \alpha/2, \pm r_{\text{CF}} \cos \alpha/2)$  with  $\alpha = \arccos 1/3$ . Choosing the electric field vector to lie along one of the C-F bonds (e.g. (1,1,1)) will thus create a superposition of all three degenerate wavefunction components:

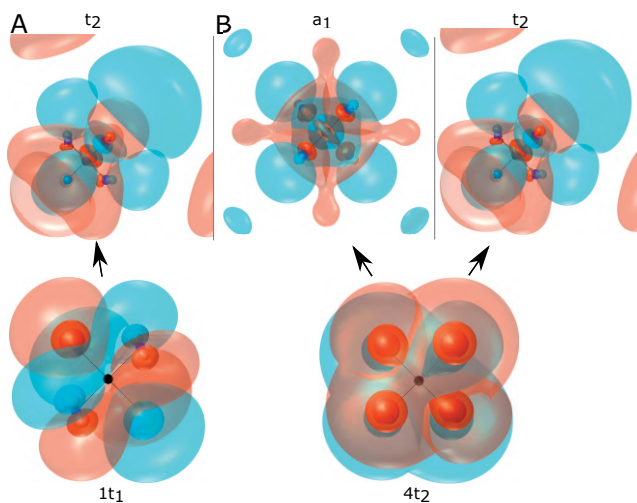
$$1/\sqrt{3}(1t_1^{(x)} + 1t_1^{(y)} + 1t_1^{(z)}).$$

Figure A15 shows the wave functions of the bound  $1t_1$  and  $4t_2$  orbitals, as well as the continuum wave functions of the three shape resonances that were studied in this work. Two of these continuum wavefunctions are also shown in Fig. 4.2C,D of the main text. Here, we note that the  $t_2$  shape resonances in both channels have nearly identical wave functions, which suggests that they are actually closely related to each other, although accessed from different initial orbitals. This is a remarkable observation because the two  $t_2$  resonances are located at different photon energies in the two channels and have different lifetimes. Specifically, the  $4t_2 \rightarrow t_2$  resonance lies higher in photon energy and has a shorter lifetime than the  $1t_1 \rightarrow t_2$  resonance.



**Figure A15: 3-dimensional orbital wavefunctions.** (A) Orbital wavefunctions for the  $1t_1$  HOMO (bottom) and the  $t_2$  continuum wavefunction at the resonance energy (top). (B) same as (A) for the  $4t_2$  HOMO-1 and the  $a_1$ , as well as  $t_2$  resonant wave functions. The position of the atoms is indicated with black/blue spheres for C/F, respectively. Contour levels used are: 0.8, 0.7, 0.35, 0.15 and 0.09.

The isocountour values chosen in Fig. A15 have the advantage of emphasizing the nature of the shape resonances, i.e. the molecular cage effect, but the disadvantage of not clearly displaying the continuum character of the corresponding wave functions. We therefore chose a different set of isocontour values for the same wavefunctions in Fig. A16. Here, the bound character of the molecular orbitals and the infinite extension of the continuum wave functions is more clearly visualized.



**Figure A16: 3-dimensional orbital wavefunctions with lower isocontour values.** Same as Fig. A15, but with lower isocontour values to emphasize the diffuse contributions to the shape-resonant wave functions. Contour levels used are: 0.8, 0.6, 0.4, 0.22, 0.0145.



## Calculation of the potential energy surfaces of $\text{CF}_4^+$

The potential-energy surfaces shown in Fig. 4.1A of the main text were obtained as follows. First, one of the C-F bond lengths was fixed to one of 25 values in a constrained structure optimization of  $\text{CF}_4^+$  with unrestricted DFT employing the BP86 functional and the def2-TZVP basis set. For each of these structures, the six lowest-lying electronic states were calculated at the SA-CASSCF(23,16) level of theory using the relativistic X2C Hamiltonian and the ANO-RCC basis set with triple-zeta contraction. This active space contains all valence orbitals except for the energetically well-separated 2s-orbitals of the fluorine atoms.

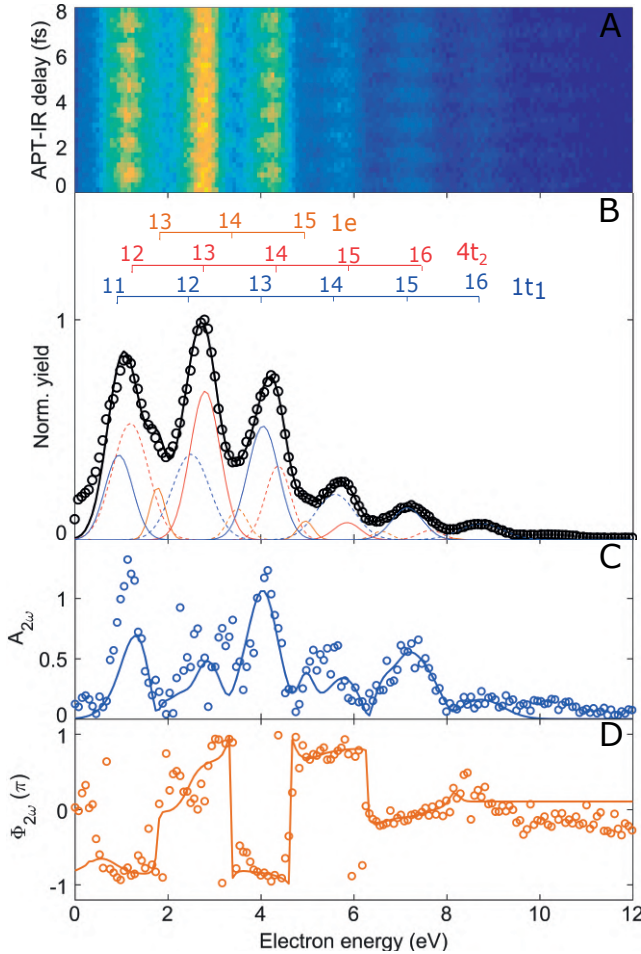


**Figure A17: Phase retrieval from overlapping photoelectron signals of  $\text{CF}_4$ .** (A) Laboratory-frame angle-resolved RABBIT spectrum with an angle between electron direction and XUV polarization of  $0$ - $18^\circ$ . (B) Fitted energy spectrum of  $\text{CF}_4$ . The electron energies from the three energetically accessible states are fitted according to their cross section and XUV intensities using Gaussians. (C) Amplitude at  $2\omega$  of a Fourier Transformation of the RABBIT spectrum shown in (A). (D) Phase at  $2\omega$  of the same Fourier Transformation.

# Appendix B

## Supplementary Material for 'Attosecond spectroscopy of size-resolved water clusters'

X. Gong<sup>1,2,\*</sup>, S. Heck<sup>1,\*</sup>, D. Jelovina<sup>1</sup>, C. Perry<sup>1</sup>, K. Zinchenko<sup>1</sup>, H. J. Wörner<sup>1,†</sup>

<sup>1</sup>Laboratorium für Physikalische Chemie, ETH Zürich, 8093 Zürich, Switzerland

<sup>2</sup>State Key Laboratory of Precision Spectroscopy, East China Normal University, Shanghai, China

\* These authors contributed equally to this work.

† e-mail: hwoerner@ethz.ch

### Attosecond size-resolved cluster spectroscopy

#### Water-Cluster Generation setup

The experimental setup and the water-cluster source are illustrated in Fig. B1. The neutral water clusters[167, 168] were formed in a continuous supersonic expansion into vacuum with a water-vapor pressure of 0.3 MPa through a 50  $\mu\text{m}$  nozzle orifice and passed through two conical skimmers (Beam Dynamics) located 10 mm and 30 mm downstream with a diameter of 200  $\mu\text{m}$  and 1 mm, respectively. The

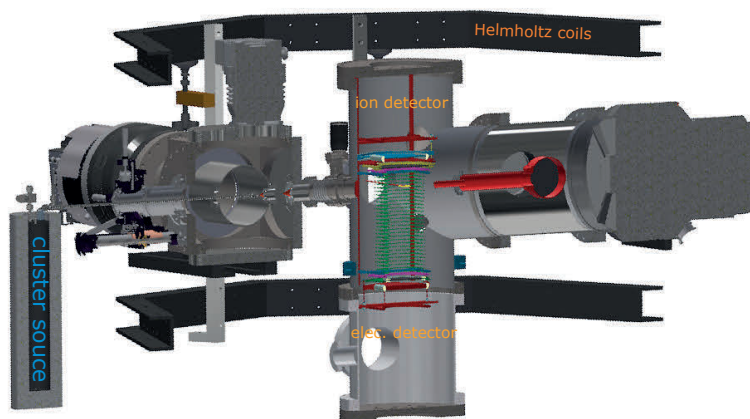


**Figure B1: Drawing of the coincidence spectrometer and water-cluster source.** The water-cluster source is coupled to the electron-ion coincidence spectrometer through a two-stage differential pumping system with a molecular-beam dump on the opposite side. The time-of-flight axis of the coincidence spectrometer was perpendicular to the supersonic beam. Homogeneous electric fields were created by a stack of electrodes that guide the motion of the ions and electrons to the MCP detectors. The pair of Helmholtz coils provided the required magnetic fields.

liquid water was maintained at 408 K to give rise to a sufficient vapor pressure in a container of 0.7 L to support a stable water-cluster beam for a duration of 120 hours. The water-cluster source was coupled to the COLTRIMS via two differential pumping stages. To maintain the ultrahigh vacuum in the main reaction chamber, a differentially pumped beam dump captured the molecular beam after the interaction region.

### Water-Cluster Fragmentation Dynamics and Abundance

The fragmentation dynamics of water clusters upon photoionization consists out of a rapid proton transfer, followed by the loss of a single neutral OH unit [146–154, 225, 226].

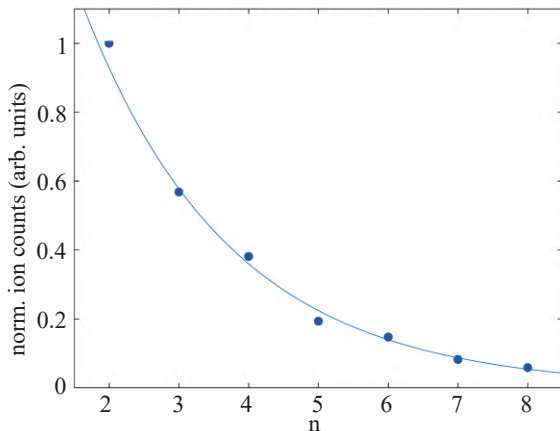
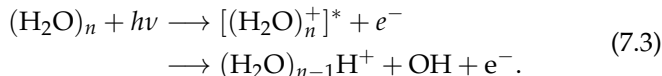
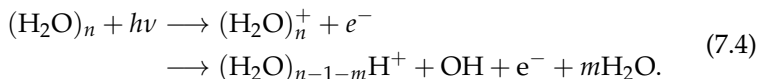


**Figure B2: Measured intensity of the protonated water-cluster ions  $(\text{H}_2\text{O})_n\text{H}^+$  in our cluster beam.** The data was normalized with respect to  $n=2$ , i.e.  $(\text{H}_2\text{O})_2\text{H}^+$ . The blue solid line is an exponential fit to the experimental data (blue dots).



This pathway dominates the fragmentation of water clusters up to  $n=15$  [146, 148, 152]. For larger clusters the subsequent loss of additional water molecules becomes relevant following the reaction



However, in photoionization experiments with 12.5 eV [152] and 26.5 eV [146], the onset of  $\text{H}_2\text{O}$  molecule loss has only been observed for clusters with  $n \geq 5$ , with the decay fraction for  $n=5$  and  $n=6$  still well below 10%. Figure B2 shows the measured intensity distribution of the protonated water clusters  $(\text{H}_2\text{O})_n\text{H}^+$  of our cluster source. The vanishing intensity for larger clusters allows us to exclude the possibility of fragmentation dynamics from large clusters.

## Water-Cluster Structure

This section summarizes the isomer structures of small water clusters and their population distribution within the temperature range of our cluster beam. The structures of small water clusters and their respective energies have been studied extensively in recent years [156–163, 227]. Table S1 shows the electronic binding energies  $\Delta E_e$  of the clusters with respect to the (non-interacting) monomers and the enthalpies of formation  $\Delta H(0K)$  at 0 K for different isomers as calculated by Temelso et al. [157]. For an estimated internal temperature of the water clusters of 150 K there is 0.3 kcal/mol of thermal energy available. Therefore, we only take into account the isomeric structures that lie within 0.3 kcal/mol in enthalpy of the energetically most stable isomer. The resulting isomers are identified with bold font in Table B1.

## Attosecond Coincidence Interferometry

In our experiments, photoionization of water clusters was induced by single-XUV-photon absorption, yielding a main-band (MB) photoelectron band at a kinetic energy  $eKE = E_{XUV} - I_p$ , as shown in Fig. B3. The synchronized IR field induced two distinct quantum paths from adjacent main bands to the same final side-band (SB) state by absorption or stimulated emission of one IR photon. The interference between these two quantum paths gave rise to the typical SB intensity oscillations with half the IR period as a function of the APT-IR pump-probe delay. To achieve attosecond temporal stability, a frequency-stabilized laser beam (He-Ne continuum reference laser,  $\lambda = 632.8\text{nm}$ ) was coupled into the XUV-APT and IR Mach-Zehnder interferometer [228–230], resulting in a time jitter of  $\sim 40$  as, as shown in Fig. B4.

The photoionization time delays of water clusters are determined from the intensity oscillations of the SB peaks defined as

$$A_q(\tau) = A \cos(2\omega(\tau - \tau_q)) + B = A \cos(2\omega(\tau - \tau_q^{\text{XUV}} - \tau_q^{\text{sys}})) + B, \quad (7.5)$$

$(\text{H}_2\text{O})_n$	$\Delta E_e$	$\Delta H(0K)$
<b>2-(C<sub>s</sub>)</b>	-5.03	-3.14
<b>3-UUD</b>	-15.70	-10.63
<b>3-UUU(C<sub>3</sub>)</b>	-15.08	-10.40
<b>4-(S<sub>4</sub>)</b>	-27.43	-19.74
4-(C <sub>i</sub> )	-26.58	-19.08
4-PY	-23.88	-16.56
<b>5-CYC</b>	-36.01	-26.29
5-FR-B	-34.87	-25.11
5-CA-C	-34.69	-24.70
5-CA-A	-34.54	-24.53
5-CA-B	-33.82	-23.83
5-FR-C	-32.44	-22.87
5-FR-A	-33.13	-23.23
<b>6-PR</b>	-46.14	-33.16
<b>6-CA</b>	-45.93	-33.14
6-BK-1	-45.51	-33.11
6-BK-2	-45.14	-32.74
6-CC(S <sub>6</sub> )	-44.60	-32.76
6-BAG	-44.59	-32.36
6-CB-1(C <sub>2</sub> )	-43.57	-31.91
6-CB-2(C <sub>2</sub> )	-43.51	-32.03

**Table B1:** Binding energy and enthalpy of formation of different water cluster isomers given in kcal/mol. The values were taken from Ref. [157].

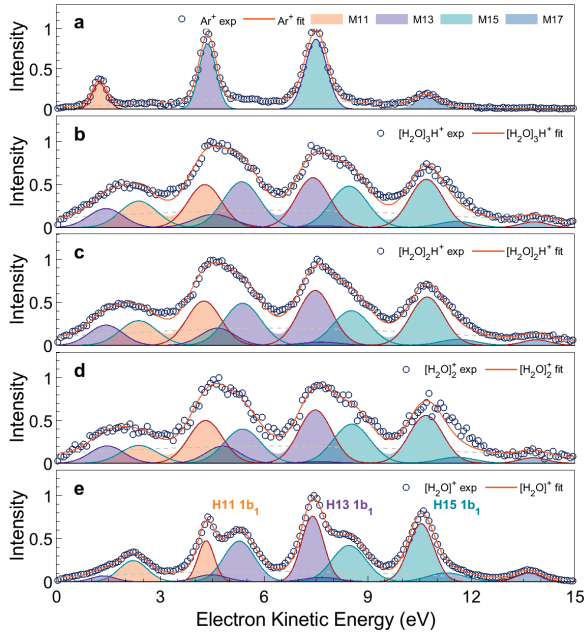


**Figure B3: XUV-only photoelectron spectra of water clusters and argon atoms.** a argon, b  $[\text{H}_2\text{O}]_3\text{H}^+$ , c  $[\text{H}_2\text{O}]_2\text{H}^+$ , d  $[\text{H}_2\text{O}]_2^+$ , e  $[\text{H}_2\text{O}]^+$ . The XUV-APT included the high-harmonic orders from 11 to 17.

where  $\omega$  is the angular frequency of the IR field,  $\tau_q^{\text{XUV}}$  represents the emission-time difference of harmonics  $q + 1$  and  $q - 1$ , i.e. it reflects the attochirp of the XUV-APT [231] and  $\tau_q^{\text{sys}}$  is the system-specific photoionization time delay [39, 40, 98, 100, 121, 137].

### Phase Reconstruction

Compared to atomic systems, the measurement of molecular photoionization time delays typically faces the challenge of spectral overlap [137, 155]. This is because the XUV-APT ionizes electrons out of several possible orbitals, which leads to spectral overlap be-



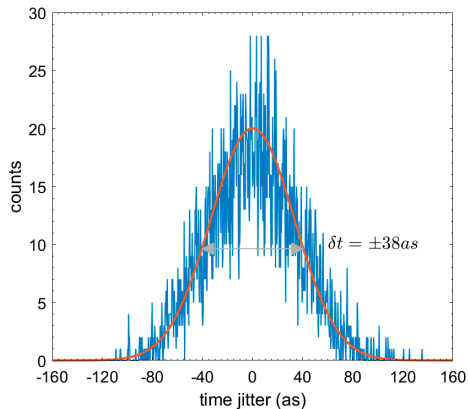


**Figure B4: Delay stability of the attosecond pump-probe interferometer.** The time jitter of the phase-locked Mach-Zehnder interferometer amounted to  $\pm 38$ as.

tween the photoelectron MB spectra created by different harmonic orders and the SB spectra. Figure B5 shows the attosecond photoelectron spectra recorded in coincidence with different water-cluster fragments, ranging from the dimer to the protonated pentamer. To extract the photoionization time delays from spectrally overlapping attosecond photoelectron spectra, we used the complex-valued principal components analysis as described in detail in [155], which has also been successfully used in our recent work on liquid water [120]. In the first step, the XUV-only photoelectron spectrum is fitted with a set of Gaussians, as shown in Fig. B3. In a second step, we fitted additional Gaussians to reproduce the XUV+IR photoelectron spectrum. Next, a Fast-Fourier Transformation (FFT) was done line by line on the attosecond photoelectron spectra (Fig. B5) along the time-delay axis and the resulting band in the complex-valued FFT at the  $2\omega$  angular frequency was fitted by multiplying each Gaussian component obtained in the XUV+IR fit with a complex amplitude  $e^{z_j}$

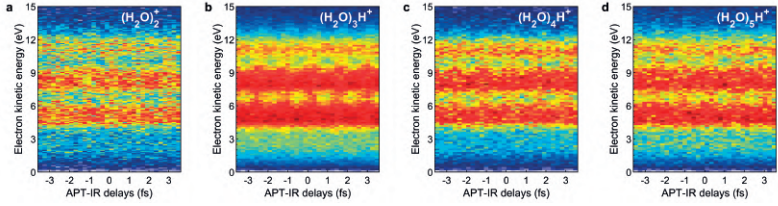


**Figure B5: Attosecond photoelectron spectra for different sized water clusters.** **a**, Attosecond photoelectron spectra coincident with the unprotonated water dimer cation,  $(\text{H}_2\text{O})_2^+$ . **b-d**, Same as **a** but for **b**  $(\text{H}_2\text{O})_3\text{H}^+$ , **c**  $(\text{H}_2\text{O})_4\text{H}^+$ , **d**  $(\text{H}_2\text{O})_5\text{H}^+$ .

$$I_{fit}(E) = \sum_j p_j(E) e^{z_j} = \sum_j \underbrace{e^{a_j} p_j(E)}_{A_j(E)} e^{ib_j}, \quad (7.6)$$

where  $p_j(E)$  is the Gaussian fit for photoelectron band  $j$  (see Fig. B3). This complex number  $z_j = a_j + ib_j$  simultaneously accounts for the side-band specific delay  $\tau_j = -b_j/(2\omega)$  and a finite modulation contrast when  $|e^{a_j}| < 1$ . The numerical robustness of the obtained phase shifts of SB12 and SB14 is illustrated in Fig. B6, obtained by randomly varying the initial guesses of the  $1b_1$  binding energies over a range of 0.2 eV. These results showed that the determination of the phase shifts was robust with respect to the initial guesses and demonstrated the absence of any systematic correlation between these two quantities.

To exclude any major contributions due to vibrational effects in the measured photoionization time delays, we additionally performed the attosecond size-resolved measurement with pure  $\text{D}_2\text{O}$  clusters (Sigma-Aldrich, 99.9 atom % D). Figure B7 shows the measured mass spectrum of ionized  $\text{D}_2\text{O}$  clusters, under similar conditions as the spectrum shown in Fig. B1c and 1d in the main text. The ion mass spectra for the different isotopes look very similar, as the fragmentation pathways are the same [232, 233]. Figure B8 shows the size-resolved attosecond photoelectron spectra and their numerical complex-fitting results for the heavy water clusters.

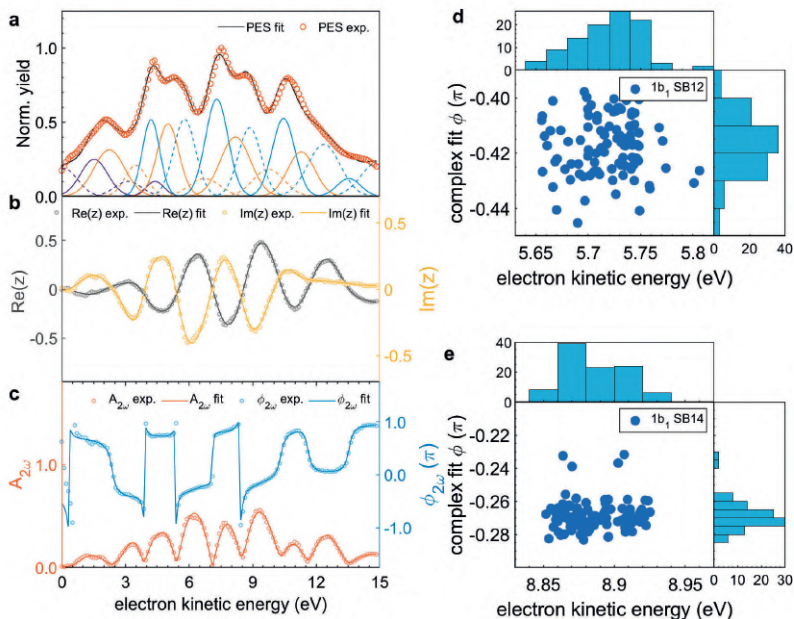


**Figure B6: Numerical stability of the phase reconstruction** **a**, Measured (red circles) and fitted (black line) photoelectron spectrum, in coincidence with  $\text{H}_2\text{O}^+$  and in the presence of the XUV-APT + IR field with the XUV single-photon contributed main bands (solid lines) and sidebands (dashed lines) corresponding to the  $1b_1$  (blue),  $3a_1$  (orange) and  $1b_2$  (purple) bands. **b**, Real (black) and imaginary (yellow) components of the  $2\omega$  frequency band in the Fourier transform of the RABBIT photoelectron spectrum of water monomers. The circles represent the data points and the full lines represent the complex fit. **c**, Same as **b**, showing the amplitude and phase of the  $2\omega$  frequency band of the Fourier transform. **d**, Retrieved SB12 phase of  $1b_1$  band as a function of the initial guess of the electron-kinetic energy. The upper and right-hand panels show the projected electron-kinetic-energy and phase distributions. **e**, Same analysis as in **d** for the phase of SB14

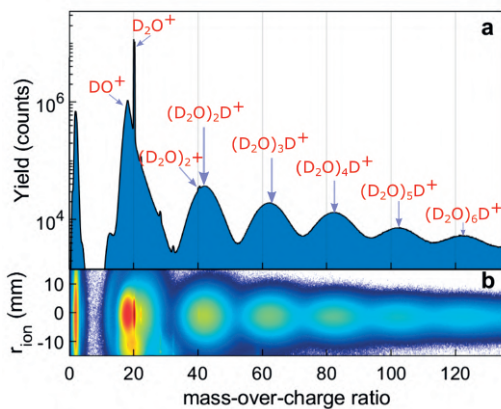


**Figure B7: Mass spectrum of  $\text{D}_2\text{O}$  clusters.** **a**, Mass spectrum of the cluster beam photoionized by an APT as a function of the mass-over-charge (MOC) ratio. **b** Two-dimensional MOC spectrum of water cluster species as a function of position on the ion detector.

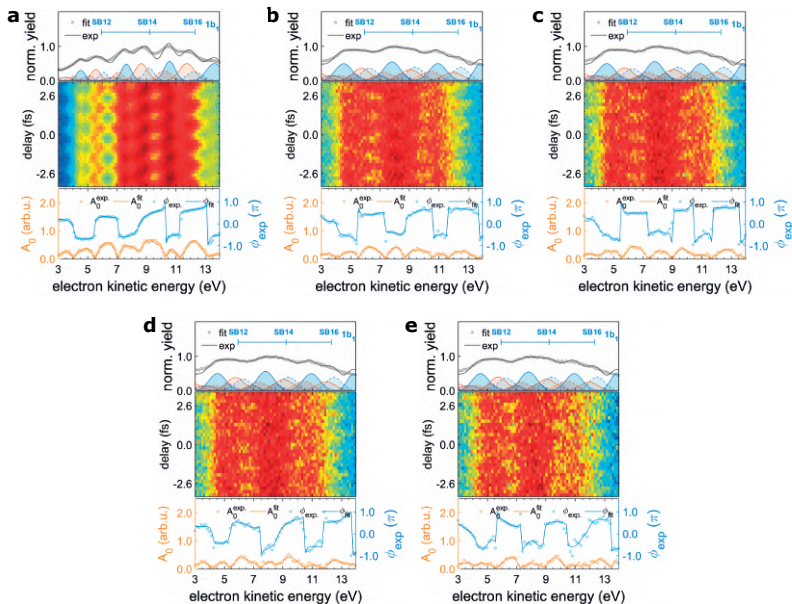


**Figure B8: Attosecond photoelectron spectroscopy of size-selected  $D_2O$  clusters.** Attosecond photoelectron spectra created by overlapping XUV-APT and IR pulses and detected in coincidence with a  $D_2O^+$ , **b**  $(D_2O)_2D^+$ , **c**  $(D_2O)_3D^+$ , **d**  $(D_2O)_4D^+$ , **e**  $(D_2O)_5D^+$ , respectively. The spectrum shown in upper panel is integrated over the APT-IR delay, the middle panel shows the RABBITT trace, and the bottom panel displays the Fourier transforms at  $2\omega$  of the attosecond photoelectron spectra, shown in terms of their modulation amplitude (orange color) and phase (blue color). The experimental data and the fitted curves are shown as open circles and solid lines, respectively.

## Calculations

### Calculations of photoionization matrix elements and cross sections

To describe the photoionization dynamics of an  $N$ -electron molecule or cluster, we employed a quantum-scattering calculation based on the iterative Schwinger variational principle [234]. In this approach, we performed a single-center partial-wave decomposition of the initial electronic state,  $\Psi_i = \sum_{\ell m} R_{n\ell}(r) Y_{\ell m}(\hat{r})$ , which was constructed from an anti-symmetrized product of the  $n = N/2$  occupied orbitals, as implemented in *ePolyScat* [206, 207]. The final-state wave function and the scattering potential were also expanded into partial waves.

The photoionization dipole matrix elements in the length gauge for linearly polarized radiation are given by

$$I_{i,f} = \left\langle \Psi_{f,\kappa}^{(-)} \left| \mathbf{r} \cdot \hat{\mathbf{E}}_{XUV} \right| \Psi_i \right\rangle = \sqrt{\frac{4\pi}{3\kappa}} \sum_{\ell m v} I_{\ell m v} Y_{\ell m}(\hat{\mathbf{k}}) Y_{1v}^*(\hat{\mathbf{n}}) \quad (7.7)$$

where  $\mathbf{r}$  is the position operator,  $Y_{\ell m}$  are the spherical harmonics,  $Y_{1,v=0,\pm 1}$  describes the orientation  $\hat{\mathbf{E}}_{XUV}$  of the XUV polarization in the molecular frame,  $\hat{\mathbf{k}}$  is the asymptotic momentum of the outgoing photoelectron wavepacket,  $|\Psi_{f,\kappa}^{(-)}\rangle$  denotes the observed final-state wave function, and  $I_{\ell m v} = \sqrt{\frac{2}{\pi}} (-i)^\ell \left\langle \Psi_{f,\kappa\ell m}^{(-)} \left| \mathbf{r}_v \right| \Psi_i \right\rangle$  is the partial-wave matrix element. The photoionization cross sections integrated over target-orientation and photoelectron-emission angles are given by

$$\sigma = \frac{4\pi^2 E}{3c} \sum |I_{i,f}|^2, \quad (7.8)$$

where  $E$  is the photon energy.

### Calculations of photoionization time delays

As introduced by Wigner and Smith [39, 40], the energy derivative of the scattering phase is associated with a time delay in scattering. In photoionization, this definition leads to a delay of the outgoing

photoelectron wavepacket. The case of atoms and molecules have been treated in Refs. [121] and [98], respectively. The photoionization time delay is defined as the energy derivative of the complex photoionization amplitude  $f(\epsilon)$

$$\tau = \frac{d}{d\epsilon} \text{Arg}(f(\epsilon)) = \text{Im} \left\{ \frac{1}{f(\epsilon)} \frac{df}{d\epsilon} \right\}. \quad (7.9)$$

In the picture of partial-wave decomposition, the outgoing wavepacket is expressed as a coherent sum over partial waves,  $\Psi = \sum_{lm} \psi_{lm}$ , where each component is defined by the quantum numbers  $(l, m)$ , i.e. the electronic orbital angular momentum and its projection onto a given quantization axis, and each  $(l, m)$  defines a partial-wave scattering channel.

In contrast to the spherical nature of the scattering potential in the atomic case, a molecule or cluster has a highly anisotropic potential, which requires many partial waves in the single-center expansion. In our calculations we have typically used  $l_{\text{max}} = 50$ .

The photoionization time delay in the molecular frame depends on the photon energy  $E$ , the final momentum  $\hat{\kappa}$  and the polarization direction  $\hat{E}_{XUV}$  of the ionizing radiation. It can be defined as:

$$\tau_{\omega}^{MF}(E, \hat{\kappa}, \hat{E}_{XUV}) = \hbar \frac{\partial}{\partial E} [\text{Arg}(\langle \Psi_{f, \kappa}^{(-)} | \mathbf{r} \cdot \hat{E}_{XUV} | \Psi_i \rangle)]. \quad (7.10)$$

Figure B9 illustrates the photoionization delay (left) and the differential photoionization cross section (right) for the case of the water dimer as a function of the emission angles  $(\theta, \phi)$  in the molecular frame.

Although the three-dimensional momentum is accessible in our coincidence setup, we averaged over all molecular orientations and the emission angle  $\hat{\kappa}$  of the photoelectron in the off-line analysis due to the limited water-cluster signal. Hence, the ionization time delay  $\tau_{\omega}(E)$  is obtained by integrating over all molecular orientations (defined by the set of Euler angles  $\hat{R}_{\gamma}$ ) and photoelectron-emission

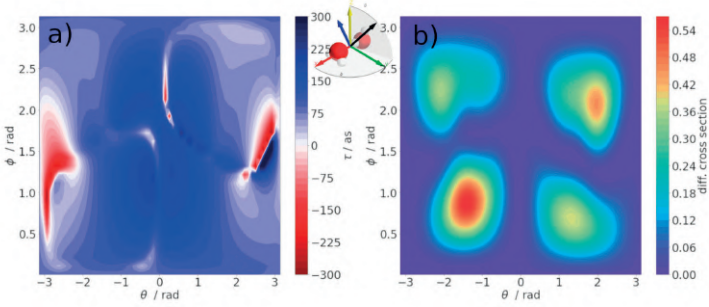


**Figure B9: Example of one-photon (Wigner) time delay in the molecular frame (a) and differential photoionization cross section (b) for HOMO of the  $(\text{H}_2\text{O})_2$  system and the light polarisation direction (blue arrow) indicated in the inset, as a function of photoelectron ejection directions (black arrow defined by  $\theta$  and  $\phi$  angles in molecular frame).**

directions  $\hat{\mathbf{k}}$ , as described in Ref. [98].

$$\tau_\omega(E) = \frac{1}{8\pi^2} \int d\hat{R}_\gamma \int d\hat{\mathbf{k}} A(E, \hat{R}_\gamma, \hat{\mathbf{k}}) \tau_\omega^{\text{MF}}(E, \hat{R}_\gamma, \hat{\mathbf{k}})$$

where

$$A(E, \hat{R}_\gamma, \hat{\mathbf{k}}) = \frac{|\sum_{lm\mu} I_{lm\mu} Y_{lm}(\hat{\mathbf{k}}) D_{\mu m p}^{(1)}(\hat{R}_\gamma)|^2}{\sum_{lm\mu} |I_{lm\mu}|^2},$$

both quantities being shown in Fig. B9.

Instead of directly measuring the one-photon (Wigner) delays  $\tau_\omega(E)$ , a RABBIT experiment accesses a closely related quantity, resulting from two-photon (XUV+IR) transitions. The molecular part of the two-photon time delay (ignoring cc-delay) in the molecular frame is defined via the total transition amplitude  $f_{\text{mol}}^{\text{MF}}$  given by

$$f_{\text{mol}}^{\text{MF}}(2q, \hat{\mathbf{k}}, \hat{R}_\gamma) = \sum_{LML'M'} Y_{L'M'}^*(\hat{\mathbf{k}}) Y_{LM}(\hat{\mathbf{k}}) b_{L'M';(2q-1)}^*(\hat{R}_\gamma) b_{LM;(2q+1)}(\hat{R}_\gamma),$$



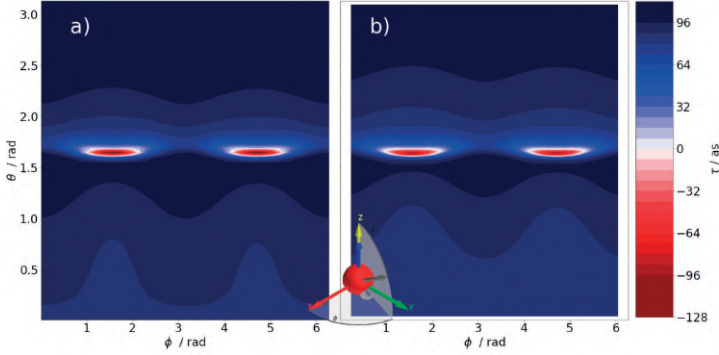


**Figure B10: One-photon (Wigner) time delay a) and two-photon (XUV+IR) time delay b) in the molecular frame as a function of electron-ejection angles ( $\theta$  and  $\phi$ ) in the molecular frame, when the light polarisation (XUV and IR, blue arrow) is aligned along the z-axis, as shown in the inset. All results are time delays calculated for the H<sub>2</sub>O monomer, HOMO orbital and photoionization to SB12.**

where transition amplitudes from IR emission/absorption  $b$  have been defined in Ref. [98]. We get the laboratory-frame  $\tau_{mol}(2q)$  time delay by coherently integrating  $f_{mol}^{MF}$  over all molecular orientations (defined by the set of Euler angles  $\hat{R}_\gamma$ ) and photoelectron-emission directions  $\hat{\mathbf{k}}$  and calculating the phase of the total transition amplitude, i.e.

$$\tau_{mol}(2q) = \frac{1}{2\omega} \arg \left[ \int d\hat{R}_\gamma \int d\hat{\mathbf{k}} f_{mol}^{MF}(2q, \hat{\mathbf{k}}, \hat{R}_\gamma) \right].$$

We can also calculate the molecular frame time delay from  $f_{mol}^{MF}(2q, \hat{\mathbf{k}}, \hat{R}_\gamma)$  directly, and then proceed as in the one-photon case by cross-section-weighted integration (shown in RHS of Fig. B10, Fig. B11 and Fig. B12). We have verified that the two approaches give the same results.

Figures B10 to B12 compare the molecular-frame one- and two-photon delays of the water clusters. These figures show that the two quantities are very similar in magnitude and display very similar an-

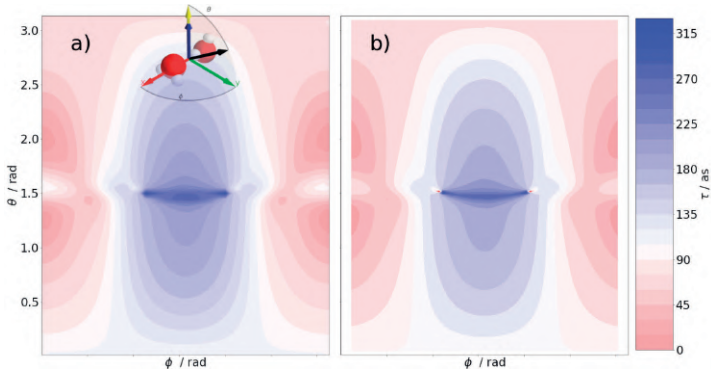


**Figure B11:** Same as Fig. B10 but for  $(\text{H}_2\text{O})_2$  and HOMO orbital.

gle dependencies. This agreement is further quantified in Fig. B13, which directly compares the one- and two-photon delays obtained after full angular averaging over the photoemission and molecular-orientation directions. In most cases, the difference between the delays amount to a few attoseconds only. The largest difference is found in the case of the  $S_4$  isomer of the water tetramer, where the difference amounts to  $\sim 13$  as. Compared to the error bars of the experimental results, even this difference is still negligible.

Based on this close agreement between one- and two-photon delays in water clusters, we have therefore based our discussion in the main text and in the remainder of this document on the one-photon (Wigner) delays.

## Photoionization delays of the $1b_1$ and O-1s ( $1a_1$ ) bands of water clusters

The following set of figures show the complete cluster-size-, isomer- and orbital-resolved one-photon-ionization delays integrated over target orientations and photoemission directions. A subset of these results are shown in Figs. 5.3 and 5.4 of the main text. Figure 5.3 of the main text shows the cross-section-weighted average time delay,

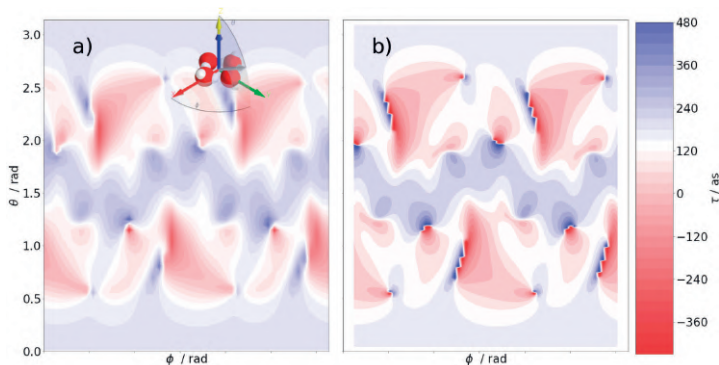


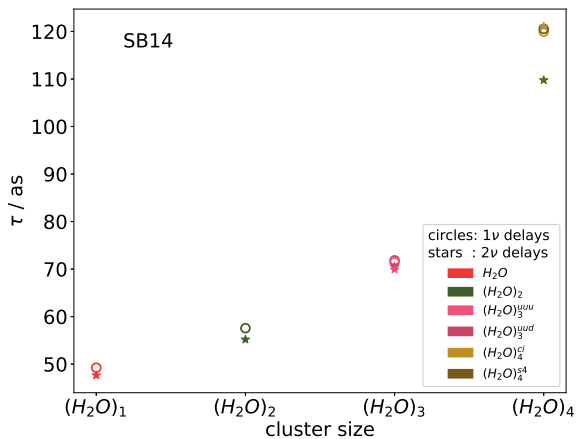
**Figure B12:** Same as Fig. B10 but for  $(\text{H}_2\text{O})_4^{(s_4)}$  and HOMO orbital.

which is defined as follows

$$\tau(E) = \frac{\sum_{i=1}^n \sigma_i(E) \tau_i(E)}{\sum_{i=1}^n \sigma_i(E)}, \quad (7.11)$$

where the sum runs over the  $n$  orbitals of the  $1b_1$  band of  $(\text{H}_2\text{O})_n$ ,  $\sigma_i(E)$  is the photoionization cross section of orbital  $i$  at the photon energy  $E$  and  $\tau_i(E)$  is the corresponding photoionization time delay. This quantity can directly be compared with the experimental results, which do not resolve the individual orbitals of the  $1b_1$  band.

Figure B14 shows the time delays and  $1b_1$ -band orbital densities of the 1-2 most stable water-cluster isomers. A selection of these results is also shown in Figs. 5.3 and 5.4 of the main text. This figure highlights the close relationship between orbital delocalization and time delays. The largest delays are obtained for the tetramer with  $S_4$  symmetry. This is consistent with the perfect orbital delocalization imposed by symmetry. This figure also nicely illustrates the generality of the localization phenomenon for clusters larger than the tetramer: all orbital densities for pentamers to heptamers are typically delocalized over  $\sim 3$  molecules. The delocalization does not augment with increasing cluster size.



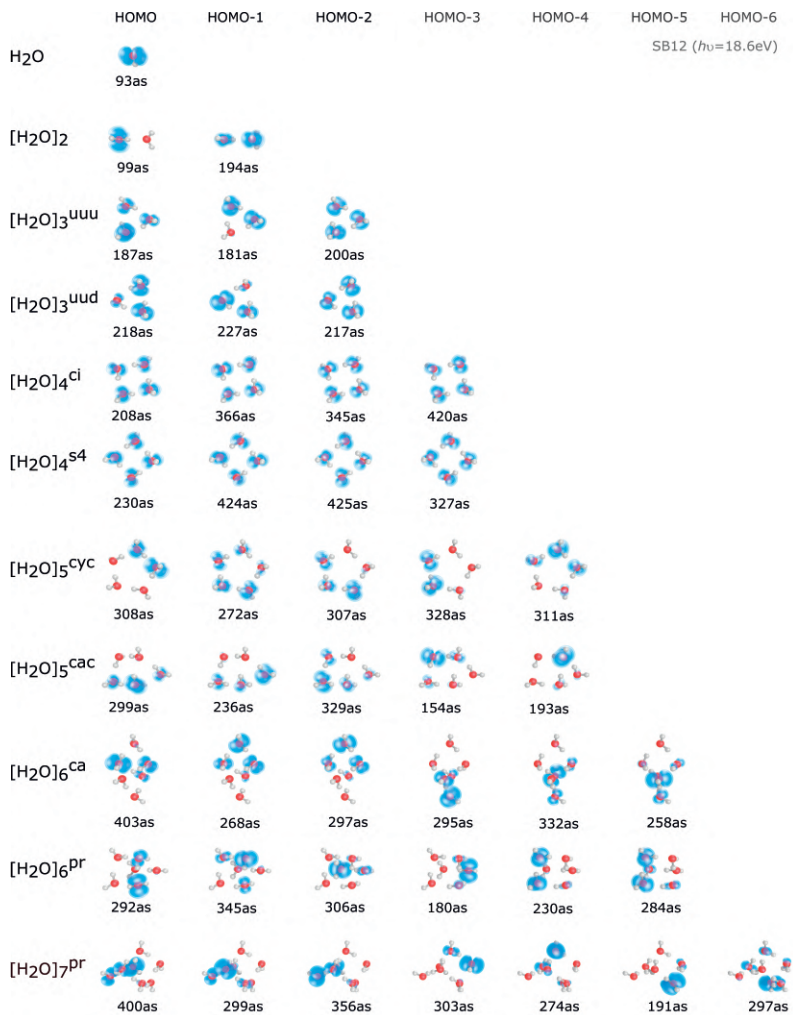
**Figure B13: Comparison of absolute angle- and orientation-averaged one- and two-photon delays** of water clusters in SB14. These results can be directly compared with the (relative) one-photon delays shown in Fig. B3b of the main text.

Figure B15 shows the same results as Fig. B14, but displays the orbital wave functions, instead of the orbital densities. This representation highlights the additional possible role of the orbital sign. Comparing, as an example, HOMO and HOMO-3 of the tetrameric reveals that the "out-of-phase" combination of the 1b<sub>1</sub> molecular-fragment orbital has a much smaller delay (208 as) than the "in-phase" combination (420 as). The same trend can also be seen when comparing the HOMO (230 as) and HOMO-2 (425 as) of the tetramer-s4.

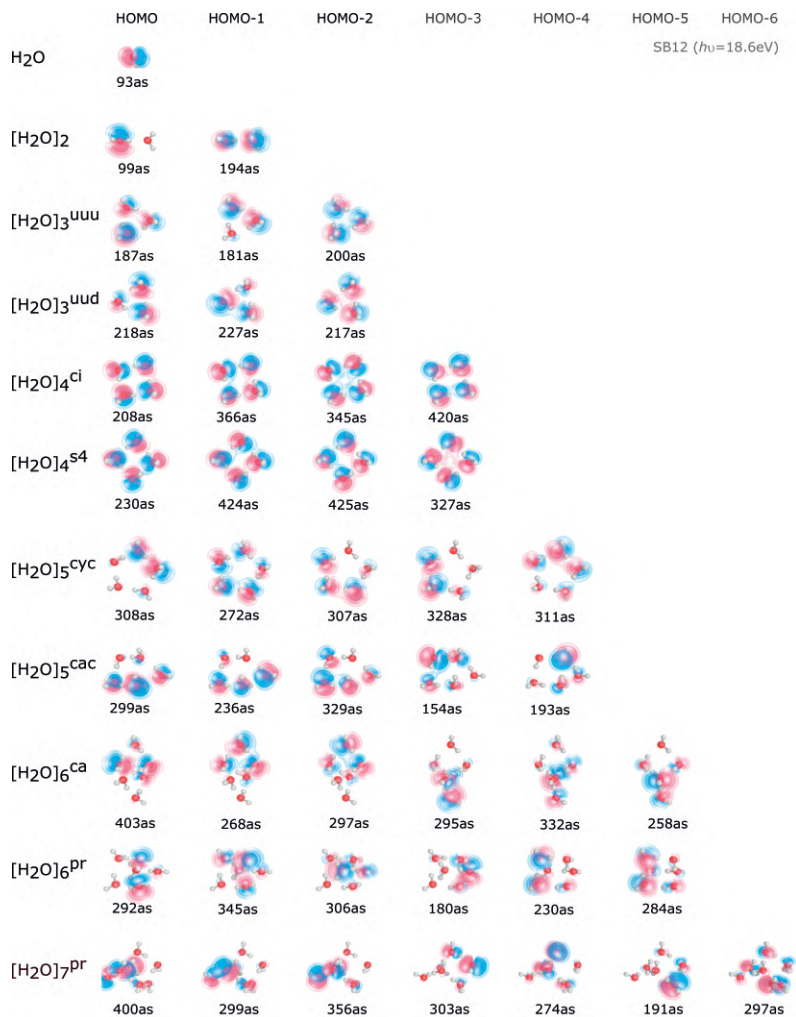
Figures B16 and B17 show the same orbital densities and wave functions as Figs. B14 and B15, but provide the delays for a kinetic energy of 9.1 eV, corresponding to a photon energy of ~21.7 eV, i.e. SB14.

Figure B18 shows the time delays and O-1s (or  $1a_1$ ) orbital densities of the same water-cluster isomers as Figs. B14-B17. A subset of these results is also shown in Figs. 5.3 and 5.4 of the main text. These calculations illustrate the direct relationship between time delay and orbital delocalization even more directly by removing the orbital hybridization effects caused by hydrogen bonding and orbital overlap in the  $1b_1$  band. The orbitals of the tetramer-ci are localized on a single water molecule and display a delay that is identical to the monomer. In contrast, the orbitals of the tetramer-s4 are perfectly delocalized (by symmetry) and all display much larger delays. In the O-1s band, the effect of disorder-induced orbital delocalization is even more striking. For all clusters larger than the tetramer, the orbitals are localized on individual molecules and the delays are close to the monomer delay. These results further confirm the negligible contribution of electron scattering off neutral water molecules to the time delays.

Figure B19 shows the same results as Fig. B18, but displays the orbital wave functions, instead of the orbital densities. In this case, the relationship between time delays and signs of the orbital wave functions appears to be opposite to the  $1b_1$  band. Comparing the HOMO and HOMO-3 of the tetramer-s4, it is the "out-of-phase" combination of the atomic O-1s orbitals that leads to the larger delay (141 as), compared to the "in-phase" combination. However, the less symmetric phase combination of HOMO-2 is associated with the largest delay (185 as). Therefore, we do not find a simple relationship between the signs of the linear combinations of fragment orbitals in clusters and the associated photoionization time delays.



**Figure B14: Orbital-resolved photoionization time delays of SB12 for the 1b<sub>1</sub> band.** Orbital density and photoionization time delays of water clusters using a kinetic energy of 6.0 eV, corresponding to a photon energy of ~18.6 eV.



**Figure B15: Orbital-resolved photoionization time delays of SB12 for the 1b<sub>1</sub> band.** Same as Fig. B14, but showing the orbital wave functions instead of their density.

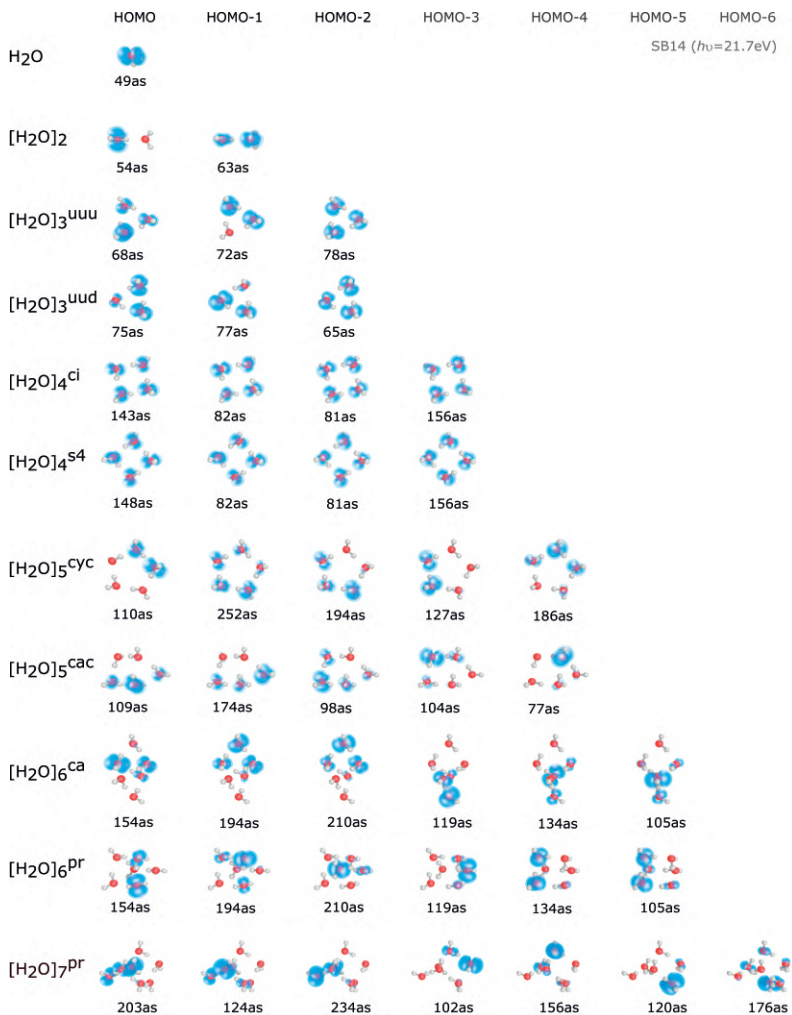


**Figure B16: Orbital-resolved photoionization time delays of SB14 for the 1b<sub>1</sub> band.** Orbital density and photoionization time delays of water clusters using a kinetic energy of 9.1 eV, corresponding to a photon energy of ~21.7 eV.



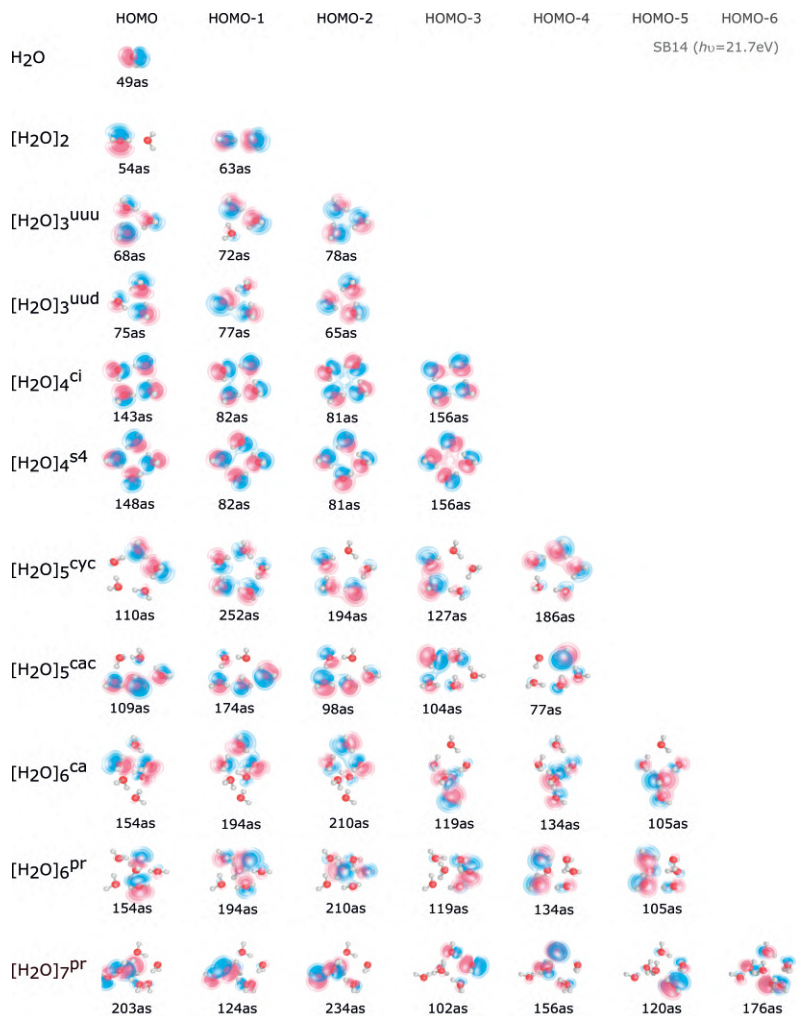


**Figure B17: Orbital-resolved photoionization time delay of SB14 for the 1b<sub>1</sub> band.** Same as Fig. B16, but showing the orbital wave functions instead of their density.

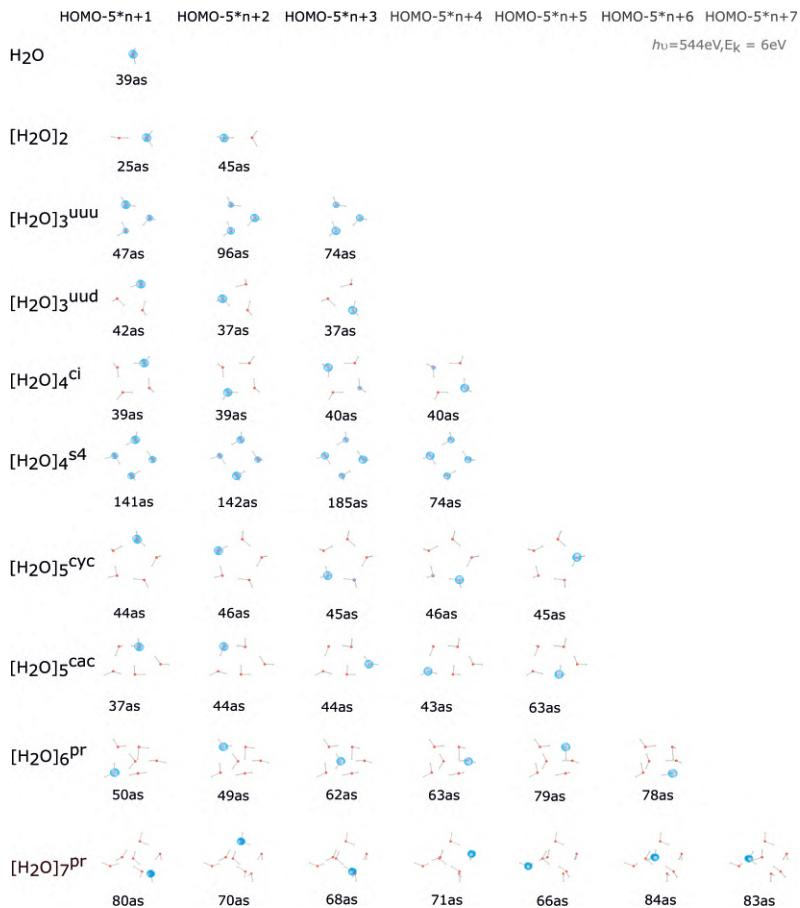


**Figure B18: Orbital-resolved photoionization time delays of the O1s (or  $1a_1$ ) band.** Orbital density and photoionization time delays of water clusters using a kinetic energy of 6.0 eV, corresponding to a photon energy of  $\sim 544$  eV.

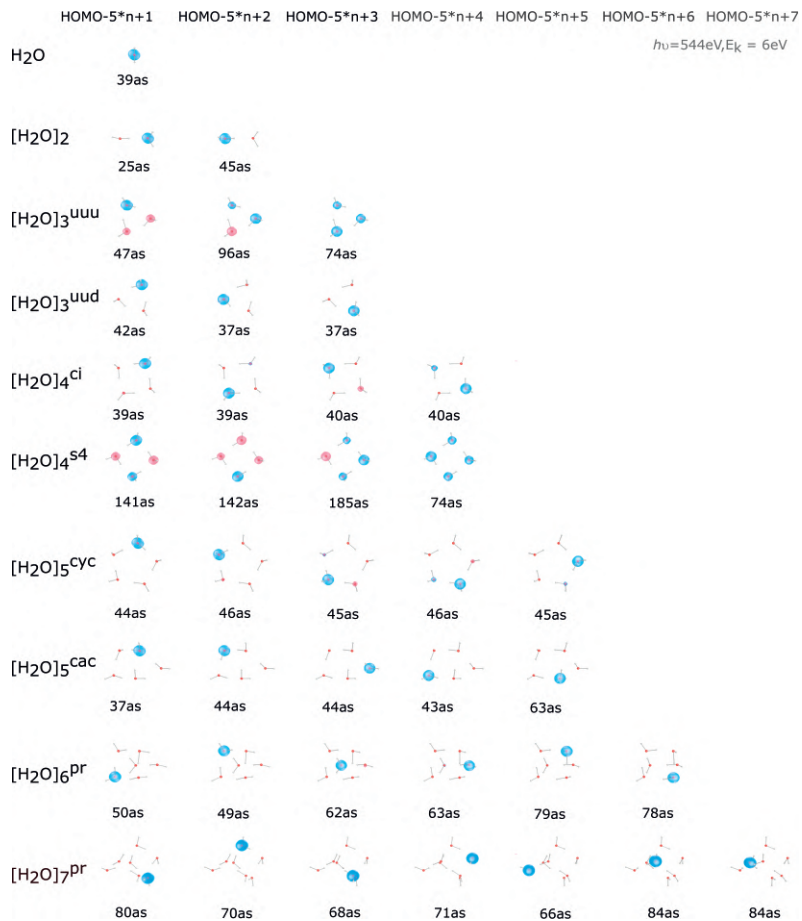


**Figure B19: Orbital-resolved photoionization time delays of the O1s (or 1a<sub>1</sub>) band.** Same as Fig. B18, but showing the orbital wave functions instead of their density.

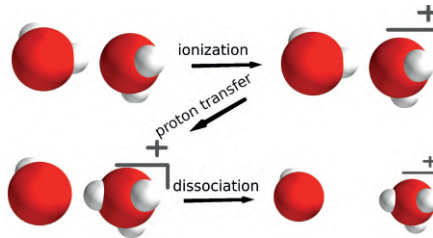


**Figure B20: Illustration of the large amplitude motion (proton transfer) following ionization of water clusters, illustrated for the example of the water dimer.** A similar illustration for the case of the water trimer is shown in Fig. 5.1b of the main text.

## Effects of nuclear motion and resonances on photoionization delays of water clusters

In this section, we briefly discuss the possible role of nuclear motion on photoionization delays of water clusters. Ionization of a water cluster initiates the transfer of a proton from the ionized molecule to its neighbor, as illustrated in Fig. B20. The time scale for proton transfer in ionized water clusters has recently been determined to be  $\sim 30\text{-}40$  fs [132].

To assess the role of nuclear motion on the photoionization time delays, we have calculated the variation of the time delays along the proton-transfer coordinate, as well as the O-O stretch coordinate in the water dimer. Figure B21 shows that the photoionization delays, obtained as a function of these nuclear coordinates vary very little (by  $\pm 3$  as) across the Franck-Condon regions, shown as red-shaded areas. These results support the fixed-nuclei approximation used in the remainder of our work.

We moreover studied the energy dependence of the photoionization time delays with the goal of locating possible shape resonances or Cooper(-like) minima. Previous work has shown that shape resonances usually lead to pronounced local maxima in the photoioniza-

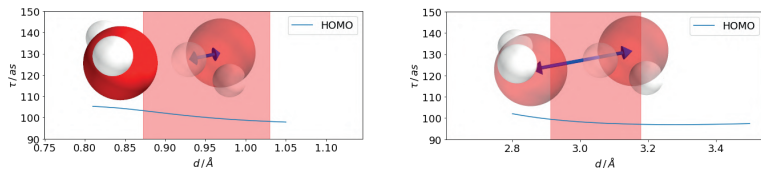


**Figure B21: Photoionization time delays for the HOMO of the water dimer as a function of OH bond length (left) and OO bond length (right) for the case of SB12. The shaded area is the Franck-Condon (FC) region for the vibrational ground state of  $(\text{H}_2\text{O})_2$ .**

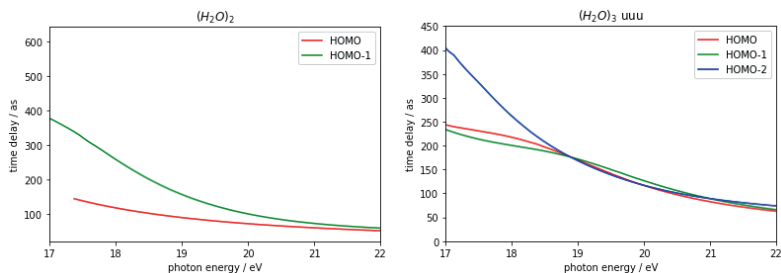


**Figure B22: Orbital-resolved photoionization time delays of individual orbitals of the  $1b_1$  band of the water dimer (left) and trimer (right).**

tion delays [98, 137, 140], whereas Cooper minima give rise to local minima [235]. In the case of water clusters, we find that the variation of the photoionization time delays is strictly monotonic in the energy region of interest in our work, which indicates the absence of shape resonances or Cooper-like minima.

## Benchmarking the quantum-scattering calculations against experimental photoelectron asymmetry parameters

Finally, we present an independent validation of our quantum-scattering calculations by comparison with an independent experimental observable, i.e. the photoelectron asymmetry parameters of

water clusters [226, 227]. Figure B23 compares the measured photoelectron asymmetry parameters to our calculations at the kinetic energies corresponding to SB12 and SB14. The asymmetry parameters were obtained from the output of ePolyScat [206, 207], which uses Eq. (12) in [207] for the calculation of the asymmetry parameters of individual orbitals. We subsequently performed a cross-section-weighted average of the  $\beta$  values of the individual orbitals  $i = 1 - N$  of the  $1b_1$ -band of  $(H_2O)_n$  according to

$$\beta(E) = \frac{\sum_{i=1}^n \sigma_i(E) \beta_i(E)}{\sum_{i=1}^n \sigma_i(E)}, \quad (7.12)$$

The very good agreement between measured asymmetry parameters and those calculated at the electron-kinetic energies corresponding to SB12 and SB14 in our work independently validates the accuracy of our quantum-scattering calculations on water clusters.

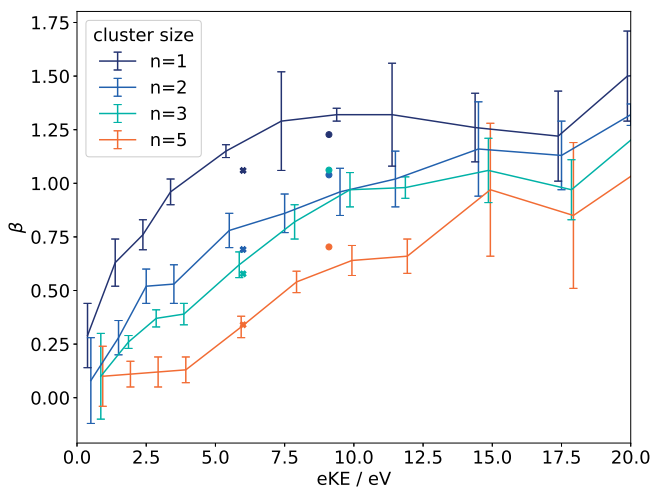


**Figure B23: Asymmetry parameters ( $\beta$ ) for photoionization from the  $1b_1$ -band of water clusters.** Comparison of experimental (lines, Ref. [227]) and calculated (crosses/circles, this work) asymmetry parameters ( $\beta$ ) as a function of the electron kinetic energies.





# Appendix C

**Additional figures for chapter 'Rare Gas Dimers'**

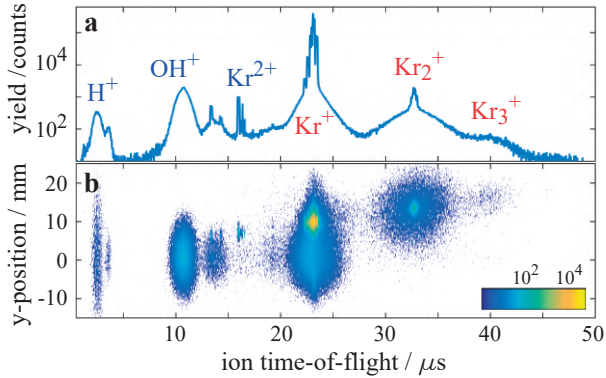


**Figure C1:** (a) Time-of-flight spectrum of the ions from a krypton gas jet with the yield on a logarithmic scale. (b) Same as in (a), but with the y-position on the detector on the y-axis and the yield represented by a logarithmic false color scale. The y-direction in the laboratory frame, corresponds to the propagation direction of the gas jet. Note that the isotopic distribution of krypton is  $^{78}\text{Kr}$ : 0.36%,  $^{80}\text{Kr}$ : 2.29%,  $^{82}\text{Kr}$ : 11.59%,  $^{83}\text{Kr}$ : 11.50%,  $^{84}\text{Kr}$ : 56.99% and  $^{86}\text{Kr}$ : 17.28% and all isotopes are observed.

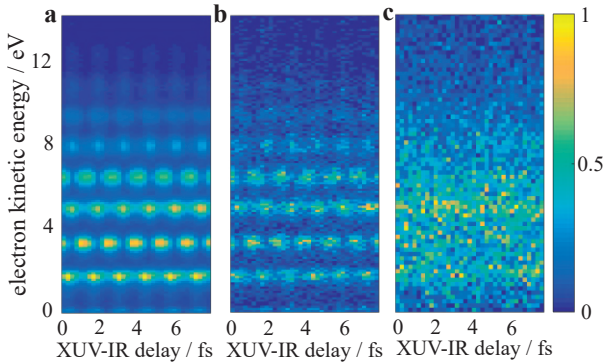


**Figure C2:** RABBIT spectrograms for electrons in coincidence with (a)  $\text{Ne}^+$ , (b)  $\text{Ne}_2^+$  and (c)  $(\text{Ne}^+)_{\text{frag}}$ , from a single experimental data set. For (a) and (b) the electron emission angle is  $\theta_{\text{Lab}} = 0 - 25^\circ$  and  $\theta_{\text{Lab}} = 155 - 180^\circ$  and for (c)  $\theta_{\text{Mol}} = 0 - 45^\circ$ , where  $\theta_{\text{Lab}}$  and  $\theta_{\text{Mol}}$  represent the polar angle in the laboratory and molecular frame, respectively. Counts are normalized and shown in false color. The sidebands 16 and 18 are at 3.2 eV and 6.3 eV, respectively.

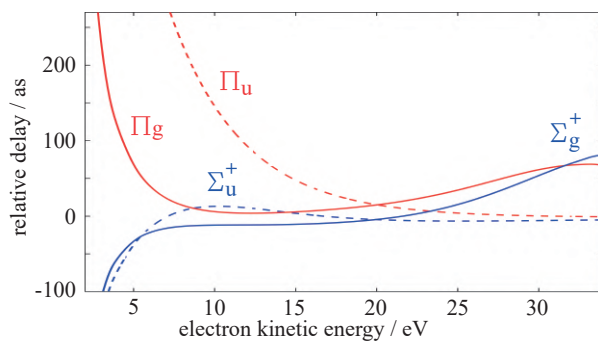


**Figure C3:** Orbital-resolved one-photon ionization delays of  $\text{Ne}_2$  referenced to Ne as a function of electron kinetic energy. Sigma states are shown in blue, Pi states in red, gerade parity with a solid line and ungerade parity with a dashed line.

---

# Author Contributions

In this chapter the contributions of Saijoscha Heck to the different journal publications, printed in this thesis, are listed.

## **Attosecond Interferometry of Shape Resonances in the Recoil Frame of CF<sub>4</sub>**

*Saijoscha Heck,<sup>1</sup> Denitsa Baykusheva,<sup>2†</sup> Meng Han,<sup>1</sup> Jia-Bao Ji,<sup>1</sup> Conaill Perry,<sup>1</sup> Xiaochun Gong<sup>1,3</sup> and Hans Jakob Wörner<sup>1†</sup>*

Science Advances (2021), in press.

- Proposal of the study
- Lead of the study
- Conduction and analysis of the experiment
- Main contribution to the manuscript
- Major contribution to building the experimental setup.

---

## **Attosecond spectroscopy of size-resolved water clusters**

*X. Gong<sup>1,2,\*</sup>, S. Heck<sup>1,\*</sup>, D. Jelovina<sup>1</sup>, C. Perry<sup>1</sup>, K. Zinchenko<sup>1</sup>, H. J. Wörner<sup>1,†</sup>*

ArXiv (2021), under review in Nature.

- Major contribution to conducting the experiments
- Major contribution to building the experimental Setup
- Co-analysis of the experimental data
- Contribution to the manuscript.



# References

1. Potter, M. C., Wyble, B., Hagmann, C. E. & McCourt, E. S. Detecting meaning in RSVP at 13 ms per picture. *Attention, Perception, & Psychophysics* **76**, 270 (2014).
2. Krehl, P & Engemann, S. August Toepler — The first who visualized shock waves. *Shock Waves* **5**, 1 (1995).
3. Krausz, F. & Ivanov, M. Attosecond physics. *Reviews of Modern Physics* **81**, 163 (2009).
4. DeMaria, A., Glenn, W., Brienza, M. & Mack, M. Picosecond laser pulses. *Proceedings of the IEEE* **57**, 2 (1969).
5. Ippen, E. P. & Shank, C. V. Dynamic spectroscopy and subpicosecond pulse compression. *Applied Physics Letters* **27**, 488 (1975).
6. Potter, E. D., Herek, J. L., Pedersen, S., Liu, Q. & Zewail, A. H. Femtosecond laser control of a chemical reaction. *Nature* **355**, 66 (1992).
7. Dantus, M., Rosker, M. J. & Zewail, A. H. Real-time femtosecond probing of “transition states” in chemical reactions. *The Journal of Chemical Physics* **87**, 2395 (1987).
8. Zewail, A. H. Laser Femtochemistry. *Science* **242**, 1645 (1988).
9. Rosker, M. J., Dantus, M. & Zewail, A. H. Femtosecond real-time probing of reactions. I. The technique. *The Journal of Chemical Physics* **89**, 6113 (1988).
10. Paul, P. M., Toma, E. S., Breger, P., Mullot, G., Augé, F., Balcou, P., Muller, H. G. & Agostini, P. Observation of a train of attosecond pulses from high harmonic generation. *Science* **292**, 1689 (2001).
11. Hentschel, M., Kienberger, R., Spielmann, C., Reider, G. A., Milosevic, N., Brabec, T., Corkum, P., Heinzmann, U., Drescher, M. & Krausz, F. Attosecond metrology. *Nature* **414**, 509 (2001).

12. Drescher, M, Hentschel, M, Kienberger, R, Uiberacker, M, Yakovlev, V, Scrinzi, A, Westerwalbesloh, T., Kleineberg, U, Heinzmann, U. & Krausz, F. Time-resolved atomic inner-shell spectroscopy. *Nature* **419**, 803 (2002).
13. Baltuška, A., Udem, T., Uiberacker, M., Hentschel, M., Goulielmakis, E., Gohle, C., Holzwarth, R., Yakovlev, V. S., Scrinzi, A., Hänsch, T. W. & Krausz, F. Attosecond control of electronic processes by intense light fields. *Nature* **421**, 611 (2003).
14. Cavalieri, A. L., Müller, N., Uphues, T., Yakovlev, V. S., Baltuška, A., Horvath, B., Schmidt, B., Blümel, L., Holzwarth, R., Hendel, S., Drescher, M., Kleineberg, U., Echenique, P. M., Kienberger, R., Krausz, F. & Heinzmann, U. Attosecond spectroscopy in condensed matter. *Nature* **449**, 1029 (2007).
15. Schultze, M., Fiess, M., Karpowicz, N., Gagnon, J., Korbman, M., Hofstetter, M., Neppel, S., Cavalieri, A. L., Komninos, Y., Mercouris, T., Nicolaides, C. A., Pazourek, R., Nagele, S., Feist, J., Burgdorfer, J., Azzeer, A. M., Ernstorfer, R., Kienberger, R., Kleineberg, U., Goulielmakis, E., Krausz, F. & Yakovlev, V. S. Delay in Photoemission. *Science* **328**, 1658 (2010).
16. Jordan, I., Huppert, M., Pabst, S., Kheifets, A. S., Baykusheva, D. & Wörner, H. J. Spin-orbit delays in photoemission. *Physical Review A* **95**, 1 (2017).
17. Fuchs, J., Douguet, N., Donsa, S., Martin, F., Burgdörfer, J., Argenti, L., Cattaneo, L. & Keller, U. Time delays from one-photon transitions in the continuum. *Optica* **7**, 154 (2020).
18. Heuser, S., Galán, Á. J., Cirelli, C., Marante, C., Sabbar, M., Boge, R., Lucchini, M., Gallmann, L., Ivanov, I., Kheifets, A. S., Dahlström, J. M., Lindroth, E., Argenti, L., Martín, F. & Keller, U. Angular dependence of photoemission time delay in helium. *Physical Review A* **94**, 1 (2016).
19. Johnsson, P, Caillat, J & Dahlstro, J. M. Probing Single-Photon Ionization on the Attosecond Time Scale. **143002**, 1 (2011).
20. Cirelli, C., Marante, C., Heuser, S., Petersson, C. L., Galán, Á. J., Argenti, L., Zhong, S., Busto, D., Isinger, M., Nandi, S., MacLot, S., Rading, L., Johnsson, P, Gisselbrecht, M., Lucchini, M., Gallmann, L., Dahlström, J. M., Lindroth, E., L'Huillier, A., Martín, F. & Keller, U. Anisotropic photoemission time delays close to a Fano resonance. *Nature Communications* **9** (2018).
21. Krüger, C., Fuchs, J., Cattaneo, L. & Keller, U. Attosecond resolution from free running interferometric measurements. *Optics Express* **28**, 12862 (2020).
22. Baggash, M. & Rottke, H. Phase differences in the photoemission from krypton in the fine-structure-split ionization channels  $^2P_{3/2}$  and  $^2P_{1/2}$ . *Phys. Rev. A* **92**, 013424 (1 2015).
23. Guénot, D., Kroon, D., Balogh, E., Larsen, E. W., Kotur, M., Miranda, M., Fordell, T., Johnsson, P, Mauritsson, J., Gisselbrecht, M., Varjú, K., Arnold, C. L., Carette, T., Kheifets, A. S., Lindroth, E., Lhuillier, A. & Dahlström, J. M. Measurements of relative photoemission time delays in noble gas atoms. *Journal of Physics B: Atomic, Molecular and Optical Physics* **47** (2014).



24. Palatchi, C., Dahlström, J. M., Kheifets, A. S., Ivanov, I. A., Canaday, D. M., Agostini, P. & DiMauro, L. F. Atomic delay in helium, neon, argon and krypton. *Journal of Physics B: Atomic, Molecular and Optical Physics* **47**, 245003 (2014).
25. Jain, A., Gaumnitz, T., Kheifets, A. & Wörner, H. J. Using a passively stable attosecond beamline for relative photoemission time delays at high XUV photon energies. *Optics Express* **26**, 28604 (2018).
26. Jain, A., Gaumnitz, T., Bray, A., Kheifets, A. & Wörner, H. J. Photoionization delays in xenon using single-shot referencing in the collinear back-focusing geometry. *Optics Letters* **43**, 4510 (2018).
27. Vos, J., Cattaneo, L., Patchkovskii, S., Zimmermann, T., Cirelli, C., Lucchini, M., Kheifets, A., Landsman, A. S. & Keller, U. Orientation-dependent stereo Wigner time delay and electron localization in a small molecule. *Science* **360**, 1326 (2018).
28. Cattaneo, L., Vos, J., Bello, R. Y., Palacios, A., Heuser, S., Pedrelli, L., Lucchini, M., Cirelli, C., Martín, F & Keller, U. Attosecond coupled electron and nuclear dynamics in dissociative ionization of H<sub>2</sub>. *Nature Physics* **14**, 733 (2018).
29. Huppert, M., Jordan, I., Baykusheva, D., Von Conta, A. & Wörner, H. J. Attosecond Delays in Molecular Photoionization. *Physical Review Letters* **117**, 1 (2016).
30. Schultze, M., Bothschafter, E. M., Sommer, A., Holzner, S., Schweinberger, W., Fiess, M., Hofstetter, M., Kienberger, R., Apalkov, V., Yakovlev, V. S., Stockman, M. I. & Krausz, F. Controlling dielectrics with the electric field of light. *Nature* **493**, 75 (2013).
31. Schultze, M., Ramasesha, K., Pemmaraju, C., Sato, S., Whitmore, D., Gandman, A., Prell, J. S., Borja, L. J., Prendergast, D., Yabana, K., Neumark, D. M. & Leone, S. R. Attosecond band-gap dynamics in silicon. *Science* **346**, 1348 (2014).
32. Jordan, I., Huppert, M., Rattenbacher, D., Peper, M., Jelovina, D., Perry, C., Conta, A. V., Schild, A., Wörner, H. J. & Carlo, M. Attosecond spectroscopy of liquid water. *Science* **369**, 974 (2020).
33. Jordan, I. & Wörner, H. J. Extracting attosecond delays from spectrally overlapping interferograms. *Journal of Optics* **20**, 024013 (2018).
34. Hertel, I. & Schulz, C. *Atome, Moleküle und Optische Physik 1* (Springer, 2008).
35. Atkins, P., Atkins, P., Friedman, R. & Atkins, U. *Molecular Quantum Mechanics Molecular Quantum Mechanics v. 4* (Oxford University Press, 2005).
36. Sakurai, J. & Napolitano, J. *Modern Quantum Mechanics* (Cambridge University Press, 2017).
37. Hertel, I. & Schulz, C. *Atome, Moleküle und optische Physik 2: Moleküle und Photonen - Spektroskopie und Streuphysik* (Springer Berlin Heidelberg, 2010).

38. Dehmer, J. L. Shape Resonances in Molecular Fields. *ACS Symp. Ser.; (United States)* **263**, 139 (1984).
39. Wigner, E. P. Lower Limit for the Energy Derivative of the Scattering Phase Shift. *Physical Review* **98**, 145 (1955).
40. Smith, F. T. Lifetime Matrix in Collision Theory. *Physical Review* **118**, 349 (1960).
41. Hockett, P., Frumker, E., Villeneuve, D. M. & Corkum, P. B. Time delay in molecular photoionization. *Journal of Physics B: Atomic, Molecular and Optical Physics* **49** (2016).
42. Gallmann, L., Jordan, I., Wörner, H. J., Castiglioni, L., Hengsberger, M., Osterwalder, J., Arrell, C. A., Chergui, M., Liberatore, E., Rothlisberger, U. & Keller, U. Photoemission and photoionization time delays and rates. *Structural Dynamics* **4** (2017).
43. Baykusheva, D. & Wörner, H. J. Theory of attosecond delays in molecular photoionization. *The Journal of chemical physics* **146**, 124306 (2017).
44. Pazourek, R., Nagele, S. & Burgdörfer, J. Attosecond chronoscopy of photoemission. *Rev. Mod. Phys.* **87**, 765 (3 2015).
45. Gianturco, F. A., Lucchese, R. R. & Sanna, N. Calculation of low-energy elastic cross sections for electron-CF<sub>4</sub> scattering. *J. Chem. Phys.* **100**, 6464 (1994).
46. Natalense, A. P. P. & Lucchese, R. R. Cross section and asymmetry parameter calculation for sulfur 1s photoionization of SF<sub>6</sub>. *J. Chem. Phys.* **111**, 5344 (1999).
47. Klünder, K., Dahlström, J. M., Gisselbrecht, M., Fordell, T., Swoboda, M., Guénot, D., Johnsson, P., Caillat, J., Mauritsson, J., Maquet, A., Taïeb, R. & L'Huillier, A. Probing Single-Photon Ionization on the Attosecond Time Scale. *Phys. Rev. Lett.* **106**, 143002 (14 2011).
48. Itatani, J., Quéré, F., Yudin, G. L., Ivanov, M. Y., Krausz, F. & Corkum, P. B. Attosecond Streak Camera. *Phys. Rev. Lett.* **88**, 173903 (17 2002).
49. Muller, H. Reconstruction of attosecond harmonic beating by interference of two-photon transitions. *Applied Physics B* **74**, s17 (2002).
50. Chang, Z. *Fundamentals of Attosecond Optics* (CRC Press, 2016).
51. McPherson, A., Gibson, G., Jara, H., Johann, U., Luk, T. S., McIntyre, I. A., Boyer, K. & Rhodes, C. K. Studies of multiphoton production of vacuum-ultraviolet radiation in the rare gases. *J. Opt. Soc. Am. B* **4**, 595 (1987).
52. Corkum, P. B. Plasma perspective on strong field multiphoton ionization. *Physical Review Letters* **71**, 1994 (1993).
53. Lewenstein, M., Balcou, P., Ivanov, M. Y., L'Huillier, A. & Corkum, P. B. Theory of high-harmonic generation by low-frequency laser fields. *Phys. Rev. A* **49**, 2117 (3 1994).

54. Maroju, P. K., Grazioli, C., Di Fraia, M., Moioli, M., Ertel, D., Ahmadi, H., Plekan, O., Finetti, P., Allaria, E., Giannessi, L., De Ninno, G., Spezzani, C., Penco, G., Spampinati, S., Demidovich, A., Danailov, M. B., Borghes, R., Kourousias, G., Sanches Dos Reis, C. E., Billé, F., Lutman, A. A., Squibb, R. J., Feifel, R., Carpeggiani, P., Reduzzi, M., Mazza, T., Meyer, M., Bengtsson, S., Ibrakovic, N., Simpson, E. R., Mauritsson, J., Csizmadia, T., Dumergue, M., Kühn, S., Nandiga Gopalakrishna, H., You, D., Ueda, K., Labeye, M., Bækhoj, J. E., Schafer, K. J., Gryzlova, E. V., Grum-Grzhimailo, A. N., Prince, K. C., Callegari, C. & Sansone, G. Attosecond pulse shaping using a seeded free-electron laser. *Nature* **578**, 386 (2020).
55. Jaco, F. *Novel schemes of attosecond interferometry* PhD thesis (2021).
56. Kulander, K. C., Schafer, K. J. & Krause, J. L. in *Super-Intense Laser-Atom Physics* (eds Piraux, B., L’Huillier, A. & Rzażewski, K.) 95 (Springer US, Boston, MA, 1993).
57. Salières, P., Carré, B., Le Déroff, L., Grasbon, F., Paulus, G. G., Walther, H., Kopold, R., Becker, W., Milošević, D. B., Sanpera, A. & Lewenstein, M. Feynman’s Path-Integral Approach for Intense-Laser-Atom Interactions. *Science* **292**, 902 (2001).
58. Pertot, Y., Schmidt, C., Matthews, M., Chauvet, A., Huppert, M., Svoboda, V., Von Conta, A., Tehlar, A., Baykusheva, D., Wolf, J. P. & Wörner, H. J. Time-resolved x-ray absorption spectroscopy with a water window high-harmonic source. *Science* **355**, 264 (2017).
59. Dahlström, J., Guénot, D., Klünder, K., Gisselbrecht, M., Mauritsson, J., L’Huillier, A., Maquet, A. & Taïeb, R. Theory of attosecond delays in laser-assisted photoionization. *Chemical Physics* **414**, 53 (2013).
60. Paul, P. M., Toma, E. S., Breger, P., Mullot, G., Augé, F., Balcou, P., Muller, H. G. & Agostini, P. Observation of a train of attosecond pulses from high harmonic generation. *Science* **292**, 1689 (2001).
61. Sweetser, J. N., Fittinghoff, D. N. & Trebino, R. Transient-grating frequency-resolved optical gating. *Opt. Lett.* **22**, 519 (1997).
62. Zehnder, L. Ein neuer Interferenzrefraktor. *Zeitschrift für Instrumentenkunde* **11**, 275–285 (1891).
63. Mach, L. Über einen Interferenzrefraktor. *Zeitschrift für Instrumentenkunde* **12**, 89–93 (1892).
64. Ullrich, J., Moshhammer, R., Dorn, A., Dürner, R., Schmidt, L. P. H. & Schmidt-Böcking, H. Recoil-ion and electron momentum spectroscopy: reaction-microscopes. *Reports on Progress in Physics* **66**, 1463 (2003).
65. Dörner, R., Mergel, V., Jagutzki, O., Spielberger, L., Ullrich, J., Moshhammer, R. & Schmidt-Böcking, H. Cold Target Recoil Ion Momentum Spectroscopy: A ‘momentum microscope’ to view atomic collision dynamics. *Physics Report* **330**, 95 (2000).

66. Wiley, W. C. & McLaren, I. H. Time-of-Flight Mass Spectrometer with Improved Resolution. *Review of Scientific Instruments* **26**, 1150 (1955).
67. F.R.S., J. L. D. LXIII. On the theory of the magnetic influence on spectra; and on the radiation from moving ions. *The London, Edinburgh, and Dublin Philosophical Magazine and Journal of Science* **44**, 503 (1897).
68. *RoentDek Flyer* <http://www.roentdek.com/info/leaflets/Flyer.pdf>. Accessed: 2021-07-26.
69. Heck, S. *Photoelectrons in Molecular Fields: An Investigation of Shape Resonances and Electron Retroaction using Coincident 3D Momentum Imaging Technique* MA thesis (2017).
70. Havenith, M. *Infrared Spectroscopy of Molecular Clusters: An Introduction to Intermolecular Forces* (Springer Berlin Heidelberg, 2003).
71. Pauly, H. *Atom, Molecule, and Cluster Beams I: Basic Theory, Production and Detection of Thermal Energy Beams* (Springer Berlin Heidelberg, 2012).
72. Jahnke, T. *Interatomic Coulombic Decay – Experimentelle Untersuchung eines neuartigen, interatomaren Abregungsmechanismus* PhD thesis (2005).
73. Kantorovich, L. V. *Functional analysis and applied mathematics* Translated by C. D. Benster, NBS Rep. 1509, ii+202 (U. S. Department of Commerce, National Bureau of Standards, Los Angeles, Calif., 1952).
74. Czasch, A. *Resort64* (2014).
75. Vos, J., Cattaneo, L., Patchkovskii, S., Zimmermann, T., Cirelli, C., Lucchini, M., Kheifets, A., Landsman, A. S. & Keller, U. Orientation-dependent stereo Wigner time delay and electron localization in a small molecule. *Science* **360**, 1326 (2018).
76. Nandi, S., Plésiat, E., Zhong, S., Palacios, A., Busto, D., Isinger, M., Neoričić, L., Arnold, C. L., Squibb, R. J., Feifel, R., Decleva, P., L’Huillier, A., Martín, F. & Gisselbrecht, M. Attosecond timing of electron emission from a molecular shape resonance. *Science Advances* **6**, eaba7762 (2020).
77. Busto, D., Vinbladh, J., Zhong, S., Isinger, M., Nandi, S., Maclot, S., Johnson, P., Gisselbrecht, M., L’Huillier, A., Lindroth, E. & Dahlström, J. M. Fano’s Propensity Rule in Angle-Resolved Attosecond Pump-Probe Photoionization. *Physical Review Letters* **123**, 133201 (2019).
78. Bray, A. W., Naseem, F. & Kheifets, A. S. Simulation of angular-resolved RABBITT measurements in noble-gas atoms. *Physical Review A* **97**, 1 (2018).
79. Ivanov, I. A. & Kheifets, A. S. Angle-dependent time delay in two-color XUV+IR photoemission of He and Ne. *Physical Review A* **96**, 1 (2017).
80. Hockett, P. Angle-resolved RABBITT: Theory and numerics. *Journal of Physics B: Atomic, Molecular and Optical Physics* **50** (2017).
81. Henriksen, N. E. Molecular alignment and orientation in short pulse laser fields. *Chemical Physics Letters* **312**, 196 (1999).

82. Chacon, A., Lein, M. & Ruiz, C. Asymmetry of Wigner's time delay in a small molecule. *Physical Review A* **89**, 053427 (2014).
83. Biswas, S., Förg, B., Ortmann, L., Schötz, J., Schweinberger, W., Zimmermann, T., Pi, L., Baykushева, D., Masood, H. A., Liontos, I., Kamal, A. M., Kling, N. G., Alharbi, A. F., Alharbi, M., Azzeer, A. M., Hartmann, G., Wörner, H. J., Landsman, A. S. & Kling, M. F. Probing molecular environment through photoemission delays. *Nature Physics* **16**, 778 (2020).
84. Larsen, K. A., Trevisan, C. S., Lucchese, R. R., Heck, S., Iskandar, W., Champenois, E., Gatton, A., Moshhammer, R., Strom, R., Severt, T., Jochim, B., Reedy, D., Weller, M., Landers, A. L., Williams, J. B., Ben-Itzhak, I., Dörner, R., Slaughter, D., McCurdy, C. W., Weber, T. & Rescigno, T. N. Resonance signatures in the body-frame valence photoionization of CF 4. *Physical Chemistry Chemical Physics* **20**, 21075 (2018).
85. Scheid, W. *FUNDAMENTALS OF PHYSICS – VOL. III - Nuclear Reactions* (ed Lopez, J. L. M.) (Eolss Publisher Co. Ltd., 2009).
86. Henson, A. B., Gersten, S., Shagam, Y., Narevicius, J. & Narevicius, E. Observation of Resonances in Penning Ionization Reactions at Sub-Kelvin Temperatures in Resonant Beams. *Science* **338**, 234 (2012).
87. Yao, X.-C., Qi, R., Liu, X.-P., Wang, X.-Q., Wang, Y.-X., Wu, Y.-P., Chen, H.-Z., Zhang, P., Zhai, H., Chen, Y.-A. & Pan, J.-W. Degenerate Bose gases near a d-wave shape resonance. *Nature Physics* **15**, 570 (2019).
88. Hamilton, E. L., Greene, C. H. & Sadeghpour, H. R. Shape-resonance-induced long-range molecular Rydberg states. *Journal of Physics B: Atomic, Molecular and Optical Physics* **35**, L199 (2002).
89. Peper, M. & Deiglmayr, J. Heteronuclear Long-Range Rydberg Molecules. *Phys. Rev. Lett.* **126**, 013001 (1 2021).
90. Schulz, G. J. Resonances in Electron Impact on Atoms. *Reviews of Modern Physics* **45**, 378 (1973).
91. Palmer, R. E. & Rous, P. J. Resonances in electron scattering by molecules on surfaces. *Reviews of Modern Physics* **64**, 383 (1992).
92. Boudaïffa, B., Cloutier, P., Hunting, D., Huels, M. A. & Sanche, L. Resonant formation of DNA strand breaks by low-energy (3 to 20 eV) electrons. *Science* **287**, 1658 (2000).
93. Tonzani, S. & Greene, C. H. Low-energy electron scattering from DNA and RNA bases: Shape resonances and radiation damage. *The Journal of Chemical Physics* **124**, 054312 (2006).
94. Martin, F., Burrow, P. D., Cai, Z., Cloutier, P., Hunting, D. & Sanche, L. DNA strand breaks induced by 0-4 eV electrons: The role of shape resonances. *Physical Review Letters* **93**, 6 (2004).
95. Kleinwachter, P. & Rotter, I. On resonance phenomena in nuclear reaction cross sections. *Journal of Physics G: Nuclear Physics* **8**, 955 (1982).

## References

---

96. Braunstein, M. & McKoy, V. Shape resonances in the photoionization of N<sub>2</sub>O. *The Journal of Chemical Physics* **87**, 224 (1987).
97. Piancastelli, M. The neverending story of shape resonances. *Journal of electron spectroscopy and related phenomena* **100**, 167 (1999).
98. Baykusheva, D. & Wörner, H. J. Theory of attosecond delays in molecular photoionization. *The Journal of Chemical Physics* **146**, 124306 (2017).
99. Loriot, V., Marciniak, A., Nandi, S., Karras, G., Hervé, M., Constant, E., Plésiat, E., Palacios, A., Martín, F. & Lépine, F. High harmonic generation-2  $\omega$  attosecond stereo-photoionization interferometry in N<sub>2</sub>. *Journal of Physics: Photonics* **2**, 024003 (2020).
100. Klünder, K., Dahlström, J. M., Gisselbrecht, M., Fordell, T., Swoboda, M., Guénot, D., Johnsson, P., Caillat, J., Mauritsson, J., Maquet, A., Taïeb & L'Huillier, A. Probing Single-Photon Ionization on the Attosecond Time Scale. *Phys. Rev. Lett.* **106**, 143002 (14 2011).
101. Haessler, S., Fabre, B., Higuët, J., Caillat, J., Ruchon, T., Breger, P., Carré, B., Constant, E., Maquet, A., Mével, E., Salières, P., Taïeb, R. & Mairesse, Y. Phase-resolved attosecond near-threshold photoionization of molecular nitrogen. *Phys. Rev. A* **80**, 011404 (1 2009).
102. Heuser, S., Jiménez Galán, A., Cirelli, C., Marante, C., Sabbar, M., Boge, R., Lucchini, M., Gallmann, L., Ivanov, I., Kheifets, A. S., Dahlström, J. M., Lindroth, E., Argenti, L., Martín, F. & Keller, U. Angular dependence of photoemission time delay in helium. *Phys. Rev. A* **94**, 063409 (6 2016).
103. Cattaneo, L., Vos, J., Bello, R. Y., Palacios, A., Heuser, S., Pedrelli, L., Lucchini, M., Cirelli, C., Martín, F. & Keller, U. Attosecond coupled electron and nuclear dynamics in dissociative ionization of H<sub>2</sub>. *Nature Physics* **14**, 733 (2018).
104. Cattaneo, L., Vos, J., Baykusheva, D., Wörner, H. J. & Keller, U. *Unfolding the Physics of Shape Resonances in the Photoionization of N<sub>2</sub>O in Proceedings of ATTO2019* (2019).
105. Joseph, J., Holzmeier, F., Bresteau, D., Spezzani, C., Ruchon, T., Hergott, J., Tcherbakoff, O., D'Oliveira, P., Houver, J. & Dowek, D. Angle-resolved studies of XUV-IR two-photon ionization in the RABBITT scheme. *Journal of Physics B: Atomic, Molecular and Optical Physics* **53**, 184007 (2020).
106. Hockett, P., Frumker, E., Villeneuve, D. M. & Corkum, P. B. Time delay in molecular photoionization. *Journal of Physics B: Atomic, Molecular and Optical Physics* **49**, 095602 (2016).
107. Hikosaka, Y. & Shigemasa, E. Anisotropic fragment emission on valence photoionization of CF<sub>4</sub>. *Journal of Electron Spectroscopy and Related Phenomena* **152**, 29 (2006).

108. Larsen, K. A., Trevisan, C. S., Lucchese, R. R., Heck, S., Iskandar, W., Champenois, E., Gatton, A., Moshhammer, R., Strom, R., Severt, T., Jochim, B., Reedy, D., Weller, M., Landers, A. L., Williams, J. B., Ben-Itzhak, I., Dörner, R., Slaughter, D., McCurdy, C. W., Weber, T. & Rescigno, T. N. Resonance signatures in the body-frame valence photoionization of CF<sub>4</sub>. *Physical Chemistry Chemical Physics* **20**, 21075 (2018).
109. Yencha, A. J., Hopkirk, A., Hiraya, A., Dujardin, G., Kvaran, A., Hellner, L., Besnard-Ramage, M. J., Donovan, R. J., Goode, J. G., Maier, R. R. J., King, G. C. & Spyrou, S. Threshold photoelectron spectroscopy of CF<sub>4</sub> up to 60.5 eV. *Journal of Electron Spectroscopy and Related Phenomena* **70**, 29 (1994).
110. Tachikawa, H. Ionization Dynamics of the Small-Sized Water Clusters: A Direct Ab Initio Trajectory Study. *The Journal of Physical Chemistry A* **108**, 7853 (2004).
111. Creasey, J., Jones, H., Smith, D., Tuckett, R., Hatherly, P., Codling, K. & Powis, I. Fragmentation of valence electronic states of CF<sub>4</sub><sup>+</sup> and SF<sub>6</sub><sup>+</sup> studied by threshold photoelectron-photoion coincidence spectroscopy. *Chemical Physics* **174**, 441 (1993).
112. Brehm, B., Frey, R., Küstler, A. & Eland, J. Kinetic energy release in ion fragmentation: N<sub>2</sub>O<sup>+</sup>, COS<sup>+</sup> and CF<sub>4</sub><sup>+</sup> decays. *International Journal of Mass Spectrometry and Ion Physics* **13**, 251 (1974).
113. Carlson, T. A., Fahlman, A., Agneta Svensson, W., Krause, M. O., Whitley, T. A., Grimm, F. A., Piancastelli, M. N. & Taylor, J. W. Angle-resolved photoelectron cross section of CF<sub>4</sub>. *The Journal of Chemical Physics* **81**, 3828 (1984).
114. Velchev, I., Hogervorst, W. & Ubachs, W. Precision VUV spectroscopy of Ar I at 105 nm. *Journal of Physics B: Atomic, Molecular and Optical Physics* **32**, L511 (1999).
115. Sze, K. H. & Brion, C. E. Inner-shell and valence-shell electronic excitation of SF<sub>6</sub>, SeF<sub>6</sub> and TeF<sub>6</sub> by high energy electron impact: An investigation of potential barrier effects. *Chemical Physics* **140**, 439 (1990).
116. Holzmeier, F., Joseph, J., Houver, J.-C., Lebech, M., Dowek, D. & Lucchese, R. R. *What Causes the Angular Dependence of Photoionization Time Delays in a Shape Resonance?* 2021.
117. McCurdy, C. W., Rescigno, T. N., Trevisan, C. S., Lucchese, R. R., Gaire, B., Menssen, A., Schöffler, M. S., Gatton, A., Neff, J., Stammer, P. M., Rist, J., Eckart, S., Berry, B., Severt, T., Sartor, J., Moradmand, A., Jahnke, T., Landers, A. L., Williams, J. B., Ben-Itzhak, I., Dörner, R., Belkacem, A. & Weber, T. Unambiguous observation of F-atom core-hole localization in CF<sub>4</sub> through body-frame photoelectron angular distributions. *Physical Review A* **95**, 1 (2017).
118. Yin, Y.-Y., Chen, C., Elliott, D. & Smith, A. Asymmetric photoelectron angular distributions from interfering photoionization processes. *Physical review letters* **69**, 2353 (1992).

119. Sabbar, M., Heuser, S., Boge, R., Lucchini, M., Gallmann, L., Cirelli, C. & Keller, U. Combining attosecond XUV pulses with coincidence spectroscopy. *Review of Scientific Instruments* **85** (2014).
120. Jordan, I., Huppert, M., Rattenbacher, D., Peper, M., Jelovina, D., Perry, C., von Conta, A., Schild, A. & Wörner, H. J. Attosecond Spectroscopy of Liquid Water. *Science* **369**, 974 (2020).
121. Dahlström, J. M., L'Huillier, A & Maquet, A. Introduction to attosecond delays in photoionization. *Journal of Physics B: Atomic, Molecular and Optical Physics* **45**, 183001 (2012).
122. Dahlström, J., Guénot, D., Klünder, K., Gisselbrecht, M., Mauritsson, J., L'Huillier, A., Maquet, A. & Taieb, R. Theory of attosecond delays in laser-assisted photoionization. *Chemical Physics* **414**, 53 (2013).
123. Sabbar, M., Heuser, S., Boge, R., Lucchini, M., Gallmann, L., Cirelli, C. & Keller, U. Combining attosecond XUV pulses with coincidence spectroscopy. *Review of Scientific Instruments* **85**, 103113 (2014).
124. Sederberg, S., Zimin, D., Keiber, S., Siegrist, F., Wismer, M. S., Yakovlev, V. S., Floss, I., Lemell, C., Burgdörfer, J., Schultze, M., Krausz, F. & Karpowicz, N. Attosecond optoelectronic field measurement in solids. *Nature Communications* **11**, 1 (2020).
125. Sommer, A., Bothschafter, E. M., Sato, S. A., Jakubeit, C., Latka, T., Razskazovskaya, O., Fattahi, H., Jobst, M., Schweinberger, W., Shirvanyan, V., Yakovlev, V. S., Kienberger, R., Yabana, K., Karpowicz, N., Schultze, M. & Krausz, F. Attosecond nonlinear polarization and light-matter energy transfer in solids. *Nature* **534**, 86 (2016).
126. Cavalieri, A. L., Müller, N., Uphues, T., Yakovlev, V. S., Baltuška, A., Horvath, B., Schmidt, B., Blümel, L., Holzwarth, R., Hendel, S., Drescher, M., Kleineberg, U., Echenique, P. M., Kienberger, R., Krausz, F. & Heinzmann, U. Attosecond spectroscopy in condensed matter. *Nature* **449**, 1029 (2007).
127. Schultze, M., Ramasesha, K., Pemmaraju, C. D., Sato, S. A., Whitmore, D., Gandman, A., Prell, J. S., Borja, L. J., Prendergast, D., Yabana, K., Neumark, D. M. & Leone, S. R. Attosecond band-gap dynamics in silicon. *Science* **346**, 1348 (2014).
128. Rattenbacher, D., Jordan, I., Schild, A. & Wörner, H. J. Nonlocal mechanisms of attosecond interferometry and implications for condensed-phase experiments. *Physical Review A* **97**, 063415 (2018).
129. Sanche, L. Beyond radical thinking. *Nature* **461**, 358 (2009).
130. Boudaiffa, B., Cloutier, P., Hunting, D., Huels, M. A. & Sanche, L. Resonant Formation of DNA Strand Breaks by Low-Energy (3 to 20 eV) Electrons. *Science* **287**, 1658 (2000).



131. Garrett, B. C., Dixon, D. A., Camaioni, D. M., Chipman, D. M., Johnson, M. A., Jonah, C. D., Kimmel, G. A., Miller, J. H., Rescigno, T. N., Rossky, P. J., *et al.* Role of water in electron-initiated processes and radical chemistry: Issues and scientific advances. *Chemical reviews* **105**, 355 (2005).
132. Svoboda, V., Michiels, R., LaForge, A. C., Stienkemeier, F., Slavíček, P. & Wörner, H. J. Real-time observation of water radiolysis and hydrated electron formation induced by extreme-ultraviolet pulses. *Science Advances* **6**, eaaz0385 (2020).
133. Loh, Z.-H., Doumy, G., Arnold, C., Kjellsson, L., Southworth, S., Al Haddad, A., Kumagai, Y., Tu, M.-F., Ho, P., March, A., *et al.* Observation of the fastest chemical processes in the radiolysis of water. *Science* **367**, 179 (2020).
134. Cavalieri, A. L., Muller, N., Uphues, T., Yakovlev, V. S., Baltuska, A., Horvath, B., Schmidt, B., Blumel, L., Holzwarth, R., Hendel, S., Drescher, M., Kleineberg, U., Echenique, P. M., Kienberger, R., Krausz, F. & Heinzmann, U. Attosecond spectroscopy in condensed matter. *Nature* **449**, 1029 (2007).
135. Schultze, M., Fiess, M., Karpowicz, N., Gagnon, J., Korbman, M., Hofstetter, M., Neppl, S., Cavalieri, A. L., Komninos, Y., Mercouris, T., Nicolaidis, C. A., Pazourek, R., Nägele, S., Feist, J., Burgdörfer, J., Azzeer, A. M., Ernstorfer, R., Kienberger, R., Kleineberg, U., Goulielmakis, E., Krausz, F. & Yakovlev, V. S. Delay in Photoemission. *Science* **328**, 1658 (2010).
136. Ossiander, M., Siegrist, F., Shirvanyan, V., Pazourek, R., Sommer, A., Latka, T., Guggenmos, A., Nagele, S., Feist, J., Burgdörfer, J., *et al.* Attosecond correlation dynamics. *Nature Physics* **13**, 280 (2016).
137. Huppert, M., Jordan, I., Baykusheva, D., von Conta, A. & Wörner, H. J. Attosecond delays in molecular photoionization. *Phys. Rev. Lett.* **117** (2016).
138. Alizadeh, E., Orlando, T. M. & Sanche, L. Biomolecular damage induced by ionizing radiation: the direct and indirect effects of low-energy electrons on DNA. *Annual review of physical chemistry* **66**, 379 (2015).
139. Marsalek, O., Elles, C. G., Pieniasek, P. A., Pluhařová, E., VandeVondele, J., Bradforth, S. E. & Jungwirth, P. Chasing charge localization and chemical reactivity following photoionization in liquid water. *The Journal of chemical physics* **135**, 224510 (2011).
140. Nandi, S., Plésiat, E., Zhong, S., Palacios, A., Busto, D., Isinger, M., Neoričić, L., Arnold, C. L., Squibb, R. J., Feifel, R., Declava, P., L'Huillier, A., Martín, F. & Gisselbrecht, M. Attosecond timing of electron emission from a molecular shape resonance. *Science Advances* **6**, eaba7762 (2020).
141. Anderson, P. W. Absence of diffusion in certain random lattices. *Physical Review* **109**, 1492 (1958).
142. Anderson, P. W. *Basic notions of condensed matter physics* 1 (Westview Press, 1997).

## References

---

143. Prendergast, D., Grossman, J. C. & Galli, G. The electronic structure of liquid water within density-functional theory. *The Journal of chemical physics* **123**, 014501 (2005).
144. Jagutzki, O., Cerezo, A., Czasch, A., Dörner, R., Hattaf, M., Huang, M., Mergel, V., Spillmann, U., Ullmann-Pfleger, K., Weber, T., Schmidt-Böcking, H. & Smith, G. D. Multiple hit readout of a microchannel plate detector with a three-layer delay-line anode. *IEEE Transactions on Nuclear Science* **49 II**, 2477 (2002).
145. Ullrich, J., Moshhammer, R., Dorn, A., Rner, R. D., Schmidt, L. P. H. & Ck-ing, H. S.-B. Recoil-ion and electron momentum spectroscopy: reaction-microscopes. *Reports on Progress in Physics* **66**, 1463 (2003).
146. Dong, F., Heinbuch, S., Rocca, J. J. & Bernstein, E. R. Dynamics and fragmentation of van der Waals clusters: (H<sub>2</sub>O)<sub>n</sub>, (CH<sub>3</sub>OH)<sub>n</sub>, and (NH<sub>3</sub>)<sub>n</sub> upon ionization by a 26.5 eV soft x-ray laser. *Journal of Chemical Physics* **124** (2006).
147. Shiromaru, H., Shinohara, H., Washida, N., Yoo, H.-S. & Kimura, K. Synchrotron radiation measurements of appearance potentials for (H<sub>2</sub>O)<sub>2</sub><sup>+</sup>, (H<sub>2</sub>O)<sub>3</sub><sup>+</sup>, (H<sub>2</sub>O)<sub>2</sub>H<sup>+</sup> and (H<sub>2</sub>O)<sub>3</sub>H<sup>+</sup> in supersonic jets. *Chemical Physics Letters* **141**, 7 (1987).
148. Shi, Z., Ford, J. V., Wei, S. & Castleman, A. W. Water clusters: Contributions of binding energy and entropy to stability. *The Journal of Chemical Physics* **99**, 8009 (1993).
149. Wei, S. & Castleman, A. W. Using reflection time-of-flight mass spectrometer techniques to investigate cluster dynamics and bonding. *International Journal of Mass Spectrometry and Ion Processes* **131**, 233 (1994).
150. Bobbert, C., Schütte, S., Steinbach, C. & Buck, U. Fragmentation and reliable size distributions of large ammonia and water clusters. *The European Physical Journal D* **19**, 183 (2002).
151. Tachikawa, H. Ionization Dynamics of the Small-Sized Water Clusters: A Direct Ab Initio Trajectory Study. *The Journal of Physical Chemistry A* **108**, 7853 (2004).
152. Belau, L., Wilson, K. R., Leone, S. R. & Ahmed, M. Vacuum ultraviolet (VUV) photoionization of small water clusters. *Journal of Physical Chemistry A* **111**, 10075 (2007).
153. Liu, X., Lu, W. C., Wang, C. Z. & Ho, K. M. Energetic and fragmentation stability of water clusters (H<sub>2</sub>O)<sub>n</sub>, n = 2-30. *Chemical Physics Letters* **508**, 270 (2011).
154. Zamith, S., Labastie, P. & Lhermite, J. M. Fragmentation cross sections of protonated water clusters. *Journal of Chemical Physics* **136** (2012).

155. Jordan, I., Jain, A., Gaumnitz, T., Ma, J. & Wörner, H. J. Photoelectron spectrometer for liquid and gas-phase attosecond spectroscopy with field-free and magnetic bottle operation modes. *Review of Scientific Instruments* **89**, 053103 (2018).
156. Shi, Z., Ford, J. V., Wei, S. & Castleman, A. W. Water clusters: Contributions of binding energy and entropy to stability. *The Journal of Chemical Physics* **99**, 8009 (1993).
157. Temelso, B., Archer, K. A. & Shields, G. C. Benchmark structures and binding energies of small water clusters with anharmonicity corrections. *Journal of Physical Chemistry A* **115**, 12034 (2011).
158. Malloum, A., Fifen, J. J., Dhaouadi, Z., Nana Engo, S. G. & Conradie, J. Structures, relative stability and binding energies of neutral water clusters, (H<sub>2</sub>O)<sub>2-30</sub>. *New Journal of Chemistry* **43**, 13020 (2019).
159. Liu, K., Brown, M. G., Carter, C., Saykally, R. J., Gregory, J. K. & Clary, D. C. Characterization of a cage form of the water hexamer. *Nature* **381**, 501 (1996).
160. Liu, A. K., Cruzan, J. D. & Saykally, R. J. Published by : American Association for the Advancement of Science. *Science* **271**, 929 (1996).
161. Xantheas, S. S. Cooperativity and hydrogen bonding network in water clusters. *Chemical Physics* **258**, 225 (2000).
162. Richardson, J. O., Perez, C., Lobsiger, S., Reid, A. A., Temelso, B., Shields, G. C., Kisiel, Z., Wales, D. J., Pate, B. H. & Althorpe, S. C. Concerted hydrogen-bond breaking by quantum tunneling in the water hexamer prism. *Science* **351**, 1310 (2016).
163. Cvitaš, M. T. & Richardson, J. O. Quantum tunnelling pathways of the water pentamer. *Physical Chemistry Chemical Physics* **22**, 1035 (2020).
164. Jahnke, T., Sann, H., Havermeier, T., Kreidi, K., Stuck, C., Meckel, M., Schöffler, M., Neumann, N., Wallauer, R., Voss, S., Czasch, A., Jagutzki, O., Malakzadeh, A., Afaneh, F., Weber, T., Schmidt-Bocking, H. & Dorner, R. Ultrafast energy transfer between water molecules. *Nature Physics* **6**, 139 (2010).
165. Mucke, M., Braune, M., Barth, S., Forstel, M., Lischke, T., Ulrich, V., Arion, T., Becker, U., Bradshaw, A. & Hergenhahn, U. A hitherto unrecognized source of low-energy electrons in water. *Nature Physics* **6**, 143 (2010).
166. Unger, I., Seidel, R., Thürmer, S., Pohl, M. N., Aziz, E. F., Cederbaum, L. S., Muchová, E., Slaviček, P., Winter, B. & Kryzhevoi, N. V. Observation of electron-transfer-mediated decay in aqueous solution. *Nature Chemistry* **9**, 708 (2017).
167. Hagena, O. F. & Obert, W. Cluster formation in expanding supersonic jets: effect of pressure, temperature, nozzle size, and test gas. *The Journal of Chemical Physics* **56**, 1793 (1972).

168. Pradzynski, C. C., Forck, R. M., Zeuch, T., Slavíček, P. & Buck, U. A fully size-resolved perspective on the crystallization of water clusters. *Science* **337**, 1529 (2012).
169. Hermann, G., Pohl, V., Tremblay, J. C., Paulus, B., Hege, H.-C. & Schild, A. ORBKIT: A modular python toolbox for cross-platform postprocessing of quantum chemical wavefunction data. *Journal of Computational Chemistry* **37**, 1511 (2016).
170. Böhmer, H. U. & Peyerimhoff, S. D. Stability and structure of singly-charged argon clusters  $\text{Ar}_n^+$ ,  $n=3-27$ . A Monte-Carlo simulation. *Zeitschrift für Physik D Atoms, Molecules and Clusters* **11**, 239 (1989).
171. Bonhommeau, D., Halberstadt, N. & Viel, A. Fragmentation dynamics of argon clusters ( $\text{Ar}_n$ ,  $n=2$  to 11) following electron-impact ionization: Modeling and comparison with experiment. *Journal of Chemical Physics* **124** (2006).
172. M. Cardona, L. L. *Photoemission in Solids I* (Springer-Verlag Berlin Heidelberg, 1978).
173. Hoare, M. & Pal, P. Physical cluster mechanics: Statics and energy surfaces for monatomic systems. *Advances in Physics* **20**, 161 (1971).
174. Young, T. The Bakerian Lecture. Experiments and Calculations relative to physical Optics. *PHILOSOPHICAL TRANSACTIONS* (1803).
175. Jönsson, C. Elektroneninterferenzen an mehreren künstlich hergestellten Feinspalten. *Zeitschrift für Physik* **161**, 454 (1961).
176. Cohen, H. D. & Fano, U. Interference in the photo-ionization of molecules. *Physical Review* **150**, 30 (1966).
177. Liu, X.-J., Cherepkov, N. A., Semenov, S. K., Kimberg, V., Gel'mukhanov, F., Prümper, G., Lischke, T., Tanaka, T., Hoshino, M., Tanaka, H. & Ueda, K. Young's double-slit experiment using core-level photoemission from  $\text{N}_2$ : revisiting Cohen–Fano's two-centre interference phenomenon. *Journal of Physics B: Atomic, Molecular and Optical Physics* **39**, 4801 (2006).
178. Le, A. T., Tong, X. M. & Lin, C. D. Evidence of two-center interference in high-order harmonic generation from  $\text{CO}_2$ . *Physical Review A - Atomic, Molecular, and Optical Physics* **73**, 2 (2006).
179. Akoury, D., Kreidi, K., Jahnke, T., Weber, T., Staudte, A., Schöffler, M., Neumann, N., Titze, J., Schmidt, L. P. H., Czasch, A., Jagutzki, O., Fraga, R. A. C., Grisenti, R. E., Muiño, R. D., Cherepkov, N. A., Semenov, S. K. & Ranitovic, P. The Simplest Double Slit : *Science* **318**, 949 (2007).

180. Schöffler, M. S., Kreidi, K., Akoury, D., Jahnke, T., Staudte, A., Neumann, N., Titze, J., Schmidt, L. P. H., Czasch, A., Jagutzki, O., Costa Fraga, R. A., Grisenti, R. E., Smolarski, M., Ranitovic, P., Cocke, C. L., Osipov, T., Adaniya, H., Lee, S., Thompson, J. C., Prior, M. H., Belkacem, A., Weber, T., Landers, A., Schmidt-Böcking, H. & Dörner, R. Photo-double-ionization of H<sub>2</sub>: Two-center interference and its dependence on the internuclear distance. *Physical Review A* **78**, 013414 (2008).
181. Baker, S., Robinson, J. S., Lein, M., Chirilă, C. C., Torres, R., Bandulet, H. C., Comtois, D., Kieffer, J. C., Villeneuve, D. M., Tisch, J. W. G. & Marangos, J. P. Dynamic Two-Center Interference in High-Order Harmonic Generation from Molecules with Attosecond Nuclear Motion. *Physical Review Letters* **101**, 053901 (2008).
182. Kreidi, K., Akoury, D., Jahnke, T., Weber, T., Staudte, A., Schöffler, M., Neumann, N., Titze, J., Schmidt, L. P. H., Czasch, A., Jagutzki, O., Costa Fraga, R. A., Grisenti, R. E., Smolarski, M., Ranitovic, P., Cocke, C. L., Osipov, T., Adaniya, H., Thompson, J. C., Prior, M. H., Belkacem, A., Landers, A. L., Schmidt-Böcking, H. & Dörner, R. Interference in the Collective Electron Momentum in Double Photoionization of H<sub>2</sub>. *Physical Review Letters* **100**, 133005 (2008).
183. Chen, Y. J. & Liu, J. High-order harmonic generation from diatomic molecules with large internuclear distance: The effect of two-center interference. *Physical Review A* **77**, 013410 (2008).
184. Hargreaves, L. R., Colyer, C., Stevenson, M. A., Lohmann, B., Al-Hagan, O., Madison, D. H. & Ning, C. G. (2,2e) study of two-center interference effects in the ionization of N<sub>2</sub>. *Physical Review A* **80**, 062704 (2009).
185. Chaluvadi, H., Ozer, Z. N., Dogan, M., Ning, C., Colgan, J. & Madison, D. Observation of two-center interference effects for electron impact ionization of N<sub>2</sub>. *Journal of Physics B: Atomic, Molecular and Optical Physics* **48** (2015).
186. Li, X., Ren, X., Hossen, K., Wang, E., Chen, X. & Dorn, A. Two-center interference in electron-impact ionization of molecular hydrogen. *Physical Review A* **97**, 022706 (2018).
187. Nagy, L., Borbély, S. & Póra, K. Interference effects in the photoionization of molecular hydrogen. *Physics Letters A* **327**, 481 (2004).
188. Kanai, T., Minemoto, S. & Sakai, H. Quantum interference during high-order harmonic generation from aligned molecules. *Nature* **435**, 470 (2005).
189. Vozzi, C., Calegari, F., Benedetti, E., Caumes, J. P., Sansone, G., Stagira, S., Nisoli, M., Torres, R., Heesel, E., Kajumba, N., Marangos, J. P., Altucci, C. & Velotta, R. Controlling two-center interference in molecular high harmonic generation. *Physical Review Letters* **95**, 1 (2005).
190. Rupenyan, A., Kraus, P. M., Schneider, J. & Wörner, H. J. High-harmonic spectroscopy of isoelectronic molecules: Wavelength scaling of electronic structure and multielectron effects. *Phys. Rev. A* **87**, 033409 (3 2013).

191. Rupenyay, A., Kraus, P. M., Schneider, J. & Wörner, H. J. Quantum interference and multielectron effects in high-harmonic spectra of polar molecules. *Phys. Rev. A* **87**, 031401 (3 2013).
192. Van der Zwan, E. V. & Lein, M. Two-center interference and ellipticity in high-order harmonic generation from H<sub>2</sub><sup>+</sup>. *Physical Review A* **82**, 033405 (2010).
193. Serov, V. V., Derbov, V. L. & Sergeeva, T. A. Interpretation of time delay in the ionization of two-center systems. *Physical Review A* **87**, 063414 (2013).
194. Liao, Y., Zhou, Y., Pi, L.-W., Ke, Q., Liang, J., Zhao, Y., Li, M. & Lu, P. Two-center interference and stereo Wigner time delay in photoionization of asymmetric molecules. *Physical Review A* **104**, 013110 (2021).
195. Ning, Q.-C., Peng, L.-Y., Song, S.-N., Jiang, W.-C., Nagele, S., Pazourek, R., Burgdörfer, J. & Gong, Q. Attosecond streaking of Cohen-Fano interferences in the photoionization of H<sub>2</sub><sup>+</sup>. *Physical Review A* **90**, 013423 (2014).
196. Saalman, U. & Rost, J. M. Proper Time Delays Measured by Optical Streaking. *Physical Review Letters* **125**, 113202 (2020).
197. Kunitski, M., Eicke, N., Huber, P., Köhler, J., Zeller, S., Voigtsberger, J., Schlott, N., Henrichs, K., Sann, H., Trinter, F., Schmidt, L. P. H., Kalinin, A., Schöffler, M. S., Jahnke, T., Lein, M. & Dörner, R. Double-slit photoelectron interference in strong-field ionization of the neon dimer. *Nature Communications* **10**, 1 (2019).
198. Neese, F. The ORCA program system. *WIREs Computational Molecular Science* **2**, 73 (2012).
199. Neese, F. Software update: the ORCA program system, version 4.0. *WIREs Computational Molecular Science* **8**, e1327 (2018).
200. Wüest, A. & Merkt, F. Determination of the interaction potential of the ground electronic state of Ne<sub>2</sub> by high-resolution vacuum ultraviolet laser spectroscopy. *The Journal of Chemical Physics* **118**, 8807 (2003).
201. Ulrich, B., Vredenburg, A., Malakzadeh, A., Schmidt, L. P. H., Havermeier, T., Meckel, M., Cole, K., Smolarski, M., Chang, Z., Jahnke, T. & Dörner, R. Imaging of the structure of the argon and neon dimer, trimer, and tetramer. *Journal of Physical Chemistry A* **115**, 6936 (2011).
202. Barker, J. A., Watts, R. O., Lee, J. K., Schafer, T. P. & Lee, Y. T. Interatomic potentials for krypton and xenon. *The Journal of Chemical Physics* **61**, 3081 (1974).
203. Pflüger, T. *Electron Impact Ionization Studies of Small Rare Gas Clusters* PhD thesis (Heidelberg University, 2012).
204. Helm, H., Stephan, K. & Märk, T. D. Electron-impact ionization of Ar<sub>2</sub>, ArKr, Kr<sub>2</sub>, KrXe, and Xe<sub>2</sub>. *Physical Review A* **19**, 2154 (1979).
205. Hatsui, T., Setoyama, H., Kosugi, N., Wassermann, B., Bradeanu, I. L. & Rühl, E. Photoionization of small krypton clusters in the Kr 3d regime: Evidence for site-specific photoemission. *The Journal of Chemical Physics* **123**, 154304 (2005).

206. Gianturco, F. A., Lucchese, R. R. & Sanna, N. Calculation of low-energy elastic cross sections for electron-CF 4 scattering. *The Journal of Chemical Physics* **100**, 6464 (1994).
207. Natalense, A. P. & Lucchese, R. R. Cross section and asymmetry parameter calculation for sulfur 1s photoionization of SF<sub>6</sub>. *The Journal of Chemical Physics* **111**, 5344 (1999).
208. Hall, R. I., Lu, Y., Morioka, Y., Matsui, T., Tanaka, T., Yoshii, H., Hayaishi, T. & Ito, K. High resolution threshold photoelectron spectroscopy of rare gas dimers. *Journal of Physics B: Atomic, Molecular and Optical Physics* **28**, 2435 (1995).
209. Wadt, W. R. The electronic states of Ar<sup>2+</sup>, Kr<sup>2+</sup>, Xe<sup>2+</sup>. I. Potential curves with and without spin-orbit coupling. *The Journal of Chemical Physics* **68**, 402 (1978).
210. Hay, P. J. & Dunning, T. H. Polarization CI wavefunctions: the valence states of the NH radical. *The Journal of Chemical Physics* **64**, 5077 (1976).
211. Sann, H., Schober, C., Mhamdi, A., Trinter, F., Müller, C., Semenov, S. K., Stener, M., Waitz, M., Bauer, T., Wallauer, R., Goihl, C., Titze, J., Afaneh, F., Schmidt, L. P. H., Kunitski, M., Schmidt-Böcking, H., Demekhin, P. V., Cherepov, N. A., Schöffler, M. S., Jahnke, T. & Dörner, R. Delocalization of a Vacancy across Two Neon Atoms Bound by the van der Waals Force. *Physical Review Letters* **117**, 263001 (2016).
212. Sansone, G., Kelkensberg, F., Pérez-Torres, J. F., Morales, F., Kling, M. F., Siu, W., Ghafur, O., Johnsson, P., Swoboda, M., Benedetti, E., Ferrari, F., Lépine, F., Sanz-Vicario, J. L., Zhrebtsov, S., Znakovskaya, I., L'Huillier, A., Ivanov, M. Y., Nisoli, M., Martín, F. & Vrakking, M. J. J. Electron localization following attosecond molecular photoionization. *Nature* **465**, 763 (2010).
213. Kling, M. F., Siedschlag, C., Verhoef, A. J., Khan, J. I., Schultze, M., Uphues, T., Ni, Y., Uiberacker, M., Drescher, M., Krausz, F. & Vrakking, M. J. J. Control of Electron Localization in Molecular Dissociation. *Science* **312**, 246 (2006).
214. Ray, D., He, F., De, S., Cao, W., Mashiko, H., Ranitovic, P., Singh, K. P., Znakovskaya, I., Thumm, U., Paulus, G. G., Kling, M. F., Litvinyuk, I. V. & Cocke, C. L. Ion-Energy Dependence of Asymmetric Dissociation of D<sub>2</sub> by a Two-Color Laser Field. *Phys. Rev. Lett.* **103**, 223201 (22 2009).
215. Wu, J., Magrakvelidze, M., Schmidt, L. P., Kunitski, M., Pfeifer, T., Schöffler, M., Pitzer, M., Richter, M., Voss, S., Sann, H., Kim, H., Lower, J., Jahnke, T., Czasch, A., Thumm, U. & Dörner, R. Understanding the role of phase in chemical bond breaking with coincidence angular streaking. *Nature Communications* **4** (2013).
216. Mi, Y., Camus, N., Fechner, L., Laux, M., Moshhammer, R. & Pfeifer, T. Electron-Nuclear Coupling through Autoionizing States after Strong-Field Excitation of H<sub>2</sub> Molecules. *Physical Review Letters* **118**, 1 (2017).

217. Martin, F., Fernandez, J., Havermeier, T., Foucar, L., Weber, T., Kreidi, K., Schoffler, M., Schmidt, L., Jahnke, T., Jagutzki, O., Czasch, A., Benis, E. P., Osipov, T., Landers, A. L., Belkacem, A., Prior, M. H., Schmidt-Bocking, H., Cocke, C. L. & Dorner, R. Single Photon-Induced Symmetry Breaking of H<sub>2</sub> Dissociation. *Science* **315**, 629 (2007).
218. Lafosse, A., Lebech, M., Brenot, J. C., Guyon, P. M., Spielberger, L., Jagutzki, O., Houver, J. C. & Doweck, D. Molecular frame photoelectron angular distributions in dissociative photoionization of H<sub>2</sub> in the region of the Q 1 and Q 2 doubly excited states. *Journal of Physics B: Atomic, Molecular and Optical Physics* **36**, 4683 (2003).
219. Waitz, M., Aslitürk, D., Wechselberger, N., Gill, H. K., Rist, J., Wiegandt, F., Goihl, C., Kastirke, G., Weller, M., Bauer, T., Metz, D., Sturm, F. P., Voigtsberger, J., Zeller, S., Trinter, F., Schiwietz, G., Weber, T., Williams, J. B., Schöffler, M. S., Schmidt, L. P. H., Jahnke, T & Dörner, R. Electron Localization in Dissociating H<sub>2</sub><sup>+</sup> by Retroaction of a Photoelectron onto Its Source. *Physical Review Letters* **116**, 1 (2016).
220. Heck, S., Gattton, A., Larsen, K. A., Iskandar, W., Champenois, E. G., Strom, R., Landers, A., Reedy, D., Dailey, C., Williams, J. B., Severt, T., Jochim, B., Ben-Itzhak, I., Moshhammer, R., Dörner, R., Slaughter, D. S. & Weber, T. Symmetry breaking in the body-fixed electron emission pattern due to electron-retroaction in the photodissociation of H<sub>2</sub><sup>+</sup> and D<sub>2</sub><sup>+</sup> close to threshold. *Physical Review Research* **1**, 033140 (2019).
221. Zhang, C., Feng, T., Raabe, N. & Rottke, H. Strong-field ionization of xenon dimers: The effect of two-equivalent-center interference and of driving ionic transitions. *Physical Review A* **97**, 023417 (2018).
222. Wadt, W. R. The electronic states of Ne 2 + , Ar 2 + , Kr 2 + , and Xe 2 + . II. Absorption cross sections for the 1(1/2) u → 1(3/2) g , 1(1/2) g , 2(1/2) g transitions. *The Journal of Chemical Physics* **73**, 3915 (1980).
223. Li, M., Liu, H., Wu, C., Deng, Y., Wu, C., Gong, Q. & Liu, Y. Charge oscillation in multiphoton and tunneling ionization of rare-gas dimers. *Physical Review A* **89**, 025402 (2014).
224. Fano, U. Effects of Configuration Interaction on Intensities and Phase Shifts. *Physical Review* **124**, 1866 (1961).
225. Litman, J. H., Yoder, B. L., Schläppi, B. & Signorell, R. Sodium-doping as a reference to study the influence of intracluster chemistry on the fragmentation of weakly-bound clusters upon vacuum ultraviolet photoionization. *Phys. Chem. Chem. Phys.* **15**, 940 (2013).
226. Zhang, C., Andersson, T., Förstel, M., Mucke, M., Arion, T., Tchapyguine, M., Björneholm, O. & Hergenroth, U. The photoelectron angular distribution of water clusters. *J. Chem. Phys.* **138**, 234306 (2013).



- 
227. Hartweg, S., Yoder, B. L., Garcia, G. A., Nahon, L. & Signorell, R. Size-Resolved Photoelectron Anisotropy of Gas Phase Water Clusters and Predictions for Liquid Water. *Physical Review Letters* **118**, 103402 (2017).
228. Chini, M., Mashiko, H., Wang, H., Chen, S., Yun, C., Scott, S., Gilbertson, S. & Chang, Z. Delay control in attosecond pump-probe experiments. *Optics Express* **17**, 21459 (2009).
229. Huppert, M, Jordan, I & Wörner, H. J. Attosecond beamline with actively stabilized and spatially separated beam paths. *Review of Scientific Instruments* **86**, 123106 (2015).
230. Gong, X., Lin, C., He, F., Song, Q., Lin, K., Ji, Q., Zhang, W., Ma, J., Lu, P., Liu, Y., Zeng, H., Yang, W. & Wu, J. Energy-Resolved Ultrashort Delays of Photoelectron Emission Clocked by Orthogonal Two-Color Laser Fields. *Physical Review Letters* **118**, 143203 (2017).
231. Paul, P. M., Toma, E. S., Breger, P., Mullot, G., Augé, F., Balcou, P., Muller, H. G. & Agostini, P. Observation of a train of attosecond pulses from high harmonic generation. *Science* **292**, 1689 (2001).
232. Radi, P. P., Beaud, P., Franzke, D., Frey, H.-M., Gerber, T., Mischler, B. & Tzannis, A.-P. Femtosecond photoionization of (H<sub>2</sub>O)<sub>n</sub> and (D<sub>2</sub>O)<sub>n</sub> clusters. *The Journal of Chemical Physics* **111**, 512 (1999).
233. Huang, C., Kresin, V. V., Pysanenko, A. & Fárniĕk, M. Water cluster fragmentation probed by pickup experiments. *The Journal of Chemical Physics* **145**, 104304 (2016).
234. Smith, M. E., Lucchese, R. R. & McKoy, V. Schwinger variational principle applied to long-range potentials. *Physical Review A* **29**, 1857 (1984).
235. Schoun, S. B., Chirla, R., Wheeler, J., Roedig, C., Agostini, P., Dimauro, L. F., Schafer, K. J. & Gaarde, M. B. Attosecond pulse shaping around a Cooper minimum. *Phys. Rev. Lett.* **112**, 153001 (2014).

---

## List of Publications

1. JB. Ji, **S. Heck**, M. Han and H. J. Wörner. *Attosecond time remapping for free running interferometric measurements*. In preparation.
2. X. Gong, E. Plèsiat, **S. Heck**, A. Palacios, C. Perry, K. Zinchenko, F. Martín and H. J. Wörner. *Attosecond time-resolved symmetry relaxation in polyatomic molecules*. In preparation.
3. X. Gong, D. Jelovina, **S. Heck**, C. Perry, K. Zinchenko, D.R. Baykusheva and H. J. Wörner. *Channel-resolved attosecond photoionization time delays in CH<sub>3</sub>F*. In preparation.
4. **S. Heck**, D. Baykusheva, M. Han, JB. Ji, C. Perry, X. Gong and H. J. Wörner. *Attosecond Interferometry of Shape Resonances in the Molecular Frame*. *Science Advances* (2021), in press.
5. X. Gong\*, **S. Heck**\*, D. Jelovina, C. Perry, K. Zinchenko and H. J. Wörner. *Attosecond Spectroscopy of Size-Resolved Water Clusters*. arXiv:2106.09459 (2021), under review in *Nature*.
6. JB. Ji, **S. Heck**, M. Han and H. J. Wörner. *Quantitative uncertainty determination of phase retrieval in RABBITT*. *Opt. Express* 29, 27732-27749 (2021).
7. K. A. Larsen, T. N. Rescigno, Z. L. Streeter, W. Iskandar, **S. Heck**, A. Gatton, E. G. Champenois, T. Severt, R. Strom, B. Jochim, D. Reedy, D. Call, R. Moshhammer, R. Dörner, A. L. Landers, J. B. Williams, C. W. McCurdy, R. R. Lucchese, I. Ben-Itzhak, D. S. Slaughter, T. Weber. *Mechanisms and dynamics of the NH<sub>2</sub><sup>+</sup> + H<sup>+</sup> and NH<sup>+</sup> + H<sup>+</sup> + H fragmentation channels upon single-photon double ionization of NH<sub>3</sub>*. *J. Phys. B: At. Mol. Opt. Phys.* 53, 244003 (2020)
8. K. A. Larsen, T. N. Rescigno, T. Severt, Z. L. Streeter, W. Iskandar, **S. Heck**, A. Gatton, E. G. Champenois, R. Strom, B. Jochim, D. Reedy, D. Call, R. Moshhammer, R. Dörner, A. L.

- 
- Landers, J. B. Williams, C. W. McCurdy, R. R. Lucchese, I. Ben-Itzhak, D. S. Slaughter, T. Weber. *Photoelectron and fragmentation dynamics of the  $H^+ + H^+$  dissociative channel in  $NH_3$  following direct single-photon double ionization*. Phys. Rev. Research 2, 043056 (2020)
9. **S. Heck**, A. Gatton, K. A. Larsen, W. Iskandar, E. G. Champenois, R. Strom, A. Landers, D. Reedy, C. Dailey, J. B. Williams, T. Severt, B. Jochim, I. Ben-Itzhak, R. Moshhammer, R. Dörner, D. S. Slaughter, and Th. Weber. *Symmetry breaking in the body-fixed electron emission pattern due to electron-retroaction in the photodissociation of  $H_2^+$  and  $D_2^+$  close to threshold*. Phys. Rev. Research 1, 033140 (2019)
10. K. A. Larsen, C. S. Trevisan, R. R. Lucchese, **S. Heck**, W. Iskandar, E. Champenois, A. Gatton, R. Moshhammer, R. Strom, T. Severt, B. Jochim, D. Reedy, M. Weller, A. L. Landers, J. B. Williams, I. Ben-Itzhak, R. Dörner, D. Slaughter, C. W. McCurdy, Th. Weber and T. N. Rescigno. *Resonance signatures in the body-frame valence photoionization of  $CF_4$* . Phys. Chem. Chem. Phys. 20, 21075 (2018)

\* Contributed equally.

---

# Curriculum Vitae

**Name:** Saijoscha Heck  
**Date of Birth:** March 7, 1993  
**Place of Birth:** Schwetzingen, Germany  
**Nationality:** German

## Education

- 2018-2021** Ph.D. student  
ETH Zürich, Zürich, Switzerland  
Laboratory of Physical Chemistry  
Advisor: Prof. Hans Jakob Wörner
- 2015-2017** M.Sc. Physics  
Ruprecht-Karls-Universität, Heidelberg, Germany  
Thesis: *Photoelectrons in Molecular Fields: An Investigation of Shape Resonances and Electron Retroaction using Coincident 3D Momentum Imaging Technique.*  
Advisor: Prof. Robert Moshhammer
- 2012-2015** B.Sc. Physics  
Goethe Universität, Frankfurt am Main, Germany  
Thesis: *Strong-field Ionization in circularly polarized two-color Fields.*  
Advisor: Prof. Reinhard Dörner
- 2003-2012** Allgemeine Deutsche Hochschulreife (Abitur)  
Leibniz Gymnasium, Östringen, Germany

# Acknowledgments

I want to devote these last pages to thank the many people that helped me along this journey.

First of all I thank *Hans Jakob* for giving me the opportunity to start a PhD in his group. As you said, I came at the right time and for the right project. I really enjoyed working in your group and always felt supported while you also gave me all the freedom I could have wished for. You always had an open ear for my questions and took the time to answer them in detail. Thank you!

Second, I want to thank *Gunnar Jeschke* for being the co-examiner for this thesis. I am happy you accepted this task and hope the topics covered in this thesis were interesting for you to read.

Next, I would like to thank all the co-authors of the two manuscripts printed in this thesis. It was a lot of fun to work with all of you and highly motivating to see everyone contributing to get the best out of the results we had. In particular I want to thank *Denitsa* and *Denis* for investing so much of their time into the calculations which were critical in figuring out the interpretation of the experimental results. I feel honored that I got the chance to collaborate with you.

---

One of the most important contributions to this thesis came from *Xiaochun*. You were the reason the COLTRIMS was running after such short time and without you I certainly could not have finished my PhD within the time I did. In the beginning it was challenging to keep up with your pace and work attitude but it was also highly rewarding and I learned a lot during our time together. I remember many late nights in the lab where we not only tightened countless screws of the vacuum chambers but also had many interesting conversations. I wish I could have made it to Shanghai and visited you and your group for a few months as planned (who would have expected a pandemic starting the month my flight was supposed to leave...). I am sure at some point I will come and visit you and I am really looking forward to the Shanghai hot pot you told me so often about.

A big thank you also goes to *Jiabao*. It was a pleasure to supervise you during your Master thesis. At times I felt that I was learning more from you than the other way round. I am happy that you decided to stay for your PhD. You will be a good successor for the COLTRIMS. I also would like to thank *Meng* who takes over the setup together with Jiabao. You are a great colleague and I really appreciated your dinner invitations where the food was always incredibly tasty.

An important part of my PhD life was the whole attogroup. I always enjoyed coming to the lab and the main reason for this are the wonderful fellow PhD students and colleagues I shared my time with. Many of you I now call friends and I want to thank all of you for making my time here such a superb experience.

*Conaill*, I feel lucky that I got to share an office with you. It was always fun to work alongside you and many hours were spent talking science and drinking coffee. I will always remember our trip

---

to Istanbul and I am looking forward to a repetition. *Dan*, I was super happy when you joined the group and learned that you are such a big fan of the outdoors. I really enjoyed our many weekends climbing multi-pitches and I am particularly grateful that you introduced me into the amazing world of mountaineering and took me up my first "4000er". *Danylo*, you were always willing to help with any problem - no matter how busy you were yourself. I also remember many beers together and anytime I think of Adams couch I need to smile :D *Max*, you were always up for discussions on any topic and it was always intellectually stimulating and fun. I am sure you will make a great professor. *Giuseppe*, let's go back to the toro bar at some point! And I strongly hope that you have more luck with your setup in the near future. *Valentina*, you are so full of joy that it is always fun to have you around. I also apologize for the many times I stepped on your toes when you tried to teach me dancing :D *Matteo*, I still wish we will get the chance to go biking together at some point in the future! *Kristina*, I wish we would have started earlier to do stuff together! *Vit*, thank you for explaining to me various quantum-chemistry calculations and teaching me how to use them. *Pengju*, you were always so motivated and coming up with new experimental ideas - it was really infectious and I always enjoyed the many discussions with you - in particular the ones about Chinese politics ;). *Zhong*, thank you for all the career advice and the discussions about science and academia. *Andi*, *Mario* and *Markus*, without your constant help and support, setting up an experiment would have been so much more difficult (or impossible). I hope you realize how valuable your work is for the whole group!

I also had plenty of support coming from friends and family outside ETH. Thank you *Felix*, *Delfi* and *Marian* for always having an open ear when I was frustrated! I am so lucky I can call you my friends. The biggest "thank you" goes to my parents, *Axel* and *Sabine*, which

---

have supported me unconditionally during the last 28 years. You are the reason I always felt capable and encouraged to follow my passions. It is because of you that I ended up where I am now.

**Thank you!**